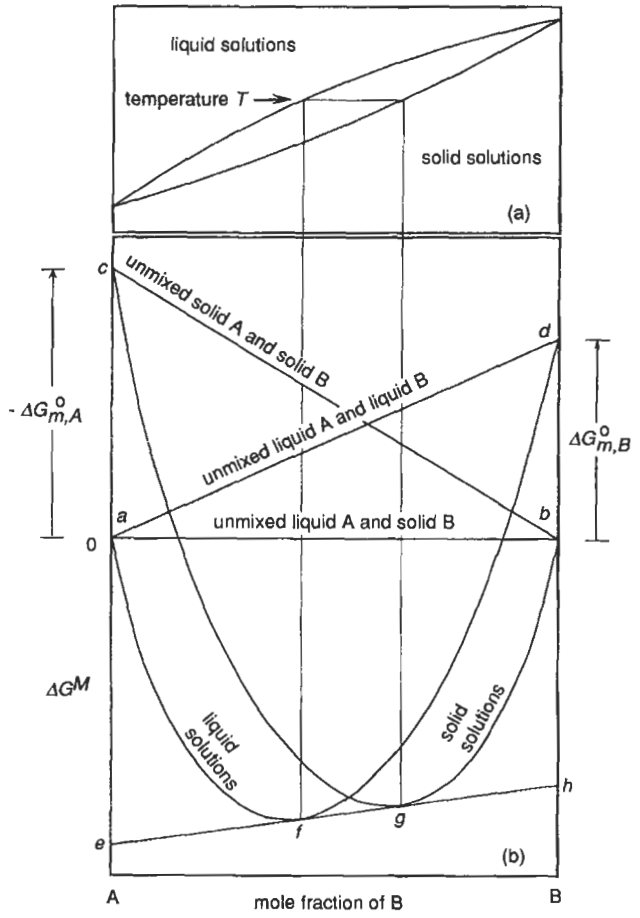

Fig. 10. (a) The phase diagram for the system A–B. (b) The ideal free energy of mixing curves for the system A–B at temperature T.

$$\mathbf{ca} + \mathbf{ae} = \mathbf{ce} \text{ and } \mathbf{db} + \mathbf{bh} = \mathbf{dh}, \tag{54}$$

where: $\mathbf{ce} = \Delta\overline{G}^{M}_{A}$ (relative to solid A as the standard state)
$= RT \ln X_A$ (at the composition **g**),
$\mathbf{ae} = \Delta\overline{G}^{M}_{A}$ (relative to liquid A as the standard state)
$= RT \ln X_A$ (at the composition **f**),
$\mathbf{dh} = \Delta\overline{G}^{M}_{B}$ (relative to liquid B as the standard state)
$= RT \ln X_B$ (at the composition **f**),
and $\mathbf{bh} = \Delta\overline{G}^{M}_{B}$ (relative to solid B as the standard state)
$= RT \ln X_B$ (at the composition **g**).

References: p. 469.

Thus eqs. (54) become:

$$\Delta G^0_{m,A} + RT \ln X_A(\text{liquidus}) = RT \ln X_A(\text{solidus}),$$

and

$$-\Delta G^0_{m,B} + RT \ln X_B(\text{solidus}) = RT \ln X_B(\text{liquidus}).$$

As $X_A(\text{liquidus}) + X_B(\text{liquidus}) = 1$ and $X_A(\text{solidus}) + X_B(\text{solidus}) = 1$, the solidus and liquidus compositions (in a Raoultian system) are thus uniquely determined by the values of $\Delta G^0_{m,A}$ and $\Delta G^0_{m,B}$ as:

$$X_{A(\text{liquidus})} = \frac{1 - \exp\left(-\Delta G^0_{m,B}/RT\right)}{1 - \left[\exp\left(-\Delta G^0_{m,B}/RT\right)\right]\left[\exp\left(\Delta G^0_{m,A}/RT\right)\right]} \tag{55}$$

and

$$X_{A(\text{solidus})} = \frac{\exp\left(\Delta G^0_{m,A}/RT\right)\left[1 - \exp\left(-\Delta G^0_{m,B}/RT\right)\right]}{1 - \left[\exp\left(-\Delta G^0_{m,B}/RT\right)\right]\left[\exp\left(\Delta G^0_{m,A}/RT\right)\right]}. \tag{56}$$

The phase diagram for the system Si–Ge, calculated from eqs. (55) and (56) and the known variations of $\Delta G^0_{m,Si}$ and $\Delta G^0_{m,Ge}$ with temperature, is compared, in fig. 11, with the liquidus and solidus lines determined experimentally by thermal and X-ray analysis. As is seen, the behavior in the system is very close to Raoultian.

Raoultian behavior is very much the exception rather than the rule, and even complete mutual solid solubility between A and B requires that A and B have the same crystal structure, similar atomic sizes, similar electronegativities, and similar valences. The requirement of similar atomic size arises from the introduction of a strain energy into the lattice when the solvent and substitutional solute atoms are of differing size. This strain energy always increases the Gibbs free energy and, hence, can significantly influence the phase relationships in the system. It is found that terminal solid solutions extend only a few atomic percent into a binary system if the atomic diameters differ by more than 14%. Significant differences in electronegativity cause the formation of intermetallic compounds such as Mg_2Si, Mg_2Sn and Mg_2Pb, and differences in valences can cause the formation of electron compounds such as occur in the systems Cu–Zn and Cu–Sn.

Although Cu and Ag are chemically similar, the atomic radius of Ag is 13% larger than that of Cu and hence, as shown in fig. 12a, Cu and Ag form a simple eutectic system. In this system it is presumed that Ag exhibits Raoultian ideal behavior in the Ag-rich α-solid solution and that Cu exhibits Raoultian ideal behavior in the Cu-rich β-solid solution. Consequently Cu in α and Ag in β exhibit Henrian ideal behavior and, at 1000 K, the activities of the components, relative to the pure solids as standard states, are as shown in fig. 12b. At 1000 K, saturation of the α-phase with Cu occurs at $X_{Ag} = 0.9$, and hence, as Ag obeys Raoult's law in the α-phase, $a_{Ag} = 0.9$ at this composition. Phase equilibrium between α saturated with Cu and β saturated with Ag requires that the

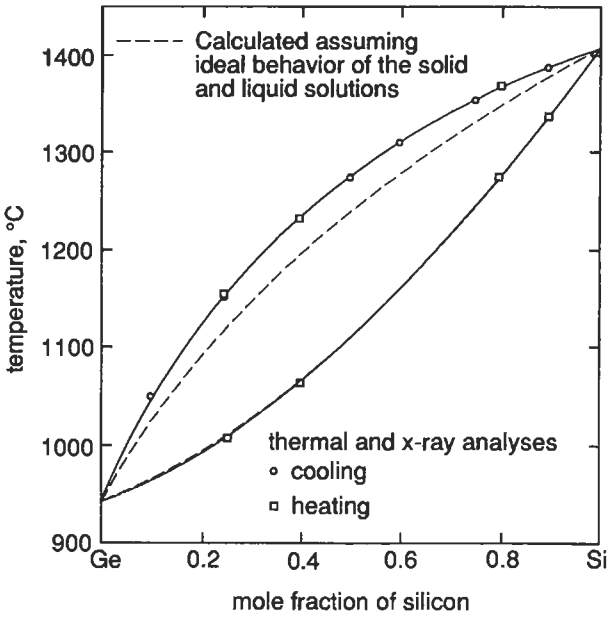

Fig. 11. Comparison of the phase diagram for the system Si–Ge as determined experimentally by X-ray and thermal analysis, with that calculated assuming Raoultian ideal behavior in both the solid and liquid solutions.

activities of both Ag and Cu be the same in both phases, and hence $a_{Ag} = 0.9$ in the Ag-saturated β-phase of composition $X_{Ag} = 0.04$. Similarly, $a_{Cu} = 0.96$ in the Ag-saturated β (at $X_{Cu} = 0.96$) and in the Cu-saturated α (at $X_{Ag} = 0.9$). Thus, in the α-phase, Henrian behavior of Cu is given by:

$$a_{Cu} = 9.6X_{Cu}, \tag{57}$$

and in the β-phase, Henrian behavior of Ag is given by:

$$a_{Ag} = 22.5X_{Ag}.$$

8. *Reaction equilibrium involving solutions and the Gibbs phase rule*

8.1. The dependence of the equilibrium state on activity

In §4 it was shown that, at constant temperature and pressure, equilibrium is established in the reaction

$$aA + bB = cC + dD,$$

when

$$a\overline{G}_A + b\overline{G}_B = c\overline{G}_C + d\overline{G}_D. \tag{58}$$

References: p. 469.

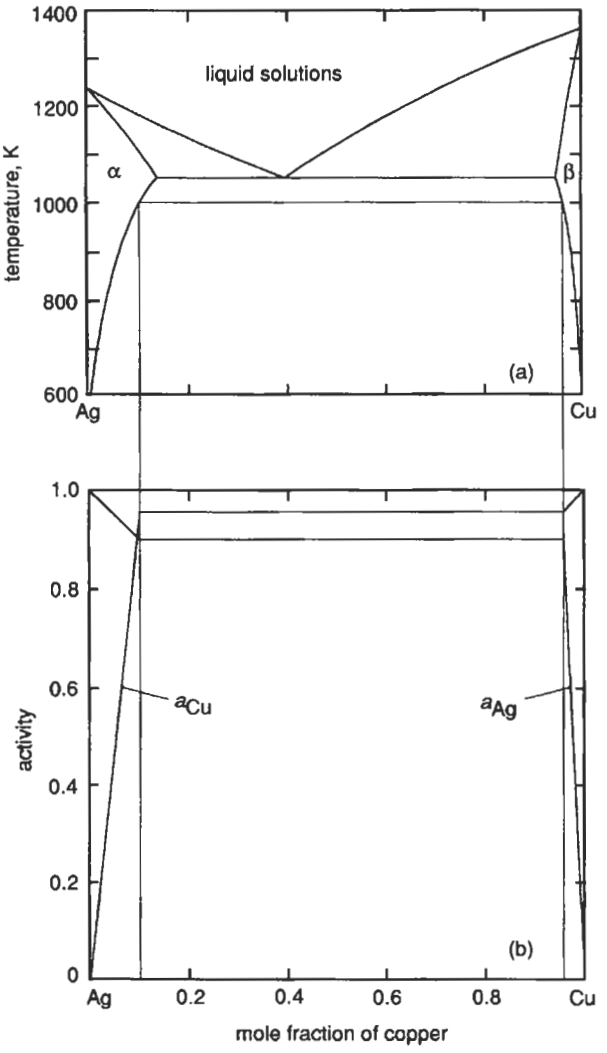

Fig. 12. (a) The phase diagram for the system Ag–Cu. (b) The activities of Ag and Cu in the system Ag–Cu at 1000 K.

As:

$$\overline{G}_i = G_i^0 + RT \ln a_i,$$

eq. (58) can be written as:

$$\Delta G_T^0 = -RT \ln \frac{a_C^c a_D^d}{a_A^a a_B^b},$$

where the quotient in the logarithm term is K_T the equilibrium constant for the reaction.

Consider the oxidation, at 1000 K, of Cu from an Ag–Cu alloy of $X_{Cu} = 0.08$. From eq. (57), the activity of Cu in this alloy, relative to pure solid Cu as the standard state, is

$$a_{Cu} = 9.6X_{Cu} = 9.6 \times 0.08 = 0.768.$$

For the reaction:

$$4Cu_{(s)} + O_{2(g)} = 2Cu_2O_{(s)}$$

$$\Delta G_T^0 = -336810 + 142.5T \text{ J}.$$

Thus, $\Delta G_{1000}^0 = -194300 \text{ J} = -8.3144 \times 1000 \ln K_{1000}$ and so:

$$K_{1000} = 1.41 \times 10^{10} = \frac{a_{Cu_2O}^2}{a_{Cu}^4 p_{O_2}}. \tag{59}$$

Oxidation of the Cu occurs when the oxygen pressure in the system has been increased to the level at which $a_{Cu_2O} = 1$. From eq. (59) this oxygen pressure is:

$$p_{O_2} = \frac{1}{(0.768)^4 \times 1.41 \times 10^{10}} = 2.04 \times 10^{-10} \text{atm}.$$

From eq. (16), ΔG_{1000}^0 for the reaction

$$2Ag_{(s)} + \tfrac{1}{2} O_{2(g)} = Ag_2O_{(s)}$$

has the value 31 062 J. Thus:

$$K_{1000} = \frac{a_{Ag_2O}}{a_{Ag}^2 p_{O_2}^{1/2}} = 0.024.$$

Thus, with $a_{Ag} = 0.92$ (Raoultian behavior in the α-solid solution) and $p_{O_2} = 2.04 \times 10^{-10}$ atm:

$$a_{Ag_2O} = 2.9 \times 10^{-7},$$

which shows that the equilibrium oxide is virtually pure Cu_2O. As the oxygen pressure in the system is further increased, the Cu content in the alloy decreases in accordance with eq. (59). Thus the alloy in equilibrium with virtually pure Cu_2O and air (oxygen fraction 0.21) at 1000 K is that in which

$$a_{Cu} = \left[\frac{1}{1.41 \times 10^{10} \times 0.21}\right]^{1/4} = 0.0043,$$

or $X_{Cu} = a_{Cu}/9.6 = 4.5 \times 10^{-4}$.

At this oxygen pressure the activity of Ag_2O in the equilibrium oxide phase, with $a_{Ag} \approx 1$, is:

References: p. 469.

$$a_{Ag_2O} = 0.024 \times 1 \times 0.21^{1/2} = 0.011,$$

and so the equilibrium oxide phase is still essentially pure Cu_2O.

8.2. The Gibbs phase rule

The complete description of a thermodynamic system containing C components existing in P phases requires specification of the temperatures, pressures and compositions of each of the P phases. As the composition of each phase is defined when the concentrations of $C-1$ of its components are known, the total number of variables in the description is P pressures + P temperatures + $P(C-1)$ concentrations $= P(C+1)$. For thermodynamic equilibrium in the system, each of the P phases must be at the same temperature and same pressure and the activity (or partial molar free energy) of each of the individual components must be the same in each of the P phases. Thus, for equilibrium, there are $(P-1)$ equalities of temperature, $(P-1)$ equalities of pressure and $(P-1)C$ equalities of activity, and hence the total number of equilibrium conditions, given as the number of equations among the variables of the system, is $(P-1)(C+2)$. The number of *degrees of freedom*, F, which the equilibrium system may have, is defined as the maximum number of variables which may be independently altered in value without disturbing the equilibrium in the system. This number is obtained as the difference between the total number of variables available to the system and the minimum number of equations among these variables that is required for maintenance of the equilibrium, i.e.:

$$\begin{aligned} F &= P(C+1) - (P-1)(C+2) \\ &= C + 2 - P. \end{aligned} \tag{60}$$

Equation (60) is the *Gibbs phase rule* and is a powerful tool in the determination of possible equilibria which may occur in multicomponent, multiphase systems.

In the simplest of applications, i.e., in a one-component system, $F = 3 - P$. Thus, with reference to the phase diagram for H_2O, shown in fig. 3, for the existence of a single phase $F = 2$ and so the pressure and temperature can be varied independently without disturbing the equilibrium, i.e., with $F = 2$ the state of the system can be moved about within the area of stability of the single phase in the pressure–temperature diagram. However, for a two-phase equilibrium the state of the system must lie on one of the lines in fig. 3 and thus only the pressure or the temperature can be varied independently. From the phase rule, $F = 1$ and hence the two-phase equilibrium is univariant. The triple point, where the three phases are in equilibrium, occurs at fixed values of temperature and pressure, in accordance with $F = 0$ from the phase rule. The three-phase equilibrium is thus invariant and three is the maximum number of phases which can be in equilibrium with one another in a one-component system.

In a binary system, the inclusion of a second component adds an extra degree of freedom to each equilibrium and hence the maximum number of phases which can be in equilibrium with one another in a two-component system is four. However, phase diagrams for binary systems of metallurgical interest are normally presented for a

pressure of 1 atm, i.e., they are the 1 atm isobaric sections of the phase equilibria occurring in pressure–temperature–composition space, and hence one of the degrees of freedom is used in specifying the pressure. Thus, at an arbitrarily selected pressure such as 1 atm, the maximum number of phases which can exist in equilibrium with one another in a binary system is three (unless, by chance, the arbitrarily selected pressure happens to be that at which an invariant four-phase equilibrium occurs). In the binary system A–B, considered at constant pressure, the available variables are T, a_A and a_B. For the existence of a single phase, such as α, β or liquid in fig. 12a, the phase rule gives $F=2$, and hence any two of T, a_A and a_B may be varied independently. For any two-phase equilibrium, $F=1$ and hence the specification of any one of the three variables fixes the state of the system. For example, specification of the temperature at which the two-phase equilibrium exists fixes the compositions of the equilibrated phases on the appropriate liquidus, solidus or solvus lines; and specification of the composition of one of the equilibrated phases fixes the temperature at which the chosen composition lies on the appropriate liquidus, solidus or solves line and fixes the composition of the second phase at the other end of the tie-line between the two equilibrated phases. The three-phase equilibrium with $F=0$ is invariant, and, in fig. 12a, the eutectic equilibrium occurs at a fixed temperature at which the compositions of the α, β and liquid phases are also fixed.

If some, or all, of the components of a system can react chemically with one another to produce new chemical species, a distinction must be drawn between the terms component and species. For example the *components* silver and oxygen in the binary system Ag–O are capable of reacting to form the new *species* Ag_2O, and hence an equilibrium among the three species Ag, Ag_2O and O_2 can occur in the two-component system. The equilibrium among Ag, Ag_2O and O_2 is called an *independent reaction equilibrium*. In a system containing N species and existing in P phases among which there are R independent reaction equilibria, the number of variables is $P(N+1)$, i.e., P pressures + P temperatures + $P(N-1)$ concentrations. However, if the species i and j react to form the species k, reaction equilibrium requires that

$$\overline{G}_i + \overline{G}_j = \overline{G}_k,$$

and this is an additional equation required among the variables. Thus, if R independent reaction equilibria occur, the number of equations among the $P(N+1)$ variables, required for equilibrium is $(P-1)$ equalities of temperature $+(P-1)$ equalities of pressure $+(P-1)N$ equalities of activity $+R=(P-1)(N+2)+R$, and hence the number of degrees of freedom, F, is

$$\begin{aligned} F &= P(N+1) - (P-1)(N+2) - R \\ &= (N-R) + 2 - P. \end{aligned}$$

Comparison with eq. (60) indicates that

$$C = N - R, \tag{61}$$

References: p. 469.

i.e., the number of components in a system equals the number of species present minus the number of reaction equilibria. Equation (61) is normally used to calculate the number of independent reaction equilibria from knowledge of the number of components and the number of species. For example, in the two-component system Ag–O, the independent reaction equilibrium among the three species is

$$2Ag + \tfrac{1}{2}O_2 = Ag_2O.$$

For equilibrium among the phases metal, metal oxide and oxygen gas in the two-component system, $F=1$ and thus only T or p_{O_2} can be selected as the single degree of freedom. Selection of T fixes ΔG_T^0 and hence, via eq. (34), fixes p_{O_2}, and vice versa.

Consider the various equilibria which can occur in the ternary system Si–C–O, for which a stability diagram is shown in fig. 7. It can be considered that this system contains the six species Si, SiO_2, SiC, C, CO and CO_2, and hence $R=6-3$, i.e., there are three independent reaction equilibria. These are derived as follows. The chemical reaction for formation of each compound from its elements is written:

$$Si + O_2 = SiO_2,$$
$$Si + C = SiC,$$
$$C + O_2 = CO_2,$$
$$C + \tfrac{1}{2}O_2 = CO.$$

These equations are then combined in such a way as to eliminate any elements which are not considered as species in the system, and the minimum number of equations so obtained, is the number of independent reaction equilibria, R. In this case oxygen is not considered as species, and elimination of O_2 gives:

$$C + CO_2 = 2CO, \tag{i}$$

$$Si + C = SiC, \tag{ii}$$

and

$$Si + 2CO_2 = SiO_2 + 2CO \tag{iii}$$

as the independent equilibria. From the phase rule, the maximum number of phases which can coexist in equilibrium is five (the condensed phases Si, SiO_2, SiC, C and the gas phase CO–CO_2). This equilibrium is invariant and occurs at the temperature T_{eq} at which $\Delta G_{(ii)}^0 = 0$ and at the pressure $P = p_{CO} + p_{CO_2}$ at which $K_{(i),T_{eq}} = p_{CO}/p_{CO_2}$ and $K_{(iii),T_{eq}} = (p_{CO}/p_{CO_2})^2$ are simultaneously satisfied. If the temperature is arbitrarily fixed, as is the case in fig. 7, the maximum number of phases which can coexist in equilibrium is four (three condensed phases and a gas phase). One such equilibrium occurs in fig. 7 at point **b**. For the coexistence of two condensed phases and a gas phase at the arbitrarily selected temperature, $F=1$, and such equilibria lie on the univariant lines A, B, C and D in fig. 7, and for equilibrium between a single condensed phase and a gas phase, $F=2$, corresponding to areas of single condensed phase stability in fig. 7.

Occasionally situations are found in which it might appear, at first sight, that the

phase rule is not obeyed, and usually, in such situations a degree of freedom is used by a condition of stoichiometry in the system. For example, in the reduction of ZnO by graphite to produce Zn vapor, CO and CO_2, it might appear that the three-phase equilibrium (ZnO, C and the gas phase) in the three-component system (Zn–O–C) has $F = 5 - 3 = 2$ degrees of freedom, and that, with the five species ZnO, C, $Zn_{(v)}$, CO and CO_2, two independent reaction equilibria occur, which can be selected as

$$ZnO_{(s)} + C_{(gr)} = Zn_{(v)} + CO_{(g)} \tag{iv}$$

and

$$2ZnO_{(s)} + C_{(gr)} = 2Zn_{(v)} + CO_{2(g)}, \tag{v}$$

for which

$$K_{(iv)} = p_{CO} p_{Zn}, \tag{vi}$$

and

$$K_{(v)} = p_{Zn}^2 p_{CO_2}. \tag{vii}$$

However, selecting T, which fixes the values of $K_{(iv)}$ and $K_{(v)}$ and any one of p_{Zn}, p_{CO} or p_{CO_2} as the two apparent degrees of freedom does not fix the state of the system, i.e., does not allow simultaneous solution of eqs. (vi) and (vii). This difficulty arises because the stoichiometry requirement has not been taken into consideration, i.e. that, as all the Zn and O occurring in the gas phase originates from the stoichiometric ZnO, the condition

$$\frac{n_O}{n_{Zn}} = 1 = \frac{n_{CO} + 2n_{CO_2}}{n_{Zn}} = \frac{p_{CO} + 2p_{CO_2}}{p_{Zn}} \tag{viii}$$

must also be satisfied. This stoichiometric requirement decreases F to unity and hence selecting T as the single degree of freedom fixes the partial pressures of Zn, CO and CO_2 as the values required for simultaneous solution of eqs. (vi), (vii) and (viii).

9. *The thermodynamics of surfaces and interfaces*

9.1. The Gibbs adsorption isotherm

In passing from one phase to another in a heterogeneous system, some of the properties undergo significant changes as the boundary between the two phases is traversed. The thin region over which these changes occur is called the *interface*, and a complete thermodynamic analysis of the system requires consideration of the thermodynamic properties of the interface.

Consider fig. 13 which shows the variation of the concentration, c_1, of the component 1 across the interface region in a system comprising equilibrated α and β phases. Calculation of the total number of moles of component 1 in the system as the sum $c_1^\alpha V^\alpha + c_1^\beta V^\beta$, where V^α and V^β are the volumes of the phases, involves the assumption

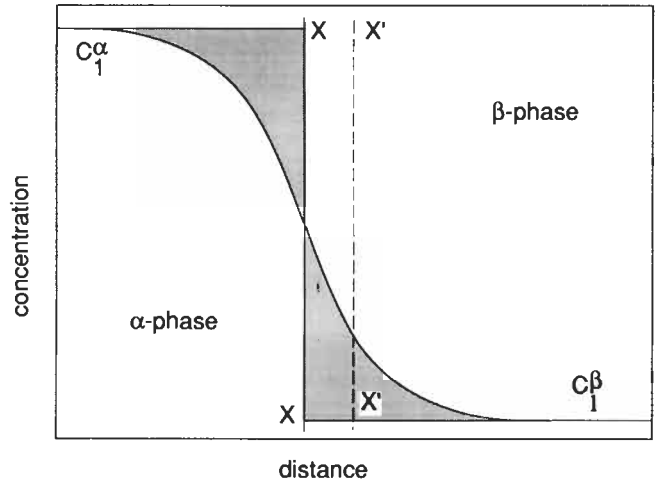

Fig. 13. The variation, with distance, of concentration on passing through the interface between two phases.

that the values c_1^{α} and c_1^{β} occur up to some plane in the interface region, and evaluation of $c_1^{\alpha}V^{\alpha} + c_1^{\beta}V^{\beta}$ requires that a mathematical plane be located somewhere in the interface region. In fig. 13 it is seen that the number of moles of component 1 in the system, calculated as $c_1^{\alpha}V^{\alpha} + c_1^{\beta}V^{\beta}$, is only equal to the actual number of moles of 1 in the system, n_1 when the boundary plane X–X is located such that the shaded areas in fig. 13 are equal. If the boundary plane is located to the right of X–X, say at X′–X′, then:

$$n_1 < c_1^{\alpha}V^{\alpha} + c_1^{\beta}V^{\beta}$$

or, if the boundary plane is located to the left of X–X:

$$n_1 > c_1^{\alpha}V^{\alpha} + c_1^{\beta}V^{\beta}.$$

The difference between n_1 and $c_1^{\alpha}V^{\alpha} + c_1^{\beta}V^{\beta}$ defines the *surface concentration of component 1*, Γ_1, (moles/cm^2), as:

$$\Gamma_1 A_s = n_1 - (c_1^{\alpha}V^{\alpha} + c_1^{\beta}V^{\beta}),$$

where A_s is the area of surface between the two phases. Thus, with the boundary located to the left of X–X, Γ_1 is a positive quantity and with the boundary located to the right of X–X, Γ_1 is a negative quantity. In a single-component system where the boundary is between a condensed phase and a vapor phase, it is logical to locate the boundary at X–X so that the surface concentration is zero. However, with two or more components in the system it is not generally possible to locate the interface at a position at which more than one of the surface concentrations are zero. In such a case X–X is located such that the surface concentration of the solvent, Γ_1, is zero and the surface concentration of the solute, Γ_2, is not zero. This is illustrated in fig. 14.

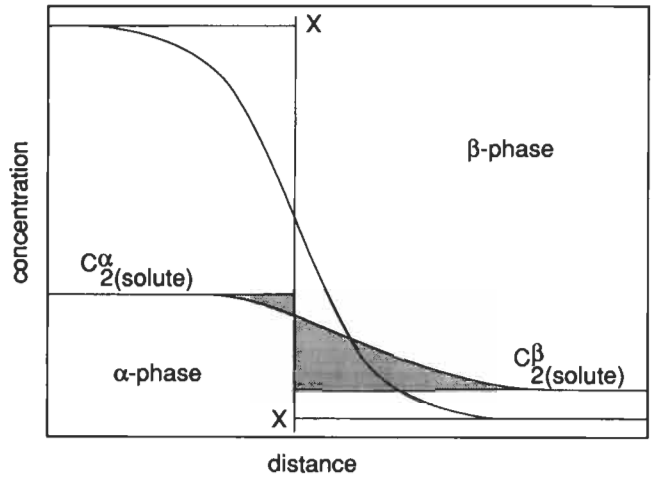

Fig. 14. The variations, with distance, of the concentrations of solvent and solute on passing through an interface, and illustration of the origin of surface concentration of the solute.

The definition of *surface free energy per unit area*, G_s, is analogous to that for the surface concentration, i.e.:

$$G_s A_s = G' - \sum \overline{G}_i^{\alpha} n_i^{\alpha} - \sum \overline{G}_i^{\beta} n_i^{\beta}, \tag{62}$$

where G' is the total free energy of the system.

The *surface tension*, σ, is defined as:

$$\sigma = \left(\frac{\partial G'}{\partial A_s} \right)_{T,P,n_i},$$

and hence, when surfaces are included in the discussion, eq. (13) is written as:

$$dG' = -S'dT + V'dP + \sigma dA_s + \sum \overline{G}_i dn_i \tag{63}$$

If the surface area is increased by dA_s at constant T, P, and n_i, combination of eqs. (62) and (63) gives:

$$G_s dA_s = \sigma dA_s + \left(\sum \overline{G}_i^{\alpha} n_i^{\alpha} + \sum \overline{G}_i^{\beta} n_i^{\beta} \right). \tag{64}$$

As phase equilibrium is maintained, $\overline{G}_i^{\alpha} = \overline{G}_i^{\beta}$; mass balance requires that:

$$dn_i^{\alpha} + dn_i^{\beta} = -\Gamma_i dA_s,$$

in which case eq. (64) can be written as:

$$G_s dA_s = \sigma dA_s + \sum \overline{G}_i \Gamma_i dA_s$$

or:

$$G_s = \sigma + \sum \overline{G}_i \Gamma_i, \tag{65}$$

i.e., the surface free energy is the surface tension plus the free energy due to the surface concentrations of the components.

Complete differentiation of eq. (65) gives:

$$dG_s = d\sigma + \sum \overline{G}_i d\Gamma_i + \sum \Gamma_i d\overline{G}_i, \tag{66}$$

and the differential of G_s for conditions of fixed surface area and fixed P gives:

$$dG_s = -S_s dT + \sum \overline{G}_i d\Gamma_i. \tag{67}$$

Combination of eqs. (66) and (67) gives:

$$d\sigma = -S_s dT - \sum \Gamma_i dG_i, \tag{68}$$

which is *Gibbs' equation for surface tension*. At constant T, eq. (68) gives, for the binary system A–B in which $\Gamma_A = 0$:

$$\begin{aligned} \Gamma_B &= -\left(\frac{\partial \sigma}{\partial \overline{G}_B}\right)_T = -\left(\frac{\partial \sigma}{RT \partial \ln a_B}\right)_T \\ &= -\frac{1}{RT}\left(\frac{d\sigma}{d \ln a_B}\right). \end{aligned} \tag{69}$$

Equation (69), which is known as the *Gibbs adsorption isotherm*, indicates that any solute which lowers the surface tension has a positive value of Γ and hence is concentrated in the surface, and, conversely, any solute which raises the surface tension has a lower concentration in the surface than in the bulk phase.

The influence of dissolved oxygen on the surface tension of liquid iron at 1550°C is shown in fig. 15 as the variation of σ with the activity of oxygen relative to the 1 weight percent standard state. The surface concentration of oxygen at any concentration of oxygen in the bulk phase is obtained from the slope of the line and the Gibbs adsorption isotherm. At high oxygen contents the slope of the line approaches the constant value of −240 dyne/cm, which corresponds to saturation coverage of the surface by adsorbed oxygen. From the Gibbs adsorption isotherm this saturation coverage is calculated as

$$\Gamma_0 = 6.023 \times 10^{23} \times \frac{240}{8.3144 \times 10^7 \times 1823} = 9.5 \times 10^{14} \text{ atoms/cm}^2 .$$

9.2. The Langmuir adsorption isotherm

Consider the equilibrium between the component i in a vapor phase and i adsorbed on the surface of a condensed phase. If is is considered that the atoms of i are adsorbed on specific adsorption sites on the surface of the condensed phase, the limit of adsorption

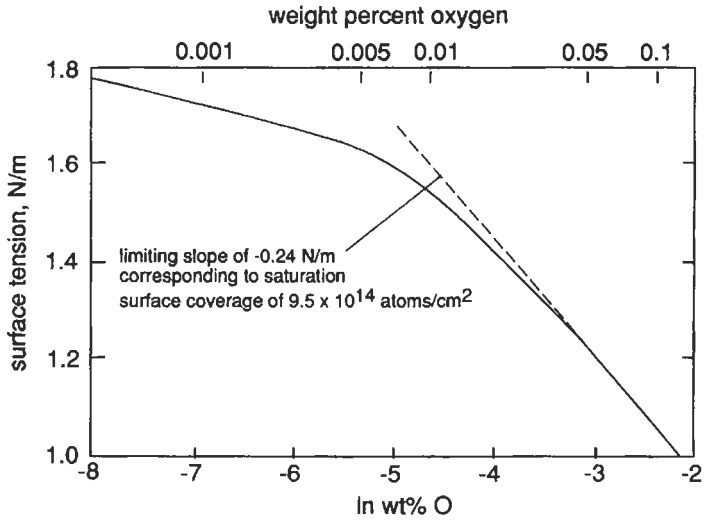

Fig. 15. The variation of the surface tension of Fe–O melts with activity of oxygen at 1550°C.

occurs when all of the available sites are occupied by adsorbed atoms. This limit corresponds to the surface being covered by a monolayer of adsorbed atoms at the surface concentration Γ_i^0. At surface concentrations, Γ_i, less than that corresponding to monolayer coverage, the fraction of surface sites occupied, θ_i (or the fractional saturation of the surface) is defined as:

$$\theta_i = \frac{\Gamma_i}{\Gamma_i^0}. \tag{70}$$

At equilibrium, the rates of adsorption and desorption of i are equal, the former being proportional to the pressure of i in the vapor phase, p_i, and the fraction of unoccupied surface sites, $(1-\theta_i)$, and the latter being proportional to the fraction of surface sites occupied by i, i.e.:

$$k_a p_i(1-\theta_i) = k_d \theta_i,$$

where k_a and k_d are the rate constants for the adsorption and desorption reactions, respectively. Thus:

$$p_i = K_i \frac{\theta_i}{1-\theta_i}, \tag{71}$$

where

$$K_i = k_d/k_a = \exp\left(-\Delta G_i^0/RT\right),$$

References: p. 469.

and ΔG_i^0 is the change in molar free energy accompanying the transfer of one mole of i from the vapor state at 1 atm pressure to the adsorbed layer on the surface at the surface concentration Γ_i^0. Equation (71), which is *Langmuir's adsorption isotherm*, shows that θ_i is proportional to p_i at small θ_i and $(1 - \theta_i)$ is inversely proportional to p_i at large θ_i.

Alternatively, eq. (71) can be written as:

$$a_i = K_i' \frac{\theta_i}{1 - \theta_i}. \tag{72}$$

BELTON has combined the Gibbs and Langmuir adsorption isotherms by substitution of eqs. (70) and (72) into eq. (69) to give:

$$\frac{d\sigma}{d \ln a_i} = -RT\, \Gamma_i = -RT\theta_i\Gamma_i^0 = -RT\, \Gamma_i^0 \frac{K_i'a_i}{1 + K_i'a_i},$$

which, on integration between the composition limits X_i' and X_i'', becomes:

$$\sigma'' - \sigma' = -RT\, \Gamma_i^0 \ln \frac{1 + K'a_i''}{1 + K'a_i'}. \tag{73}$$

If Langmuir's isotherm holds at all compositions, one limit can be taken as the pure solvent, in which case eq. (73) becomes

$$\sigma^P - \sigma = -RT\, \Gamma_i^0 \ln(1 + K'a_i). \tag{74}$$

where σ^P refers to the surface tension of the pure solvent. Curve-fitting of eq. (74) with the experimental data shown in fig. 16 and $\sigma^P = 1788$ dyne/cm, $\Gamma_O^0 = 240$ dyne/cm, gives $K' = 220$. Thus, if oxygen adsorbed on liquid iron exhibits ideal Langmuir behavior:

$$\theta_\sigma = \frac{220 \cdot [\text{wt\%O}]}{1 + 220 \cdot [\text{wt\%O}]}. \tag{75}$$

Equation (75) is shown in fig. 16 in comparison with the variation of θ_O obtained from the slopes in fig. 15 as $\theta_O = \Gamma_O / \Gamma_O^0$.

A number of applications of the Gibbs and Langmuir absorption isotherms will be found in ch. 13, §§2 and 4.

9.3. Curved interfaces

The existence of surface tension gives rise to the interesting phenomenon that the equilibrium vapor pressure exerted by a spherical droplet is a function of the radius of curvature of the droplet. This phenomenon, which was first discussed by Kelvin in 1871, is of importance with respect to the dependence of the limit of solid solution of one component in another on the particle size of the second phase.

The general equation

$$dG' = -S'dT + V'dP + \sigma dA_s + \sum \overline{G}_i dn_i \tag{63}$$

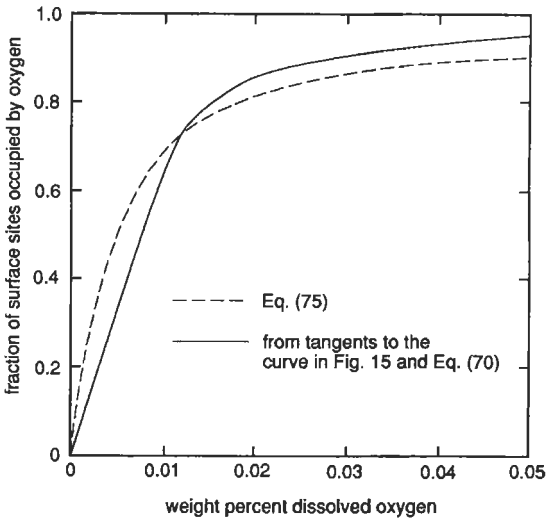

Fig. 16. The variation, at 1550°C, of the fractional coverage of the surface of liquid iron by adsorbed oxygen with concentration of oxygen in the melt.

was tacitly applied to systems containing flat interfaces. However, provided that σ is not a function of the radius of curvature of the interface, and that the interface within the system does not influence the exterior pressure, eq. (63) can be applied to the transfer of matter across curved interfaces. The *partial molar free energy*, $\overline{G}_i^*$, defined from eq. (63) as:

$$\overline{G}_i^* = \left(\frac{\partial G'}{\partial n_i}\right)_{T,P,A_s,n_j},$$

pertains to the addition of i to the system in such a manner that A_s remains constant. However, in a process involving the transfer of matter to a small spherical droplet, A_s, being dependent on the volume, and hence on the amount of matter in the droplet, is not an independent variable. The incremental increase in volume of a droplet caused by the addition of dn_i moles of the various components is:

$$dV' = \sum \overline{V}_i dn_i,$$

where $\overline{V}_i$ is the partial molar volume of i in the system. From the relationship between the surface area and the volume of a sphere,

$$dA_s = \frac{2dV'}{r} = \sum \frac{2\overline{V}_i}{r} dn_i,$$

substitution of which into eq. (63) gives:

$$dG' = -S'dT + V'dP + \sum\left(\overline{G}_i^* + \frac{2\overline{V}_i\sigma}{r}\right)dn_i.$$

Comparison with eq. (63) gives the identity

$$\overline{G}_i = G_i^* + \frac{2\overline{V}_i\sigma}{r} \tag{76}$$

as the variation of partial molar free energy with spherical particle size. From the relationship between partial molar free energy and activity, eq. (76) can be written as

$$\ln a_i = \ln a_i^* + \frac{2\overline{V}_i\sigma}{RT_r}. \tag{77}$$

In a limited terminal solid solution of B in A, in which B obeys Henry's Law, the activity of B at the limit of solubility is:

$$a_B = \gamma_B^0 X_{B(sat)},$$

and hence, from eq. (77), the solubility limit varies with particle size of the second phase as

$$\ln \frac{X_{B(sat,r)}}{X_{B(sat)}^*} = \frac{2\sigma\overline{V}_B}{RT_r}, \tag{78}$$

where $X_{B(sat,r)}$ is the solubility limit when the second phase occurs as a dispersion of spherical particles of radius r and $X_{B(sat)}^*$ is the solubility limit when the second phase is massive. Equation (78), which is known as the *Thomson–Freundlich equation*, provides a thermodynamical explanation of the phenomenon of *Ostwald ripening* (see ch. 9, § 3.2.2). When the second phase, precipitating from a primary solid solution, occurs in a range of particle sizes, it is observed that the particles of radius greater than some average value grow and that the smaller particles redissolve in the matrix. As the concentration of solute in the matrix at the interface between the matrix and a small precipitate is greater than that at the interface between the matrix and a large precipitate, a concentration, and hence activity, gradient exists between the two interfaces. This, in turn, provides the driving force for the diffusion of dissolved solute from one interface to the other, with the overall result that the larger particle grows and the smaller particle dissolves. Equation (78) is also of interest in that it indicates that no such quantity as "maximum solubility" exists.

10. The measurement of thermodynamic activity

Although activities are thermodynamic functions of state, their magnitudes and variations are determined by the interactions among the constituent particles of the system, which, in turn, determine bond energies and influence the spatial configurations assumed by the particles. Thus measurement of activities within a class of similar simple

systems can be expected to provide, at best, some fundamental understanding of the natures of these interactions or, at least, a basis for correlation of the behavior, which can then be used for extrapolation of the behavior of more complex systems.

The molar free energy of formation of a solution or compound from its pure components is obtained from the activities via eq. (44) and as the various phase equilibria occurring in a materials system are determined by the variations, with composition, temperature and pressure, of the relative free energies of the various phases, such equilibria can be most precisely determined by accurate measurement of activity. Also, the activity of a component in a solution is a measure of the minimum free energy required to convert the component from its state in solution to the pure state in any proposed extraction or refining process.

In the majority of the experimental methods the activity of only one component is measured. In such cases the activities of the other components can be obtained by integration of the Gibbs–Duhem equation. For constant temperature and total pressure this expression is $\Sigma X_i \mathrm{d} \ln a_i = 0$ or, in a more convenient form, $\Sigma X_i \mathrm{d} \ln \gamma_i = 0$ where $\gamma_i = a_i / X_i$ is the activity coefficient of i. Applied to the binary system A–B in which the variation of γ_A is known across the entire range of composition:

$$\ln \gamma_B (\text{at } X_B) = -\int_{X_B=1}^{X_B} \frac{X_A}{X_B} \mathrm{d} \ln \gamma_A . \tag{79}$$

10.1. Determination of activity by experimental measurement of vapor pressure

The experimental technique for the measurement of vapor pressure is determined by the magnitude of the pressure to be measured, and the various techniques which have been developed can be classified as *absolute methods* (direct and indirect static methods) and *indirect methods* (effusion and transpiration methods).

The earliest activity measurements were made on binary alloys of Hg with Zn, Au, Ag and Tl at temperatures near the boiling point of Hg. The partial pressure of Hg exerted by an amalgam is so much greater than the partial pressure of the other component that the former can be equated with the total vapor pressure of the amalgam. In the first studies the alloy was used as the sealing liquid in a U-tube null-point manometer. The vapor in equilibrium with the alloy is contained in the closed arm of the manometer, and hydrogen, the pressure of which is measured at a second manometer, is introduced to the other arm until the meniscuses in both arms are at the same level. The vapor pressures of amalgams at lower temperatures have been measured using various devices such as membrane manometers, quartz spiral manometers and ionization gages.

The partial pressures of Zn and Cd over α-Ag–Zn–Cd alloys and of Zn over α-brasses have been measured by resonance absorption spectroscopy. In studying the Zn alloys, light produced by a spark between Zn electrodes, is passed through a sample of vapor in equilibrium with the alloy, and the absorption of the 3076 Å resonance line is measured. As absorption of the 3035 Å resonance line does not occur, it is used as an internal standard and the vapor pressure, p, of Zn is obtained from Beer's Law as $-\ln(I_{3076}/I_{3035}) = Kpd/T$ where I is the intensity of the transmitted light, K is the absorp-

tion coefficient, T is the absolute temperature and d is the distance travelled by the light through the sample of vapor.

The *dew point method* is well-suited to systems containing a distinctly volatile component and has been applied to measurement of the activity of Zn in binary alloys containing Cu, Al, Ag, Au, Zr, Th, U, and Y, and the activity of Cd in Ag–Cd alloys. Experimentally, the alloy is placed at one end of a long initially evacuated tube which is heated to the desired temperature T_1. The temperature of the other end of the tube is lowered until condensation of the volatile component is observed at the temperature T_2. As the pressure within the tube is uniform, the partial pressure of the volatile component exerted by the alloy at T_1 equals the saturated vapor pressure of the pure volatile component at T_2. The use of fused silica tubes, which permits visual observation of condensation at the cooler end, has limited the temperature to less than 1100°C and, generally, measurements have been made in the range 400–900°C. In a similar *isopiestic technique*, the pure volatile component is placed in the cool end of an initially evacuated tube maintained in a known temperature gradient, and weighed quantities of the pure second component are placed at intervals along the temperature gradient. The volatile component is transferred from the vapor phase to the specimens of nonvolatile component until the alloys in equilibrium with the prevailing pressure of the volatile component are formed. In this technique, which has been applied to measurement of the activities of Al in solid Al–Fe and Al–Ni alloys, the compositions of the equilibrated alloys are determined gravimetrically.

Application of the dew point and isopiestic techniques to measurement of activity requires knowledge of the temperature dependence of the saturated vapor pressure of the volatile component.

In the *transpiration technique*, an inert carrier gas is passed over a sample at a flow rate which permits evaporation of the alloy to occur to the extent necessary to saturate the carrier gas. This technique has been used to measure the activities in liquid Fe–Cu and Fe–Ni alloys. The material evaporated from the sample is condensed downstream and is chemically analyzed. The total amount of evaporation into unit volume of the carrier gas at the total pressure P is determined by measuring the weight loss of the sample or by quantitative analysis of the amount of condensate recovered from a known volume of gas. If n_{Fe}, n_{Cu} and n_{He} are the numbers of moles of Fe, Cu and He carrier gas in the sampled volume, the partial pressure of Fe is calculated, from the ideal gas law, as $p_{Fe} = Pn_{Fe}/(n_{Fe} + n_{Cu} + n_{He})$. An advantage of this technique is that the activities of both components are measured and hence internal consistency of the results can be checked using the Gibbs–Duhem equation. However, in order that surface depletion of the more volatile component be avoided, the rates of diffusion in the alloy must be faster than the rates of evaporation.

In the *effusion technique* the alloy to be studied is placed in a *Knudsen cell* (a sealed crucible containing a small orifice in its lid) and the crucible is heated in vacuum to the desired temperature. Phase equilibrium is established between the vapor phase and the condensed phase in the cell and, if the dimensions of the orifice are small in comparison with the mean free path of the vapor species, the passage of vapor species through the orifice is not disturbed by collisions. Thus the rates of effusion of the vapor species are

proportional to their vapor pressures within the cell. From gas kinetic theory, the number of particles in a vapor phase striking unit area of the containing wall in unit time is $0.25n\bar{c}$, where n is the density of vapor species and $\bar{c} = (8RT/\Pi M)^{1/2}$ is the average speed of the particles. Consequently, the *weight loss*, W, due to effusion through an orifice of area A in time t is $pAt/(2\Pi MRT)^{1/2}$ and hence the pressure, p, of the species in the cell is $p = (W/At)(2\Pi RT/M)^{1/2}$. If a radioactive tracer is added to the alloy, very small amounts of effusing substance can be detected. For example, gamma-ray spectrometry of neutron-irradiated Au–Cu alloys has facilitated estimation of quantities as small as 10^{-10} g.

The transpiration and effusion techniques require that the molecular weights of the vapor species be known and hence they can only be used to study systems in which no complex vapor molecules are formed.

The problems caused by complex molecule formation can be eliminated by mass-spectrometric analysis of the vapor effusing from the Knudsen cell. In the *Knudsen cell-time of flight mass-spectrometer* combination, the beam of particles effusing from the cell is introduced to the ionization chamber of the mass-spectrometer through a slit. Ionization is produced by a pulsing electron beam and after each pulse the ionization chamber is cleared of ions by a pulse of small negative potential. The ions are then subjected to a continuously maintained high negative potential which accelerates them into a field-free drift tube, and the time required for a given ion to traverse the drift tube and be detected is proportional to $(m/e)^{1/2}$. The ion current, I_i^+, measured for the species i is related to the vapor pressure of i as:

$$p_i = KI_i^+T, \tag{80}$$

where the constant K is determined by the ionization cross-section of the ion, the detector sensitivity and the geometry of the Knudsen cell-ion source. The application of the technique to measurement of activities in binary systems was greatly facilitated by a manipulation of the Gibbs–Duhem equation which allows the variations, with composition, of the activity coefficients of the individual components to be obtained from the corresponding measured ratio of the activity coefficients as:

$$\ln \gamma_B(\text{at } X_B) = -\int_1^{X_B} X_A \, d \ln \frac{\gamma_A}{\gamma_B}. \tag{81}$$

From eq. (80):

$$\frac{I_A^+}{I_B^+} \propto \frac{p_A}{p_B} \propto \frac{a_A}{a_B} \frac{\gamma_A X_A}{\gamma_B X_B},$$

substitution of which into eq. (81) gives:

$$\ln \gamma_B(\text{at } X_B) = -\int_1^{X_B} X_A \, d\left(\ln \frac{I_A^+}{I_B^+} - \frac{X_A}{X_B} \right).$$

Use of a mass-spectrometer requires that a pressure of less than 10^{-8} atm be maintained in the areas of the ion source, analyzer and detector. This technique has been applied to

References: p. 469.

measurement of activities in a large number of binary and ternary systems containing V, Cr, Fe, Co, Ni, Cu, Ag, Au, Al, Tl, Pb, Sn, Bi, Sb, and In.

10.2. Determination of activity by establishing heterogeneous equilibrium

Heterogeneous equilibrium at constant temperature and pressure requires that the partial molar free energy, and hence activity, of each component of the system be the same in each of the phases present, i.e., a_i (in phase I) $= a_i$ (in phase II) $= a_i$ (in phase III) $= \ldots$. Thus, if the activity of a component can be fixed at a known value in any one of the phases, its value in every other phase is known.

One of the more simple heterogeneous equilibria involves a binary liquid, saturated with one of its components. In a simple binary eutectic system exhibiting virtually complete mutual immiscibility in the solid state, the saturated liquids on the liquidus lines are in equilibrium with virtually pure solids. Thus, in the melt of A-liquidus composition at the liquidus temperature T, the activity of A relative to pure liquid A as the standard state equals the activity of pure solid A relative to liquid A as the standard state, both being given by $a_A = \exp(-\Delta G^0_{m,A}/RT)$ where $\Delta G^0_{m,A}$ is the molar free energy of melting of A at temperature T. Activities have been calculated in this manner along liquidus lines in such systems as Ag–Si and Ag–Pb.

Fe and Ag are virtually immiscible in the liquid state, and when Si is added as a solute to coexisting liquid Fe and Ag it is distributed between the two liquids such that its activity is the same in both phases. The activities of Si in liquid Fe and liquid Fe–C alloys have been determined by chemical analysis of equilibrated Fe and Ag liquids containing Si, and knowledge of the activity of Si in Ag–Si alloys. In a similar manner the activity of Ag in Al–Ag alloys has been determined from measurement of the equilibrium partitioning of Ag between the virtually immiscible liquids Al and Pb, and the activity of Al in Al–Co alloys has been determined by partitioning Al between the virtually immiscible liquids Ag and Co.

The respective equilibrium constants for the reactions $CO_2 + C_{(graphite)} = 2CO$ and $CO + \frac{1}{2}O_2 = CO_2$ are:

$$K_4 = \frac{p^2_{CO}}{p_{CO_2} a_C} \tag{82}$$

and

$$K_5 = \frac{p_{CO_2}}{p_{CO} p^{1/2}_{O_2}}. \tag{83}$$

Thus, at a fixed temperature, which determines the values of K_4 and K_5, a CO–CO_2 gas mixture of known p_{CO} and p_{CO_2} has an activity of carbon given by eq. (82) and a partial pressure of oxygen given by eq. (83). Similarly, by virtue of the equilibrium $H_2 + \frac{1}{2}O_2 = H_2O$, an H_2–H_2O mixture of known p_{H_2} and p_{H_2O} exerts a unique partial pressure of oxygen at any temperature; by virtue of the equilibrium $H_2 + \frac{1}{2}S_2 = H_2S$, an H_2–H_2S mixture of known p_{H_2} and p_{H_2S} exerts a unique partial pressure of sulfur at any temperat-

ure; and, by virtue of the equilibrium $C_{(graphite)} + 2H_2 = CH_4$, a CH_4–H_2 mixture of known p_{CH_4} and p_{H_2} has a unique activity of carbon at any temperature. Consequently, CO–CO_2 and CH_4–H_2 mixtures can be used as gas phases of fixed activity of carbon for use in the establishment of heterogeneous equilibria between a gas phase and a condensed phase. Similarly, CO–CO_2 and H_2–H_2O mixtures can be used as gas phases of fixed oxygen pressure and H_2–H_2S mixtures can be used as gas phases of fixed sulfur pressure. The activities of carbon in liquid and solid iron have been determined by equilibrating iron with CO–CO_2 and CH_4–H_2 mixtures and measuring the equilibrium carbon content of the metal phase, and the activities of oxygen and sulfur in liquid iron have been determined by equilibrating iron with H_2O–H_2 and H_2S–H_2 mixtures, respectively. In more simple gas–metal equilibria the activities of hydrogen and nitrogen in iron have been determined by measuring the solubilities of the gases as functions of gas pressure. Activities in the system Fe–Fe_2O_3 have been determined by experimental observation of the variation of the composition of small samples of condensed phases with temperature and oxygen pressure imposed by an equilibrating gas phase. The variation, with composition, of the activity of Fe in the system is determined by Gibbs–Duhem integration of the corresponding measured variation of the equilibrium partial pressure of oxygen. The oxygen content of liquid iron in equilibrium with pure liquid iron oxide at 1600°C is 0.23 wt%. If the oxide of a less noble metal than iron is dissolved in the liquid iron oxide, the activity of iron oxide, and hence the equilibrium oxygen content of the liquid iron are decreased. If the latter is x wt%, the activity of FeO, relative to pure Fe-saturated iron oxide as the standard state, in the oxide solution is $x/0.23$. This technique has been used to determine the activity of FeO in CaO–FeO and CaO–FeO–SiO_2 melts saturated with liquid iron.

One step more complex is the establishment of equilibrium between a gas phase and two condensed phases. The equilibrium between manganese, manganous oxide and a CO–CO_2 mixture, expressed as $Mn + CO_2 = MnO + CO$ requires:

$$K = \frac{p_{CO} a_{MnO}}{p_{CO_2} a_{Mn}}. \tag{84}$$

Thus, at a given temperature, the equilibrium between pure Mn (at unit activity) and Mn-saturated pure MnO (at unit activity) occurs at a unique value of the ratio p_{CO}/p_{CO_2} given by eq. (84). If a metal more noble than Mn is embedded in an excess of MnO and subjected to a lower p_{CO}/p_{CO_2} ratio, manganese is transferred from the MnO to the metal phase until the activity of Mn required by eq. (84) and the imposed p_{CO}/p_{CO_2} is established. The manganese content of the alloy corresponding to the imposed activity is determined by chemical analysis. The other component of the alloy must be sufficiently more noble than Mn that formation and solution of its oxide in the MnO phase is negligible. The activity of Mn in Mn–Pt alloys has been determined in this manner. Having determined this relationship, the activity of MnO in oxide melts containing oxides more stable than MnO can be determined by equilibrating a small sample of Pt with an excess of oxide melt and a CO–CO_2 gas mixture. Again, as Mn is distributed between the Pt–Mn alloy and the oxide melt in accordance with eq. (84) and the imposed

References: p. 469.

p_{CO}/p_{CO_2}, chemical analysis of the equilibrated Pt–Mn alloy yields a_{Mn} and hence, from eq. (84), the value of a_{MnO} in the oxide melt. In this application the other oxide component must be of a metal which is sufficiently less noble than Mn that the extent of its solution in the Pt Mn phase is negligible. This technique has been used to determine the activity of MnO in systems such as $MnO–SiO_2$, $MnO–TiO_2$, $MnO–Al_2O_3$, $MnO–B_2O_3$ and $MnO–CaO–SiO_2$.

Other examples of determination of activities by establishing equilibrium between a binary alloy, a nonmetallic phase of known composition and a gas phase include:

$$\begin{aligned}
&\text{Fe(in Fe–Ni alloys)} + H_2O = FeO + H_2;\\
&2\text{Cr(in Cr–Ni alloys)} + 3H_2O = Cr_2O_3 + 3H_2;\\
&3\text{Mn(in Mn–Cu alloys)} + CH_4 = Mn_3C + 2H_2;\\
&2\text{Cu(in Cu–Au alloys)} + H_2S = Cu_2S + H_2;\\
&3\text{Si(in Si–Ag alloys)} + N_2\ (\text{in } N_2–H_2 \text{ mixtures}) = Si_3N_4.
\end{aligned} \tag{85}$$

Again, in this application, the "inert" metal must be sufficiently more noble than the primary component metal that its occurrence in the equilibrium nonmetallic phase is negligible. Corrections are required in systems where the nonmetallic phase is not a line compound. Thus, for example, in eq. (85), the activity of FeO is that in the wustite equilibrated with the imposed partial pressure of oxygen, relative to Fe-saturated wustite as the standard state. Equation (85) has also been used to determine the activity of FeO in $FeO–SiO_2$ melts by establishing the equilibrium $Fe + H_2O = FeO$ (in $FeO–SiO_2$ melts) $+ H_2$.

If the difference between the nobilities of the metals is small enough that an oxide solution is produced in equilibrium with the binary alloy phase a different approach is taken. For example, if a small specimen of an Fe–Mn alloy is equilibrated with an excess of an FeO–MnO solid solution, the exchange equilibrium $Fe + MnO = Mn + FeO$ is established, wherein $K = a_{Mn}a_{FeO}/a_{Fe}a_{MnO}$. From chemical analysis of the equilibrated Fe–Mn alloy and knowledge of the activities in the system Fe Mn, the ratio $\gamma_{FeO}/\gamma_{MnO}$ in the equilibrating oxide solution is obtained as:

$$\frac{\gamma_{FeO}}{\gamma_{MnO}} = K\frac{a_{Fe}X_{MnO}}{a_{Mn}X_{FeO}},$$

and Gibbs–Duhem integration of the variation of this ratio with composition in the oxide solution according to eq. (81) yields the individual activity coefficients, and hence activities, of the components of the oxide solution. This technique has been used to determine activities in the systems $Fe_2SiO_4–Co_2SiO_4$ and $Fe_2SiO_4–Mn_2SiO_4$.

Activities have been determined by establishing equilibrium among three condensed phases and a gas phase. As an example, the activity of SiO_2 in $CaO–MgO–Al_2O_3–SiO_2$ melts has been determined by establishing the equilibrium

$$SiO_2 + 2C = Si + 2CO \tag{86}$$

in systems comprising a silicate melt, solid graphite, liquid iron and CO gas at 1 atm pressure, and by establishing the equilibrium

$$SiO_2 + 2SiC = 3Si + 2CO \tag{87}$$

in systems comprising a silicate melt, solid SiC, liquid iron and CO gas at 1 atm pressure. The activity of SiO_2 is obtained from chemical analysis of the equilibrated liquid phases, knowledge of the equilibrium constants for the reactions given by eqs. (86) and (87) and knowledge of the activity of Si in Fe–Si–C melts. Gibbs–Duhem integration of the results yielded activities in the systems $CaO–SiO_2$, $CaO–Al_2O_3$, $MgO–SiO_2$, $CaO–Al_2O_3–SiO_2$, $MgO–CaO–SiO_2$ and $MgO–Al_2O_3–SiO_2$.

10.3. Electrochemical measurement of activity

The EMF of a reversible galvanic cell, ε, is related to the free energy change, ΔG, for the cell reaction as $\Delta G = -z F \varepsilon$ where F is Faraday's constant and z is the number of Faradays required for the cell reaction. Thus, in a concentration cell of the type

pure metal A | ionic conductor containing metal A ions of valence z_A | alloy A–B,

the cell reaction is A(pure) $\rightarrow$ A(in the A–B alloy) for which $\Delta G = RT \ln a_A$ (in the A B alloy). Thus the activity of A in the alloy is obtained as $\ln a_A = -(z_A F \varepsilon / RT)$. The determination of activity by measurement of the EMF of an electrochemical cell requires that the electrolyte be a purely ionic conductor and that the valency z_A be defined. A further requirement is that the extent of the exchange reaction at the cathode–electrolyte interface between B in the alloy and A in the electrolyte be negligible. If this condition is not met, the measured EMF contains a contribution of unknown magnitude arising from the transfer of electrolyte between regions of different composition. In practice the extent of the exchange reaction is rendered negligible by ensuring that B is significantly more noble than A. Molten chlorides are purely ionic conductors and hence these melts are popular as liquid electrolytes. The concentrations of low valent cations in the electrolyte are minimized by dissolving the chlorides in mixtures of alkali chlorides.

The activity of Al in Al–Ag melts in the range 700–800°C has been obtained from measurement of the EMFs of cells of the type

$$Al_{(l)} \,|\, Al^{3+}(\text{in KCl–NaCl}) \,|\, Al–Ag_{(l)}.$$

Similarly the activities of Cd in Cd–Pb, Cd–Bi, Cd–Sb and Cd–Sn alloys, and the activities of Cu in Cu–Au melts and Ag in Ag–Au melts have been determined from concentration cells with liquid chloride electrolytes.

The cell

$$Mg_{(l)} \,|\, MgCl_{2(l)} \,|\, Cl_{2(g,1\ atm)}$$

is a formation cell in which the cell reaction is $Mg + Cl_2 = MgCl_2$. With pure liquid Mg, pure liquid $MgCl_2$ and Cl_2 at 1 atm pressure, the free energy change is the standard free energy change, ΔG^0, and the EMF is the standard EMF, $\varepsilon^0 = -\Delta G^0 / 2F$. Alloying the anode with a more noble metal such as Al alters the free energy change for the cell reaction to $\Delta G = \Delta G^0 - RT \ln a_{Mg}$ (in the alloy) and hence the cell EMF to

$$\varepsilon = \varepsilon^0 + \frac{RT}{2F} \ln a_{Mg} \text{ (in the alloy)}. \tag{88}$$

References: p. 469.

Equation (88) has been used to determine the activities of Mg in Mg–Al melts from EMF measurements in the range 700–880°C.

Similarly, the formation cell

$$Pb_{(l)} | PbO_{(l)} | O_{2(g,1\ atm)}$$

has a standard EMF of $\varepsilon^0 = -\Delta G^0/2F$. Alloying the PbO electrolyte with the oxide of a less noble metal, such as SiO_2, changes the cell EMF to:

$$\varepsilon = \varepsilon^0 - \frac{RT}{2F} \ln a_{PbO} \text{ (in PbO–SiO}_2\text{)},$$

and this has been used as the basis for electrochemical determination of the activities in the system PbO–SiO_2 in the range 850–1050°C.

Within wide ranges of temperature and oxygen pressure, ZrO_2 and ThO_2 in the fluorite structure, stabilized by solid solution with CaO and Y_2O_3, respectively, exhibit unusually high conductivities and transport numbers for O^{2-} of essentially unity. Consequently CaO–ZrO_2 and Y_2O_3–ThO_2 have been used as solid electrolytes in oxygen concentration cells of the type

$$Pt,\ O_{2(g,\text{ at pressure } P_1)} | CaO\text{–}ZrO_2 | O_{2(g,\text{ at pressure } P_2)},\ Pt,$$

in which the cell reaction is $O_{2(g,\text{at pressure } P1)} \rightarrow O_{2(g,\text{at pressure } P2)}$ and the cell EMF is $\varepsilon = -\Delta G/4F = -(RT/4F) \ln P_2/P_1$. The oxygen pressure at the electrodes can be fixed by using equilibrated metal–metal–oxide couples, e.g., with Fe–FeO and Ni–NiO the cell becomes

$$Fe,\ FeO | CaO\text{–}ZrO_2 | Ni,\ NiO,$$

with a cell reaction of NiO + Fe = FeO + Ni. With the electrodes Fe–FeO and (Fe–Ni)–FeO, the cell reaction is $Fe_{(pure)} \rightarrow Fe_{(\text{in the Fe–Ni alloy})}$ and the cell EMF is

$$\varepsilon = -\frac{RT}{2F} \ln a_{Fe} \text{ (in the alloy)}. \tag{89}$$

This method is similar to that discussed in connection with eq. (85). In the chemical equilibration technique the oxygen pressure is imposed, and the Fe–Ni alloy in equilibrium with FeO and the imposed oxygen pressure is produced in the experimental apparatus. In the EMF technique the oxygen pressure in equilibrium with a given Fe–Ni alloy and FeO is measured. Equation (89) has been used as the basis for electrochemical determination of the activities in a large number of solid and liquid binary alloy systems, the majority of which contained Fe, Co, Ni or Cu as the less noble metal. The activity of Si in Fe–Si alloys at 1550°C and 1600°C has been determined with electrodes of Cr, Cr_2O_3 and SiO_2, Fe–Si and activities in the systems Ta–W and Ta–Mo have been determined with a Y_2O_3–ThO_2 electrolyte and Ta, Ta_2O_5 and Ta–X, Ta_2O_5 electrodes. The activities of SnO in SnO–SiO_2 melts and PbO in PbO–SiO_2 melts have been determined from cells of the type M, MO|CaO–ZrO_2|M, MO–SiO_2.

Other solid electrolytes which have been used include β-alumina and soft soda glass for measurement of the activity of sodium in alloys, and glasses containing K^+ and Ag^+

for study of K and Ag alloys, respectively. It can be expected that, as new solid state electrolytes are developed for possible use in fuel cells, they will be applied to the determination of activities by EMF measurements.

Bibliography

ALCOCK, C. B., Principles of Pyrometallurgy (Academic Press, London, 1976).

BELTON, G. R., Langmuir Adsorption, the Gibbs Adsorption Isotherm and Interfacial Kinetics in Liquid Metal Systems, Metallurg. Trans. **B7** (1976) 35.

BELTON, G. R., and R. J. FRUEHAN, The Determination of Activities by Mass-Spectrometry – Some Additional Methods, Metallurg. Trans. **2** (1971) 291.

CALLEN, H. B., Thermodynamics (Wiley, New York, 1960).

CHANDRASEKHARAIAH, M. S., O. M. SREEDHARAN and E. CHATTOPADHYAY, Thermodynamic Studies of Alloys and Intermetallic Compounds, in: Solid Electrolytes and Their Applications, ed. E. C. Subbarao (Plenum, New York, 1980).

ELLINGHAM, H. J. T., Reducibility of Oxides and Sulfides in Metallurgical Processes, J. Soc. Chem. Ind. **63** (1944) 125.

ELLIOTT, J. F., Physical Chemistry of Liquid Metal Solutions, in: Metallurgical Treatises, eds. J. F. Elliott and J. Tien (The Metallurgical Society of AIME, Warrendale, PA, 1981).

ELLIOTT, J. F., M. GLEISER and V. RAMAKRISHNA, Thermochemistry for Steelmaking (Addison Wesley, Reading, MA, 1963).

FAST, J. D., Entropy (McGraw Hill, New York, 1962).

GASKELL, D. R., Introduction to Metallurgical Thermodynamics, 2nd Ed. (McGraw–Hill, New York, 1981).

GOKCEN, N. A., Thermodynamics (Techscience, Hawthorne, CA, 1977).

HULTGREN, R., P. D. DESAI, D. T. HAWKINS, M. GLEISER and K. K. KELLEY, Selected Values of the Thermodynamic Properties of Binary Alloys (American Society for Metals, Metals Park, OH, 1973).

KUBASCHEWSKI, O., C. B. ALCOCK and P. J. SPENCER, Materials Thermochemistry, 6th Ed. (Pergamon Press, New York, 1993).

LEWIS, G. N., and M. RANDALL, Thermodynamics, 2nd Ed., revised by K. S. Spitzer and L. Brewer (McGraw–Hill, New York, 1961).

LUPIS, C. H. P., Chemical Thermodynamics of Materials (North–Holland, Amsterdam, 1983).

MOORE, J. J., Chemical Metallurgy, 2nd Ed. (Butterworths, London, 1990).

ROSENQUIST, T., Principles of Extractive Metallurgy (McGraw–Hill, New York, 1974).

STEINER, A., and K. L. KOMAREK, Thermodynamic Activities in Solid Ni–Al Alloys, Trans. Metallurg. Soc. AIME **230** (1964) 786.

SWALIN, R. A., Thermodynamics of Solids, 2nd Ed. (Wiley, New York, 1972).

TURKDOGAN, E. T., Physical Chemistry of High Temperature Technology (Academic, New York, 1980).

WAGNER, C., Thermodynamics of Alloys (Addison–Wesley, Reading, MA, 1952).

CHAPTER 6

PHASE DIAGRAMS

ARTHUR D. PELTON

Département de Génie Métallurgique
Ecole Polytechnique, Case Postale 6079, Station "Centre Ville"
Montréal, Québec H3C 3A7, Canada

R. W. Cahn and P. Haasen†, eds.
Physical Metallurgy; fourth, revised and enhanced edition

1. Introduction

The study of phase equilibria and phase transformations is central to nearly all branches of metallurgy and materials science. Although departures from equilibrium will occur in any real system, a knowledge of the equilibrium state under a given set of conditions is the starting point for the understanding of most processes.

A phase diagram is a graphical representation of the loci of thermodynamic variables when equilibrium among the phases of a system is established under a given set of conditions. The phase diagrams most familiar to the metallurgist are those for which temperature and composition are the axes. These are discussed in §§ 2 and 3 for binary (two-component) and ternary (three-component) systems, and in § 4 for multicomponent systems. However, the effect of other variables such as total pressure and chemical potential of the components (e.g., the partial pressure of oxygen) may often be of interest. In § 6, different types of phase diagrams are discussed along with the general rules governing their construction.

Throughout the chapter, the thermodynamic origin of phase diagrams is stressed. With the advent of modern computer techniques, the relationship between phase diagrams and the thermodynamic properties of the system has become of increasing practical importance. As discussed in § 2.10, a quantitative coupling of the two is now possible. Furthermore, as discussed in § 5, the computer-assisted thermodynamic approach often permits good estimates of unknown multicomponent phase diagrams to be made, and can often significantly reduce the experimental effort required to measure the phase diagram of a system.

2. Binary phase diagrams

The temperature composition (T–X) phase diagram of the Bi–Sb system is shown in fig. 1 (HULTGREN *et al.* [1963]). The abscissa is the composition, expressed as *mole fraction* of Sb, X_{Sb}. Note that $X_{Sb} = 1 - X_{Bi}$. Phase diagrams are also often drawn with the composition axis expressed as weight percent.

At all compositions and temperatures in the area above the line labelled *liquidus*, single-phase liquid alloys will be observed, while at all compositions and temperatures

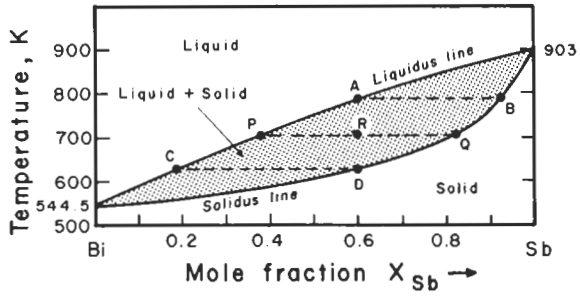

Fig. 1. Phase diagram of the Bi–Sb system (after HULTGREN *et al.* [1963]).

below the line labelled *solidus*, alloys exist as single-phase solid solutions. An alloy sample at equilibrium at a temperature and overall composition between these two curves will consist of a mixture of solid and liquid phases, the compositions of which are given by the liquidus and solidus compositions at that temperature. For example, a Bi–Sb sample of overall composition $X_{Sb} = 0.60$ at $T = 700$ K (at point R in fig. 1) will consist, at equilibrium, of a mixture of liquid alloy of composition $X_{Sb} = 0.37$ (point P) and solid alloy of composition $X_{Sb} = 0.82$ (point Q). The line PQ is called a *tie-line* or *conode*. As the overall composition is varied at 700 K between points P and Q, the compositions of the liquid and solid phases remain fixed at P and Q, and only the relative proportions of the two phases change. From a simple mass balance, one can derive the *lever rule* for binary systems: (moles of liquid)/(moles of solid) = RQ/PR. Hence, at 700 K a sample of Bi–Sb alloy with overall composition $X_{Sb} = 0.60$ consists of liquid and solid phases in the molar ratio $(0.82 - 0.60)/(0.60 - 0.37) = 0.96$. Were the composition axis expressed as weight percent, then the lever rule would give the weight ratio of the two phases.

Suppose that a liquid Bi–Sb alloy with composition $X_{Sb} = 0.60$ is cooled very slowly from an initial temperature of 900 K. When the temperature has decreased to the liquidus temperature of 780 K (point A) the first solid appears, with a composition at point B ($X_{Sb} = 0.93$). As the temperature is decreased further, solid continues to precipitate with the compositions of the two phases at any temperature being given by the liquidus and solidus compositions at that temperature and with their relative proportions being given by the lever rule. Solidification is complete at 630 K, the last liquid to solidify having composition $X_{Sb} = 0.18$ (point C).

The process just described is known as equilibrium cooling. At any temperature during equilibrium cooling the solid phase has a uniform (homogeneous) composition. In the preceding example, the composition of the solid phase during cooling varies along the line BQD. Hence, in order for the solid particles to have a uniform composition at any temperature, diffusion of Sb from the center to the surface of the growing particles must occur. Since solid state diffusion is a relatively slow process, equilibrium cooling conditions are only approached if the temperature is decreased very slowly. If a Bi–Sb alloy of composition $X_{Sb} = 0.60$ is cooled very rapidly from the liquid, concentration gradients will be observed in the solid grains, with the concentration of Sb decreasing towards the surface from a maximum of $X_{Sb} = 0.93$ (point B) at the center. Furthermore, in this case solidification will not be complete at 630 K since at 630 K the average concentration of Sb in the solid particles will now be greater than $X_{Sb} = 0.60$. These considerations are discussed more fully in ch. 9.

At $X_{Sb} = 0$ and $X_{Sb} = 1$ in fig. 1 the liquidus and solidus curves meet at the equilibrium melting points, or *temperatures of fusion*, of Bi and Sb, which are: $T^0_{f(Bi)} = 544.5$ K, $T^0_{f(Sb)} = 903$ K.

The phase diagram is influenced by the total pressure, P. Unless otherwise stated, T–X diagrams for alloy systems are usually presented for $P = \text{const.} = 1$ atm. However, for equilibria involving only solid and liquid phases, the phase boundaries are typically shifted only by the order of a few hundredths of a degree per bar change in P (see ch. 5, § 3). Hence, the effect of pressure upon the phase diagram is generally negligible

References: p. 531.

unless the pressure is of the order of hundreds of atmospheres. On the other hand, if gaseous phases are involved then the effect of pressure is very important (§ 2.12).

2.1. The thermodynamic origin of phase diagrams

In this section we shall consider first of all the thermodynamic origin of simple "lens-shaped" phase diagrams in binary systems with complete liquid and solid miscibility.

An example of such a diagram was given in fig. 1. Another example is the Ge–Si phase diagram in the lowest panel of fig. 2 (HANSEN [1958]). In the upper three panels of fig. 2 are shown, to scale, the molar Gibbs energies of the solid and liquid phases, g^s and g^l, at three temperatures. As illustrated in the top panel, g^s varies with composition

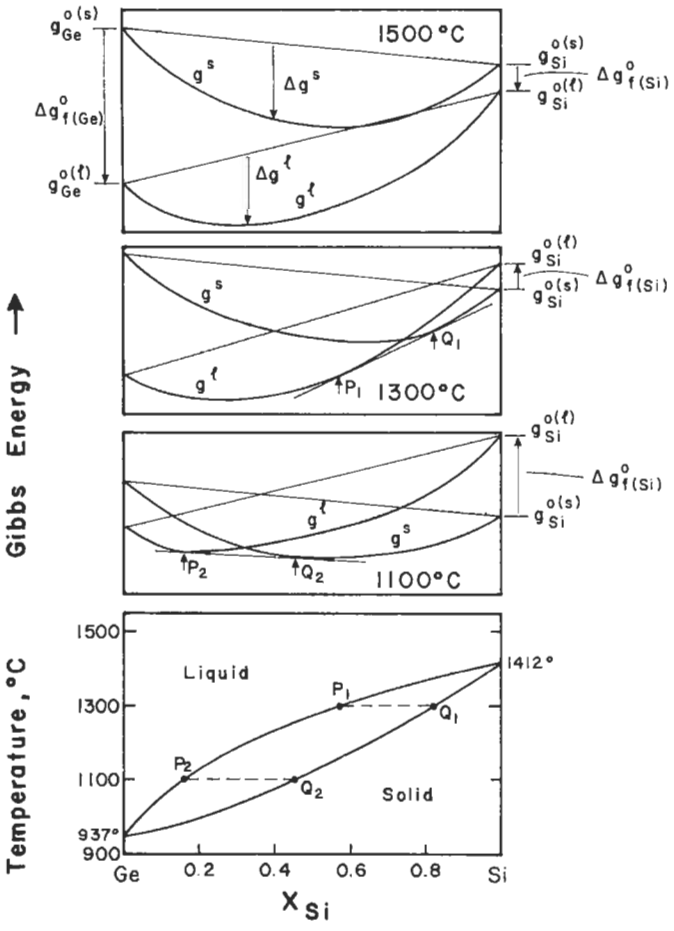

Fig. 2. Ge–Si phase diagram (after HANSEN [1958]) and Gibbs energy-composition curves at three temperatures, illustrating the common tangent construction.

between the standard molar Gibbs energies of pure solid Ge and of pure solid Si, $g_{Ge}^{0(s)}$ and $g_{Si}^{0(s)}$, while g^l varies between the standard molar Gibbs energies of the pure liquid components $g_{Ge}^{0(l)}$ and $g_{Si}^{0(l)}$. The molar *Gibbs energies of mixing* of the solid and liquid phases, Δg^s and Δg^l, are negative and are equal to the difference between the Gibbs energy of the solution and a simple weighted average of the Gibbs energies of the pure unmixed components in each phase.

The difference between $g_{Si}^{0(l)}$ and $g_{Si}^{0(s)}$ is equal to the standard molar Gibbs energy of fusion (melting) of pure Si, $\Delta g_{f(Si)}^0 = (g_{Si}^{0(l)} - g_{Si}^{0(s)})$. Similarly for Ge, $\Delta g_{f(Ge)}^0 = (g_{Ge}^{0(l)} - g_{Ge}^{0(s)})$. The Gibbs energy of fusion of a pure component may be written as:

$$\Delta g_f^0 = \Delta h_f^0 - T\Delta s_f^0, \tag{1}$$

where Δh_f^0 and Δs_f^0 are the standard molar enthalpy and entropy of fusion. Since, to a first approximation, Δh_f^0 and Δs_f^0 are independent of T, Δg_f^0 is approximately a linear function of T. If $T > T_f^0$, then Δg_f^0 is negative. If $T < T_f^0$, then Δg_f^0 is positive. Hence, as seen in fig. 2, as T decreases, the g^s curve descends relative to g^l. At 1500°C, $g^l < g^s$ at all compositions. Therefore, by the principle that a system always seeks the state of minimum Gibbs energy at constant T and P, the liquid phase is stable at all compositions at 1500°C. At 1300°C, the curves of g^s and g^l cross. The line P_1Q_1, which is the *common tangent* to the two curves, divides the composition range into three sections. For compositions between pure Ge and P_1, a single-phase liquid is the state of minimum Gibbs energy. For compositions between Q_1 and pure Si, a single-phase solid solution is the stable state. Between P_1 and Q_1, total Gibbs energies lying on the tangent line P_1Q_1 may be realized if the system adopts a state consisting of two phases with compositions at P_1 and Q_1 and with relative proportions given by the lever rule. Since the tangent line P_1Q_1 lies below both g^s and g^l, this two-phase state is more stable than either phase alone. Furthermore, no other line joining any point on g^l to any point on g^s lies below the line P_1Q_1. Hence, this line represents the true equilibrium state of the system, and the compositions P_1 and Q_1 are the liquidus and solidus compositions at 1300°C.

It may be shown that the common tangency condition also results in equal *activities* of each component in the two phases at equilibrium. That is, equality of activities and minimization of total Gibbs energy are equivalent criteria for equilibrium between phases.

As T is decreased to 1100°C, the points of common tangency are displaced to higher concentrations of Ge. For $T < 937$°C, $g^s < g^l$ at all compositions.

It should be noted that absolute values of Gibbs energies cannot be defined. Hence, the relative positions of $g_{Ge}^{0(l)}$ and $g_{Si}^{0(l)}$ in fig. 2 are completely arbitrary. However, this is immaterial for the preceding discussion, since displacing both $g_{Si}^{0(l)}$ and $g_{Si}^{0(s)}$ by the same arbitrary amount relative to $g_{Ge}^{0(l)}$ and $g_{Ge}^{0(s)}$ will not alter the compositions of the points of common tangency.

It should also be noted that in the present discussion of equilibrium phase diagrams we are assuming that the physical dimensions of the single-phase regions in the system are sufficiently large that surface (interfacial) energy contributions to the Gibbs energy can be neglected. For very fine grain sizes in the sub-micron range however, surface energy effects can noticeably influence the phase boundaries.

References: p. 531.

The shape of the two-phase (solid + liquid) "lens" on the phase diagram is determined by the Gibbs energies of fusion, Δg_f^0 of the components and by the mixing terms, Δg^s and Δg^l. In order to observe how the shape is influenced by varying Δg_f^0, let us consider a hypothetical system A–B in which Δg^s and Δg^l are ideal Raoultian (§ 2.2). Let $T_{f(A)}^0 = 800$ K and $T_{f(B)}^0 = 1200$ K. Furthermore, assume that the entropies of fusion of A and B are equal and temperature-independent. The enthalpies of fusion are then given from eq. (1) by the expression $\Delta h_f^0 = T_f^0 \Delta s_f^0$ since $\Delta g_f^0 = 0$ when $T = T_f^0$. Calculated phase diagrams for $\Delta s_f^0 = 3$, 10 and 30 J/mol K are shown in fig. 3. A value of $\Delta s_f^0 \approx 0$ is typical of most metals (*Richard's rule*). However, when the components are ionic compounds such as ionic oxides, halides, etc., then Δs_f^0 can be significantly larger since there are several atoms per formula unit. Hence, two-phase "lenses" in binary ionic salt or oxide phase diagrams tend to be "fatter" than those encountered in alloy systems. If we are considering vapour–liquid equilibria rather than solid–liquid equilibria, then the shape is determined by the entropy of vaporization, Δs_V^0 (§ 2.12). Since $\Delta s_V^0 \approx 10 \Delta s_f^0$, two-phase (liquid + vapour) lenses tend to be very wide.

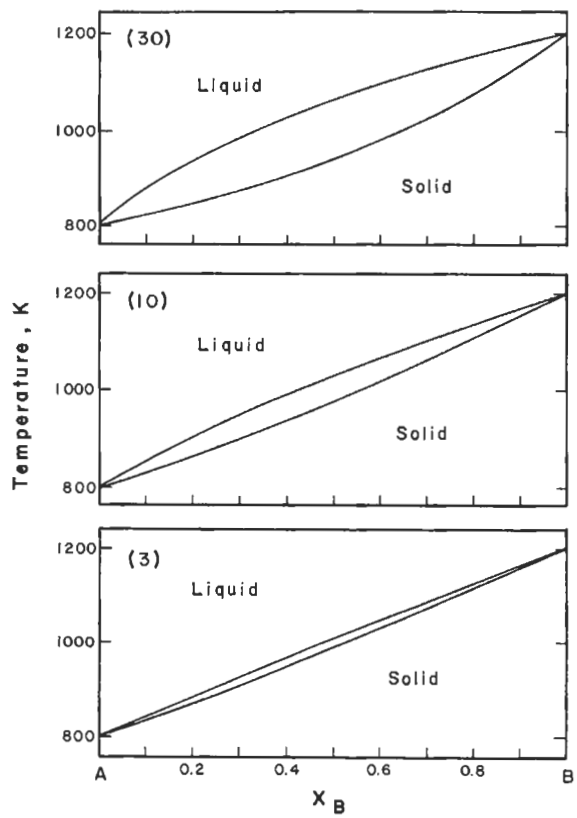

Fig. 3. Phase diagrams for a system A–B with ideal solid and liquid solutions with $T^o_{f(A)} = 800$ K and $T^o_{f(B)} = 1200$ K, calculated for entropies of fusion $\Delta s^o_{f(A)} = \Delta s^o_{f(B)} = 3$, 10 and 30 J/mol K.

2.2. Minima and maxima in two-phase regions

As discussed in ch. 6, § 6, the Gibbs energies of mixing, Δg^s and Δg^l, may each be expressed as the sum of an ideal (Raoultian) term which is purely entropic and which is given by the Boltzmann equation for a random substitutional solution of A and B particles, and an *excess* term, g^E.

$$\Delta g = RT(X_A \ln X_A + X_B \ln X_B) + g^E, \tag{2}$$

where X_A and X_B are the mole fractions of the components. An *ideal* or *Raoultian* solution is defined as one in which $g^E = 0$. Both the solid and liquid phases in the Ge–Si system (fig. 2) are approximately ideal. With two ideal solutions, a "lens-shaped" two-phase region always results. However, in most alloy systems, even approximately ideal behaviour is the exception rather than the rule.

If $g^E > 0$ then the system is said to exhibit positive deviations from ideality. If $g^E < 0$, then we speak of negative deviations.

Curves of g^s and g^l for a hypothetical system A–B are shown schematically in fig. 4 at a constant temperature below the melting points of pure A and B such that the solid state is the stable state for both pure components. However, in this system $g^{E(l)} < g^{E(s)}$ so that g^s presents a flatter curve than does g^l and there exists a central composition region in which $g^l < g^s$. Hence, there are two common tangent lines, P_1Q_1 and P_2Q_2. Such a situation gives rise to a phase diagram with a minimum in the two-phase region as observed in the Au–Cu system shown in fig. 5 (HULTGREN *et al.* [1963]). At a composition and temperature corresponding to the minimum point, liquid and solid of the same composition exist in equilibrium.

A two-phase region with a minimum point as in fig. 5 may be thought of as a two-phase "lens" which has been "pushed down" by virtue of the fact that the liquid is relatively more stable than the solid. Thermodynamically, this relative stability is expressed as $g^{E(l)} < g^{E(s)}$.

Conversely, if $g^{E(l)} > g^{E(s)}$ to a sufficient extent, then a two-phase region with a maximum will result. In alloy systems, such maxima are nearly always associated with the existence of an intermetallic phase, as will be discussed in § 2.8.

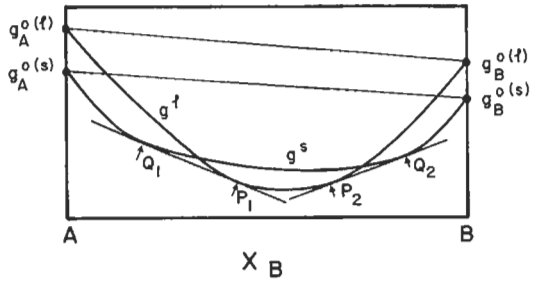

Fig. 4. Isothermal Gibbs-energy-composition curves for solid and liquid phases in a system A–B in which $g^{E(l)} < g^{E(s)}$. A phase diagram of the type in fig. 5 results.

References: p. 531.

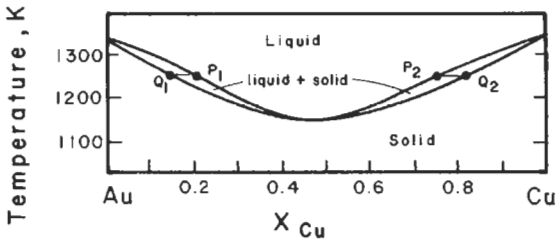

Fig. 5. Phase diagram of the Au–Cu system (after HULTGREN *et al.* [1963]).

2.3. Miscibility gaps

If $g^E > 0$ for a solution, then the solution is thermodynamically less stable than an ideal solution. In an alloy system this can result from a large difference in atomic diameter of the components, which will lead to a (positive) lattice strain energy, or from differences in valence, or from other factors.

In the Au–Ni system, g^E is positive in the solid phase. In the top panel of fig. 6 is plotted $g^{E(s)}$ at 1200 K (HULTGREN *et al.* [1963]) as well as the ideal Gibbs energy of mixing, Δg^{ideal}, also at 1200 K. The sum of these two terms is the Gibbs energy of mixing $\Delta g^s = \Delta g^{ideal} + g^{E(s)}$, which is plotted at 1200 K as well as at other temperatures in the central panel of fig. 6. Now,

$$\Delta g^{ideal} = RT\left(X_{Au} \ln X_{Au} + X_{Ni} \ln X_{Ni}\right)$$

is always negative and varies directly with T, whereas g^E varies less rapidly with temperature. As a result, the sum, $\Delta g^s = \Delta g^{ideal} + g^E$, becomes less negative as T decreases. However, the limiting slopes to the Δg^{ideal} curve at $X_{Au} = 1$ and $X_{Ni} = 1$ are both infinite

$$\left(\lim_{X_{Au}\to 1} d\left(\Delta g^{ideal}\right)/dX_{Au} = \lim_{X_{Ni}\to 1} d\left(\Delta g^{ideal}\right)/dX_{Ni} = \infty\right),$$

whereas the limiting slopes of g^E are always finite (Henry's Law). Hence, Δg^s will always be negative as $X_{Au} \to 1$ and $X_{Ni} \to 1$ no matter how low the temperature. As a result, below a certain temperature the curves of Δg^s will exhibit two negative "humps". Common tangent lines P_1Q_1, P_2Q_2, P_3Q_3 to the two humps define the ends of tie-lines of a two-phase solid–solid *miscibility gap* in the Au–Ni phase diagram which is shown in the lower panel in fig. 6 (HULTGREN *et al.* [1963]). The peak of the gap occurs at the *critical* or *consolute* temperature and composition, T_c and X_c.

When $g^{E(s)}$ is positive for the solid phase in a system it is usually also the case that $g^{E(l)} < g^{E(s)}$, since the unfavourable factors (such as a difference in atomic dimensions) which are causing $g^{E(s)}$ to be positive will have less of an influence upon $g^{E(l)}$ in the liquid phase owing to the greater flexibility of the liquid structure to accommodate different atomic sizes, valencies, etc. Hence, a solid–solid miscibility gap is often associated with a minimum in the two-phase (solid + liquid) region as in the Au–Ni system.

Below the critical temperature the curve of Δg^s exhibits two inflection points

indicated by the letter "s" in fig. 6. These are known as the *spinodal points*. On the phase diagram their locus traces out the *spinodal curve* as illustrated in fig. 6. The spinodal

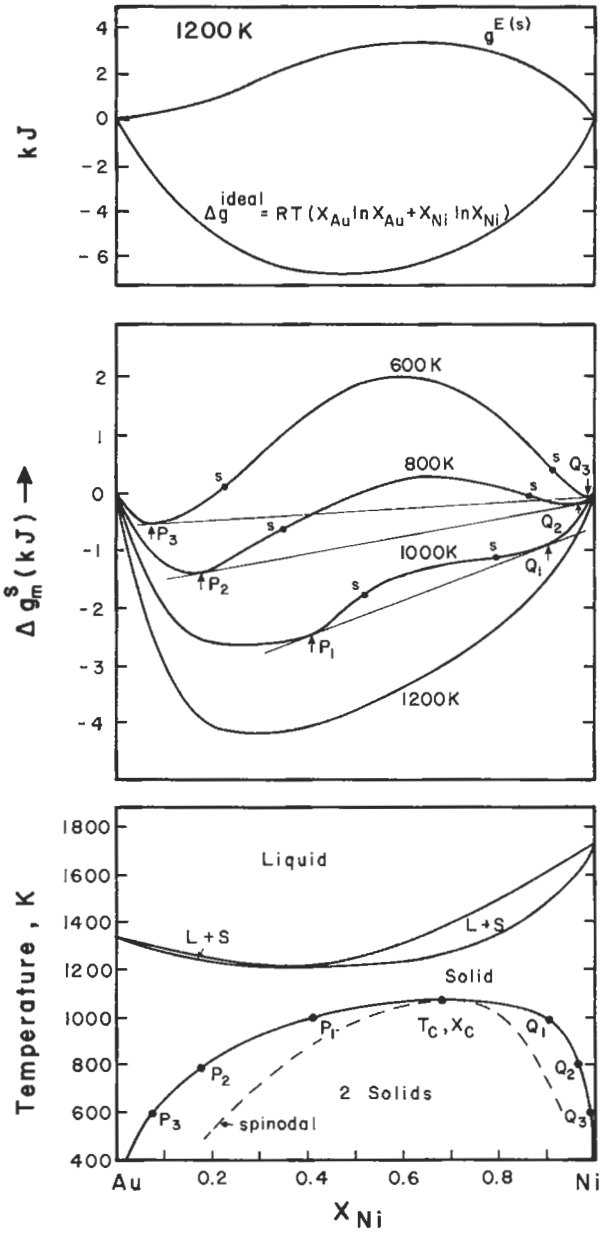

Fig. 6. Phase diagram and Gibbs energy curves of solid solutions for the Au–Ni system (after HULTGREN *et al.* [1963]). Letters "s" indicate spinodal points.

References: p. 531.

curve is not part of the equilibrium phase diagram, but it is important in the kinetics of phase separation as discussed in ch. § 15.

2.4. Simple eutectic systems

The more positive g^E in a system is, the higher is T_c and the wider is the miscibility gap at any temperature. Suppose that $g^{E(s)}$ is sufficiently positive that T_c is higher than the minimum in the (solid + liquid) region. The result will be a phase diagram such as that of the Ag–Cu system shown in fig. 7 (HULTGREN *et al.* [1963]).

In the upper panel of fig. 7 are shown the Gibbs energy curves at 1100 K. The two common tangents define two two-phase regions. As the temperature is decreased below 1100 K, the g^s curve descends relative to g^l, and the two points of tangency, P_1 and P_2, approach each other until, at $T = 1052$ K, P_1 and P_2 become coincident at the composition E. That is, at $T = 1052$ K there is just one common tangent line contacting the two portions of the g^s curve at compositions A and B and contacting the g^l curve at E. This temperature is known as the *eutectic temperature*, T_E, and the composition E is the *eutectic composition*. For temperatures below T_E, g^l lies completely above the common

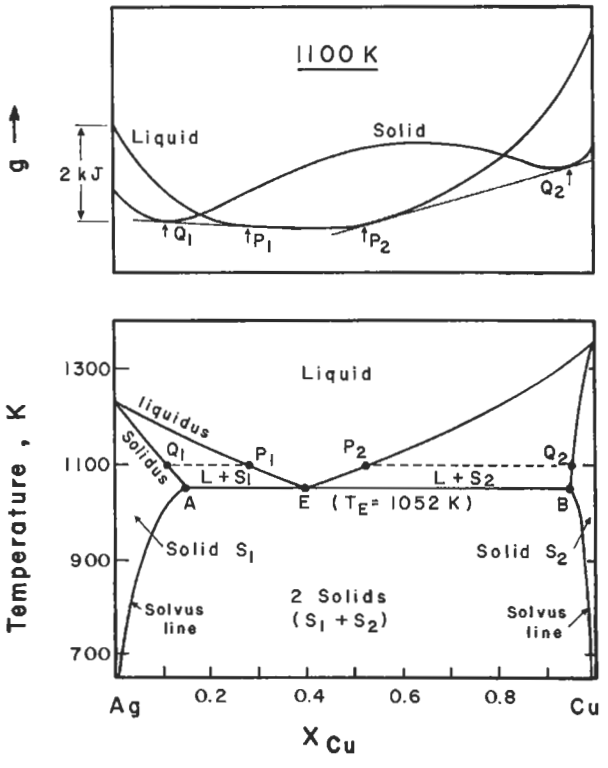

Fig. 7. Phase diagram and Gibbs energy curves at 1100 K of the Ag–Cu system (after HULTGREN *et al.* [1963]). Solid Ag and Cu are both fcc.

tangent to the two portions of the g^s curve and so, for $T < T_E$ a solid–solid miscibility gap is observed. The phase boundaries of this two-phase region are called the *solvus* lines. The word eutectic is from the Greek for "to melt well" since an alloy has the lowest melting point at the eutectic composition E.

This description of the thermodynamic origin of simple eutectic phase diagrams is strictly correct only if the pure solid components A and B have the same crystal structure (see § 2.6).

Suppose a Ag–Cu alloy of composition $X_{Cu} = 0.28$ (composition P_1) is cooled from the liquid state very slowly under equilibrium conditions. At 1100 K the first solid appears with composition Q_1. As T decreases further, solidification continues with the liquid composition following the liquidus curve from P_1 to E and the composition of the solid phase following the solidus curve from Q_1 to A. The relative proportions of the two phases at any T are given by the lever rule. At a temperature $T = (T_E + \delta)$ just above T_E, two phases are observed: a solid of composition A and a liquid of composition E. At a temperature $T = (T_E - \delta)$ just below T_E, two solids with compositions A and B are observed. Therefore, at T_E, during cooling, the following *binary eutectic reaction* occurs:

$$\text{liquid} \rightarrow \text{solid}_1 + \text{solid}_2. \tag{3}$$

Under equilibrium conditions the temperature will remain constant at $T = T_E$ until all the liquid has solidified, and during the reaction the compositions of the three phases will remain fixed at A, B and E. For this reason the eutectic reaction is called an *invariant* reaction.

The morphologies of two-phase grains resulting from the co-precipitation of two solids during eutectic reactions are discussed in detail in ch. 8.

2.5. Binary phase diagrams with no intermediate phases

2.5.1. Thermodynamic origin illustrated by simple regular solution theory

Many years ago VAN LAAR [1908] showed that the thermodynamic origin of a great many of the observed features of binary phase diagrams can be illustrated at least qualitatively by simple regular solution theory. As discussed in ch. 5, § 6.2, a *regular* solution is one in which:

$$g^E = \Omega X_A X_B, \tag{4}$$

where Ω is a parameter independent of temperature and composition.

In fig. 8 are shown several phase diagrams calculated for a hypothetical system A–B containing a solid and a liquid phase with melting points of $T^0_{f(A)} = 800$ K and $T^0_{f(B)} = 1200$ K and with entropies of fusion of both A and B set to 10 J/mol K, which is a typical value for metals. The solid and liquid phases are both regular with $g^{E(s)} = \Omega^s X_A X_B$ and $g^{E(l)} = \Omega^l X_A X_B$. The parameters Ω^s and Ω^l have been varied systematically to generate the various panels of fig. 8.

In panel (n) both phases are ideal. Panels (l–r) exhibit minima or maxima depending upon the sign and magnitude of $(g^{E(l)} - g^{E(s)})$, as has been discussed in § 2.2. In panel (h) the liquid is ideal but positive deviations in the solid give rise to a solid–solid miscibility gap as

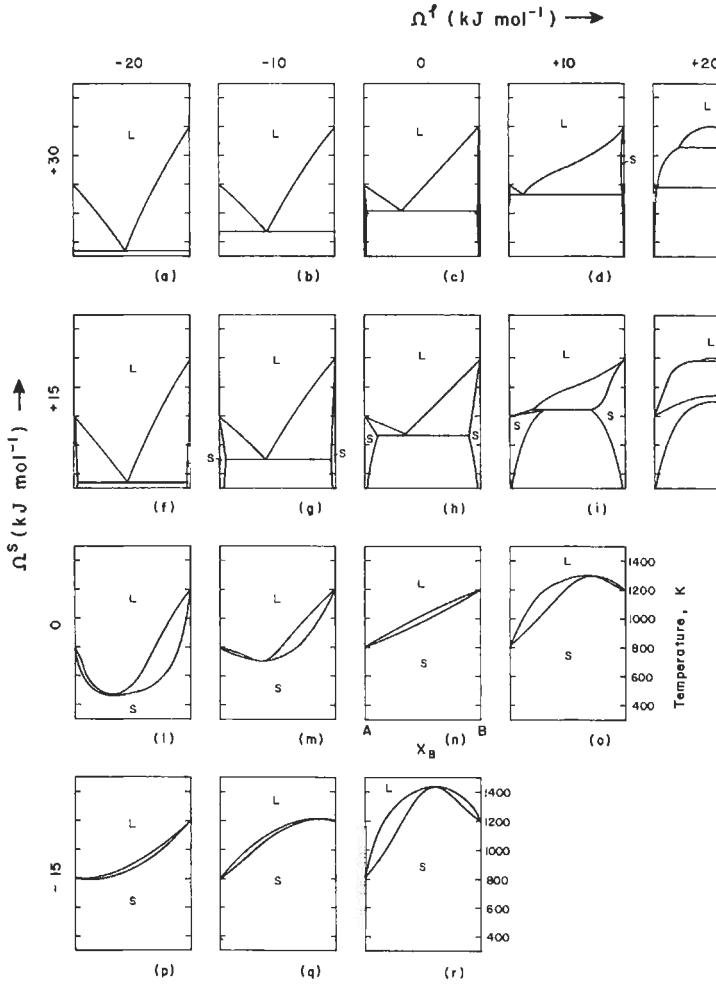

Fig. 8. Topological changes in the phase diagram for a system A–B with regular solid and liquid phases, brought about by systematic changes in the regular solution parameters Ω^s and Ω^l. Melting points of pure A and B are 800 K and 1200 K. Entropies of fusion of both A and B are 10.0 J/mol K. (PELTON and THOMPSON [1975].)

discussed above in § 2.4. On passing from panel (h) to panel (c), an increase in $g^{E(s)}$ results in a widening of the miscibility gap so that the solubilities of A in solid B and of B in solid A decrease. Panels (a–c) illustrate that negative deviations in the liquid cause a relative stabilization of the liquid with resultant lowering of the eutectic temperature.

Eutectic phase diagrams are often drawn with the maximum solid solubility occurring at the eutectic temperature (as in fig. 7). However fig. 8d, in which the maximum solubility of A in the B-rich solid solution occurs at approximately $T = 950$ K, illustrates that this need not be the case even for simple regular solutions.

2.5.2. Liquid–liquid immiscibility - monotectics

In fig. 8e, positive deviations in the liquid have given rise to a *liquid–liquid miscibility gap*. An example of a real system with such a phase diagram is the Cu–Pb system shown in fig. 9 (HULTGREN *et al.* [1963]). If a Cu–Pb alloy with $X_{Pb} = 0.10$ is cooled slowly from the liquid state, solid Cu begins to appear at 1260 K. Upon further cooling the liquid composition follows the liquidus curve to point A at $T = 1227$ K. The following invariant *monotectic reaction* then occurs:

$$\text{liquid}_A \rightarrow \text{liquid}_B + \text{Cu}_{(\text{solid})}, \tag{5}$$

where liquid_A and liquid_B are liquids with compositions at points A and B. The temperature remains constant at the monotectic temperature and the compositions of all phases remain fixed until liquid_A is completely consumed. Cooling then continues with precipitation of copper with the liquid composition following the liquidus line from B to the eutectic E.

Returning to fig. 8, we see that in panel (d) the positive deviations in the liquid are not large enough to produce immiscibility but they do result in a flattening of the liquidus which is often described as a "tendency to immiscibility". An example of such a flattened (or "S-shaped") liquidus resulting from a positive $g^{E(l)}$ is shown later for the Cd–Pb system in fig. 12.

2.5.3. Peritectics

The invariant which appears in fig. 8i is known as a *peritectic*. The Au–Fe system shown in fig. 10 (HULTGREN *et al.* [1963]) exhibits a peritectic PQR at 1441 K as well as another at about 1710 K. The Gibbs energy curves, g^l and g^{fcc}, of the liquid and solid face-centred cubic phases are shown schematically at the peritectic temperature of $T_p = 1441$ K in the upper panel of fig. 10. One common tangent line PQR to g^l and to the two portions of g^{fcc} can be drawn.

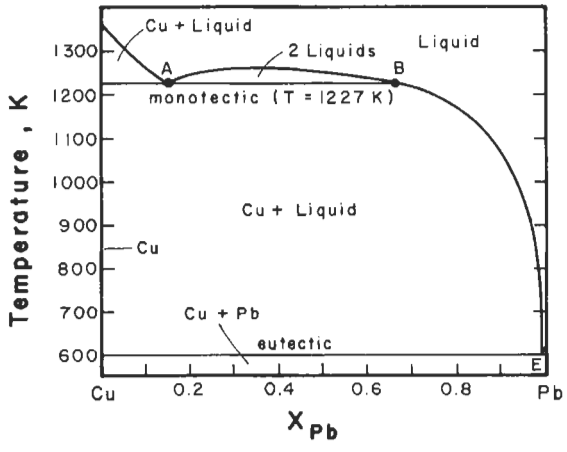

Fig. 9. The Cu–Pb phase diagram (after HULTGREN *et al.* [1963]).

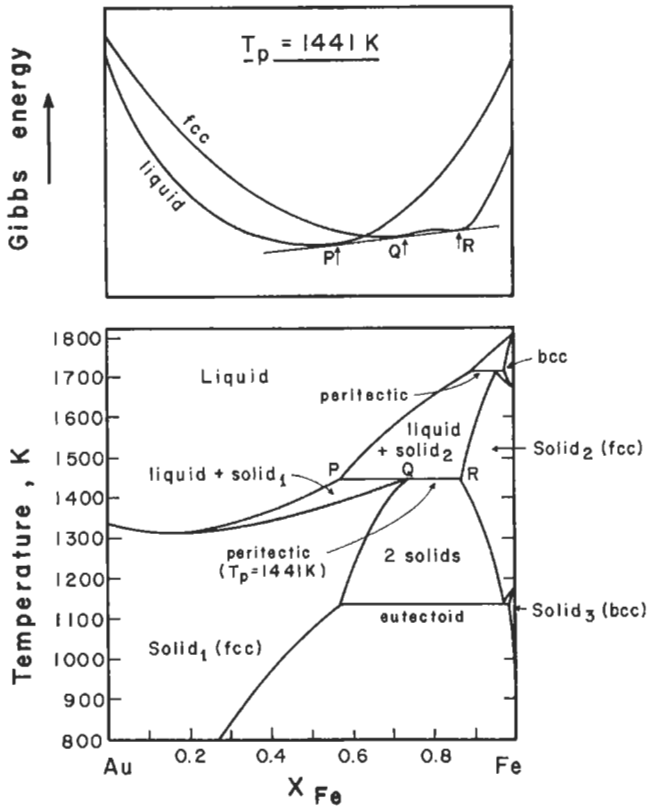

Fig. 10. Phase diagram and Gibbs energy curves at the peritectic temperature of 1441 K for the Au–Fe system (after HULTGREN *et al.* [1963]).

Suppose that a Au–Fe alloy of composition $X_{Fe} = 0.65$ is cooled very slowly from the liquid state. At a temperature $(T_p + \delta)$ just above 1441 K, a liquid phase of composition P and an fcc phase of composition R are observed at equilibrium. At a temperature $(T_p - \delta)$ just below 1441 K, the two phases at equilibrium are liquid and solid with compositions P and Q respectively. The following invariant *binary peritectic reaction* thus occurs upon cooling:

$$\text{liquid} + \text{solid}_2 \rightarrow \text{solid}_1. \tag{6}$$

This reaction occurs isothermally with all three phases at fixed compositions (at points P, Q and R). In the case of an alloy with overall composition between P and Q, the reaction occurs isothermally until all solid_2 is consumed. In the case of an alloy with overall composition between Q and R, it is the liquid which will first be completely consumed.

A peritectic reaction between a liquid and solid_2 occurs on the surface of the particles

of solid$_2$ which can rapidly become coated with solid$_1$. By preventing contact between liquid and solid$_2$, this coating may greatly retard further reaction to such an extent that equilibrium conditions can only be achieved by extremely slow cooling.

2.5.4. Syntectics

The invariant in fig. 8k in which a solid decomposes upon heating into two liquids is known as a *syntectic*. It is rarely observed in alloy systems. Examples are found in the K–Pb and K–Zn systems (HANSEN [1958]). A phase diagram similar to fig. 8j, although without the tiny miscibility gap, is exhibited by the Au–Pt system (HANSEN [1958]).

2.6. Limited mutual solid solubility

In § 2.4 the region of two solids in the Ag–Cu phase diagram of fig. 7 was described as a miscibility gap in the solid phase. That is, only one g^s curve was drawn. If, somehow, the appearance of the liquid phase could be suppressed, then the two solvus lines in fig. 7, when projected upwards, would meet at a critical point (as in the Au–Ni system in fig. 6) above which one continuous solid solution would exist at all compositions.

Such a description is justifiable only if the pure solid components have the same crystal structure. This is the case for Ag–Cu since solid Ag and Cu are both fcc. The same assumption was made in our treatment of the peritectic Au–Fe system (fig. 10) in which the region of two solids was treated as a miscibility gap. Again in this case this description is permissible since Au and Fe are both fcc in this temperature range.

However, consider the simple eutectic system A–B in fig. 11 in which pure solid A and B are hcp (hexagonal close-packed) and fcc respectively. In this case, if the formation of the liquid phase could be suppressed the two solvus lines could not project upward to meet at a critical point, since this would imply that above this critical temperature a continuous series of solid solutions varying smoothly from hcp to fcc could exist. Such a situation is prohibited by symmetry conditions. That is, one continuous curve for g^s cannot be drawn. Each solid phase must have its own separate Gibbs energy curve, as shown schematically in the upper panels of fig. 11. In this figure, $g_A^{0(fcc)}$ is the *standard molar Gibbs energy of pure fcc A* and $g_B^{0(hcp)}$ is the standard molar Gibbs energy of pure hcp B. Such quantities may be defined in a number of different and non-equivalent ways as will be discussed below.

A real system with a phase diagram similar to fig. 11 is the Cd–Pb system shown in fig. 12 (ASHTAKALA *et al.* [1981]). Gibbs energy curves at a temperature below the eutectic are shown schematically in the upper panel. Let us derive an expression for g^{fcc} under the assumption that the Pb-rich fcc solid solution is a *Henrian solution*. As discussed in ch. 5, § 6.2, when a solution is sufficiently dilute in one component, Henrian behaviour may be assumed. That is, the activity of the solvent is ideal ($a_{solvent} = X_{solvent}$; $\gamma^0_{solvent} = 1$), while for the solute, $a_{solute} = \gamma^0_{solute} X_{solute}$, where the *Henrian activity coefficient*, γ_{solute}, is independent of composition. At $T_E = 247.8°C$ in fig. 12, Cd in the Pb-rich fcc solution at $X_{Pb} = 0.940$ exists in equilibrium with virtually pure solid hcp Cd. Thus, in the fcc solution, $a_{Cd} \approx 1.0$ with respect to pure solid hcp Cd as standard state. Hence, $\gamma^0_{Cd} = a_{Cd}/X_{Cd} = 1.0/0.060 = 16.67$ at 247.8°C. We can now express g^{fcc} as:

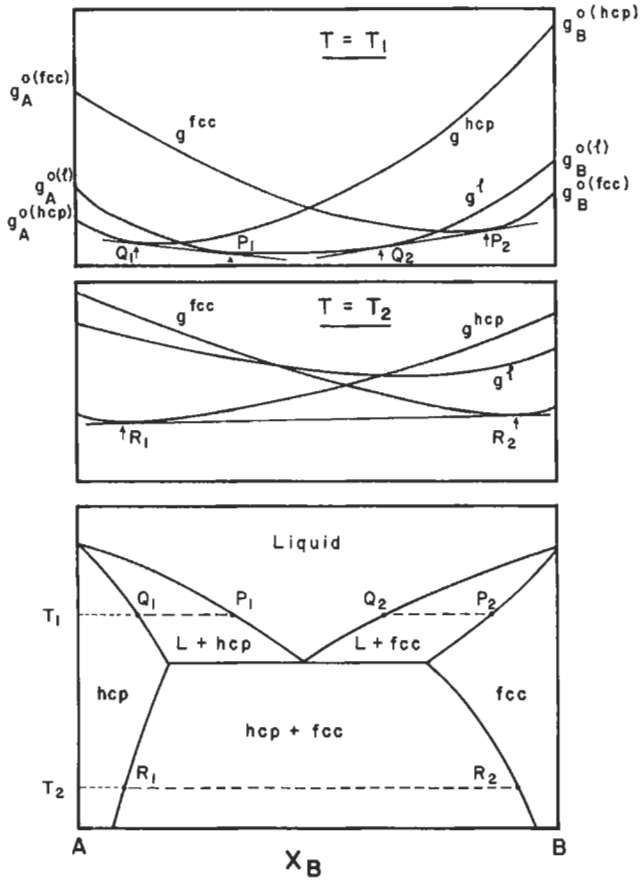

Fig. 11. Phase diagram and Gibbs energy curves at two temperatures for a simple eutectic system A–B in which pure solid A and B have different crystal structures.

$$\begin{aligned} g^{\text{fcc}} &= \left(X_{\text{Cd}} g_{\text{Cd}}^{0(\text{hcp})} + X_{\text{Pb}} g_{\text{Pb}}^{0(\text{fcc})}\right) + RT\left(X_{\text{Cd}} \ln a_{\text{Cd}} + X_{\text{Pb}} \ln a_{\text{Pb}}\right) \\ &= \left(X_{\text{Cd}} g_{\text{Cd}}^{0(\text{hcp})} + X_{\text{Pb}} g_{\text{Pb}}^{0(\text{fcc})}\right) + RT\left(X_{\text{Cd}} \ln(\gamma_{\text{Cd}}^{0} X_{\text{Cd}}) + X_{\text{Pb}} \ln X_{\text{Pb}}\right) \end{aligned} \tag{7}$$

However, since γ_{Cd}^{0} is independent of composition we can combine terms as follows:

$$\begin{aligned} g^{\text{fcc}} &= \left[X_{\text{Cd}}\left(g_{\text{Cd}}^{0(\text{hcp})} + RT \ln \gamma_{\text{Cd}}^{0}\right) + X_{\text{Pb}} g_{\text{Pb}}^{0(\text{fcc})}\right] \\ &\quad + RT\left(X_{\text{Cd}} \ln X_{\text{Cd}} + X_{\text{Pb}} \ln X_{\text{Pb}}\right). \end{aligned} \tag{8}$$

Let us now define:

$$g_{\text{Cd}}^{0(\text{fcc})} = \left(g_{\text{Cd}}^{0(\text{hcp})} + RT \ln \gamma_{\text{Cd}}^{0}\right).$$

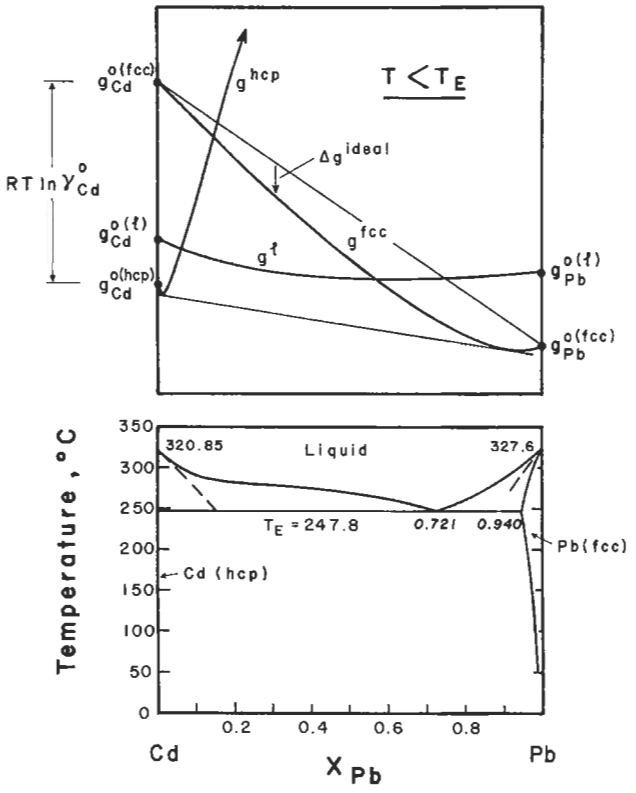

Fig. 12. Phase diagram of the Cd–Pb system (after ASHTAKALA *et al.* [1981]) and Gibbs energy curves (schematic) at a temperature below the eutectic. Dashed lines indicate limiting liquidus slopes calculated for zero solid solubility.

From eq. (8) it can be seen that relative to $g_{Cd}^{0(fcc)}$ defined in this way and to $g_{Pb}^{0(fcc)}$ the fcc solution is ideal. This is illustrated in fig. 12.

At 247.8°C in Cd–Pb, $(g_{Cd}^{0(fcc)} - g_{Cd}^{0(hcp)}) = RT \ln \gamma_{Cd}^{0} = R(247.8 + 273.15) \ln 16.67 = 12.19$ kJ/mol. As a first approximation we could take this value to be independent of T, or as a second approximation we could evaluate γ_{Cd}^{0} at other temperatures along the solidus and express $(g_{Cd}^{0(fcc)} - g_{Cd}^{0(hcp)})$ as, say, a linear function of T.

Although the above treatment has the advantage of numerical simplicity, it suffers from the difficulty that the numerical value of $(g_{Cd}^{0(fcc)} - g_{Cd}^{0(hcp)})$ is solvent–dependent and will be different for, say, solutions of Cd in fcc Cu and Cd in fcc Pb. For purposes of predicting binary phase diagrams from first principles or for estimating ternary phase diagrams from binary phase diagrams (§ 5.5) it would be desirable if $g_{Cd}^{0(fcc)}$ could be defined to be system-independent so as to be truly the "standard molar Gibbs energy of metastable fcc Cd". A great deal of effort has been expended by the international CALPHAD group under the impetus of Kaufman (KAUFMAN and BERNSTEIN [1970]) and

co-workers to compile tables of *lattice stabilities* for metals in the fcc, hcp, bcc, and liquid states (that is, to obtain a set of relative values of $g^{0(fcc)}$, $g^{0(hcp)}$, $g^{0(bcc)}$ and $g^{0(l)}$ for every metal). In some cases, these can be calculated by extrapolating thermodynamic data from regions of T and P where the phases are stable. In other cases, lattice stabilities can be estimated partly from theoretical calculations and partly from the analysis of a large number of binary phase diagrams followed by a judicious choice of the "best" values which most closely fit the greatest number of systems. Tabulations of lattice stabilities are now available for many metals (DINSDALE [1991]).

2.7. Calculation of limiting slopes of phase boundaries

In fig. 12 we see that the solubility of Pb in solid Cd is very small. The actual solubility at T_E is about 0.14 mol% (HANSEN [1958]). In thermodynamic terms this means that g^{hcp} increases very rapidly as Pb is added to solid Cd (see fig. 12), or that the Henrian activity coefficient γ^0_{Pb} is very large. The fact that the solubility of Cd in solid Pb is much greater than that of Pb in solid Cd can be understood in terms of the Hume–Rothery rule (ch. 4) that solubilities are greater when the solute atoms are smaller than the solvent atoms, since the lattice strain energy will be less and hence g will rise less rapidly upon addition of solute.

As discussed later in § 7, it is usually more difficult experimentally to determine a solidus than it is to measure liquidus temperatures. However, if the liquidus has been measured in the limit as $X_{solvent} \rightarrow 1$, then the limiting slope of the solidus can be calculated. Let component B be the solvent in a system A–B. The partial Gibbs energies of B along the liquidus and solidus are equal ($g^l_B - g^s_B = 0$). Hence:

$$\left(g^l_B - g^{0(l)}_B\right) - \left(g^s_B - g^{0(s)}_B\right) = -\left(g^{(0)l}_B - g^{0(s)}_B\right). \tag{9}$$

But: $(g^l_B - g^{0(l)}_B) \equiv RT \ln a^l_B$ and $(g^s_B - g^{0(s)}_B) \equiv RT \ln a^s_B$, where a^s_B and a^s_B are activities of B on the liquidus and solidus with respect to the pure liquid and pure solid standard states respectively. Hence, eq. (9) may be written as:

$$RT \ln a^l_B - RT \ln a^s_B = -\Delta g^0_{f(B)}. \tag{10}$$

In the limit $X_B \rightarrow 1$, Raoult's Law holds for both phases. That is, $a^l_B \rightarrow X^l_B$ and $a^s_B \rightarrow X^s_B$. Hence, in the limit, eq. (10) may be written as:

$$RT \ln X^l_B / X^s_B = -\Delta g^0_{f(B)}. \tag{11}$$

Furthermore, in the limit, $T \rightarrow T^0_{f(B)}$ and from eq. (1) $\Delta g^0_{f(B)} \rightarrow \Delta h^0_{f(B)}(1 - T/T^0_{f(B)})$. Finally, $\lim_{X_B \rightarrow 1}(\ln X_B) = (X_B - 1)$. Substituting these limiting values into eq. (11) we obtain:

$$\lim_{X_B \rightarrow 1}\left(dX^l_B/dT - dX^s_B/dT\right) = \Delta h^0_{f(B)}/R\left(T^0_{f(B)}\right)^2. \tag{12}$$

If the limiting slope of the liquidus, $\lim_{X_B \rightarrow 1}(dX^l_B/dT)$, is known, then the limiting slope of the solidus can be calculated via eq. (12) if the enthalpy of fusion is known.

For the Cd–Pb system, limiting liquidus slopes were calculated for both components

from eq. (12) under the assumption that there is no solid solubility (that is, that $dX_B^s/dT = 0$). These are shown as the dashed lines on fig. 12. In Cd-rich solutions, agreement with the measured limiting liquidus slope is very good, but in Pb-rich solutions the poor agreement indicates the existence of appreciable solid solubility as has been confirmed by direct measurement.

2.8. Intermediate phases

The phase diagram of the Ag–Mg system (HULTGREN *et al.* [1963]) is shown in fig. 13. An *intermetallic phase*, β', is seen centered approximately about the composition

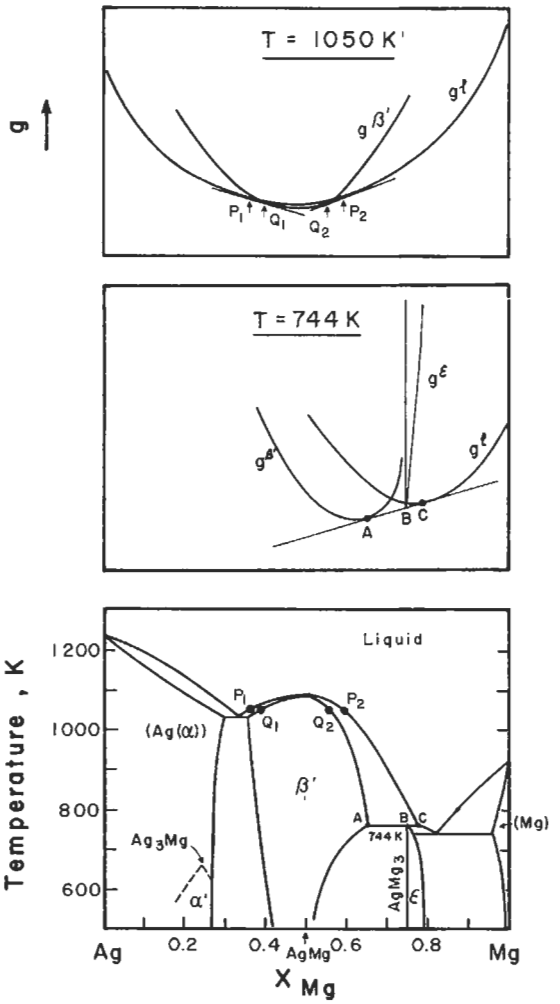

Fig. 13. Ag–Mg phase diagram (after HULTGREN *et al.* [1963]) and Gibbs energy curves (schematic) at 744 K and 1050 K.

References: p. 531.

$X_{Mg} = 0.5$. The Gibbs energy curve for such an intermetallic phase has the form shown schematically in the upper panel of fig. 13. $g^{\beta'}$ rises quite rapidly on either side of its minimum which occurs near $X_{Mg} = 0.5$. As a result, the β' phase appears on the phase diagram only over a limited composition range. This form of the curve $g^{\beta'}$ results from the fact that when $X_{Ag} \approx X_{Mg}$ a particularly stable crystal structure exists in which Ag and Mg atoms preferentially occupy different sites. The two common tangents P_1Q_1 and P_2Q_2 give rise to a maximum in the two-phase (β' + liquid) region in the phase diagram. (Although the maximum is observed very near $X_{Mg} = 0.5$, there is no thermodynamic reason for the maximum to occur exactly at this composition.)

The Na–Bi phase diagram is shown in fig. 14 (HANSEN [1958]). Gibbs energy curves at 700°C are shown schematically in the upper panel. $g(Na_{3/4}Bi_{1/4})$ rises extremely rapidly on either side of its minimum which occurs at $X_{Na} = 3/4$, $X_{Bi} = 1/4$. (We write $g(Na_{3/4}Bi_{1/4})$ rather than $g(Na_3Bi)$ in order to normalize to a basis of one mole of metal atoms.) As a result, the points of tangency Q_1 and Q_2 of the common tangents P_1Q_1 and P_2Q_2 are nearly (but not exactly) coincident. Hence, the composition range over which single-phase Na_3Bi exists (sometimes called the *range of stoichiometry* or *homogeneity*

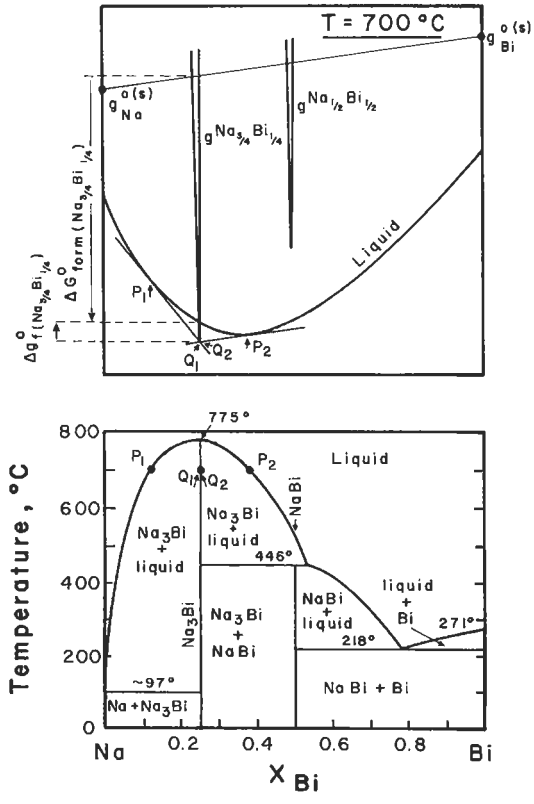

Fig. 14. Na–Bi phase diagram (after HANSEN [1958]) and schematic Gibbs energy curves at 700°C.

range of Na_3Bi) is very narrow (but never zero). The two regions labelled (Na_3Bi + liquid) in fig. 14 are the two sides of a two-phase region which passes through a maximum just like the (β' + liquid) regions in fig. 13. Because the Na_3Bi single-phase region is so narrow we refer to Na_3Bi as an *intermetallic compound*. In the case of Na_3Bi, any slight deviation from the stoichiometric composition causes a very large increase in Gibbs energy. Owing to the large difference in electronegativities of Na and Bi, Na_3Bi could be considered to be a semi-ionic compound. Deviations from stoichiometry would require the substitution of Na on Bi sites or vice versa which would be energetically very unfavourable.

If stoichiometric Na_3Bi is heated, it will melt isothermally at 775°C to form a liquid of the same composition. That is, the melting behaviour of Na_3Bi is similar to that of a pure element. Such intermetallic compounds are called *congruently melting* or simply *congruent compounds*. The β' phase in fig. 13 might also be called a congruent intermetallic compound AgMg (or $AgMg_{1\pm\delta}$). It is debatable, however, whether a phase with such a wide range of composition should really be called a "compound".

It should be noted with regard to the congruent melting of Na_3Bi in fig. 14 that the limiting slopes dT/dX of the two liquidus curves at the congruent melting point (775°C) are both zero, since we are really dealing with a maximum in a two-phase region and not with the melting of an element.

Another intermetallic phase, the ε phase, is also observed in the Ag–Mg system, fig 13. This phase has a narrow range of stoichiometry around the composition $AgMg_3$. This phase is associated with a *peritectic* invariant ABC at 744 K. The Gibbs energy curves are shown schematically at the peritectic temperature in the central panel of fig. 13. One common tangent line can be drawn to g^l, $g^{\beta'}$, and g^{ε}.

Suppose that a liquid alloy of composition $X_{Mg} = 0.7$ is cooled very slowly from the liquid state. At a temperature just above 744 K a liquid phase of composition C and a β' phase of composition A are observed at equilibrium. At a temperature just below 744 K, the two phases at equilibrium are β' of composition A and ε of composition B. The following *invariant peritectic reaction* thus occurs upon cooling (cf. § 2.5.3):

$$\text{liquid} + \beta'(\text{solid}) \rightarrow \varepsilon(\text{solid}). \tag{13}$$

This reaction occurs isothermally at 744 K with all three phases at fixed compositions (at points A, B and C). For an alloy with overall composition between points A and B the reaction proceeds until all the liquid has been consumed. In the case of an alloy with overall composition between B and C, the β' phase will be the first to be completely consumed.

The $AgMg_3(\varepsilon)$ compound is said to *melt incongruently*. If solid $AgMg_3$ is heated, it will melt isothermally at 744 K, by the reverse of the above peritectic reaction (14), to form a liquid of composition C and another solid phase, β', of composition A.

Another example of an *incongruent compound* is the compound NaBi in fig. 14. This compound has a very narrow range of stoichiometry. When heated, it melts incongruently (or peritectically) at the peritectic temperature of 446°C to form another solid, Na_3Bi, and a liquid of composition $X_{Bi} \approx 0.53$.

An incongruent compound is always associated with a peritectic. (The word peritectic comes from the Greek for (loosely) "to melt in an indirect way".) However, the converse

is not necessarily true. A peritectic is not always associated with an intermediate phase. See, for example, fig. 10.

For purposes of phase diagram computations involving very stoichiometric compounds such as Na_3Bi, we may, to a good approximation, consider the Gibbs energy curve, $g(Na_{3/4}Bi_{1/4})$, to have zero width. Then all we need is the numerical value of $g(Na_{3/4}Bi_{1/4})$ at the minimum. This value is usually expressed in terms of the *Gibbs energy of fusion of the compound*, $\Delta g^0_{f(Na_{3/4}Bi_{1/4})}$, or in terms of the "*Gibbs energy of formation*", $\Delta g^0_{form(Na_{3/4}Bi_{1/4})}$, of the compound from solid Na and Bi according to the reaction $\frac{3}{4}Na_{(s)} + \frac{1}{4}Bi_{(s)} = Na_{3/4}Bi_{1/4(s)}$. Both these quantities are interpreted graphically in fig. 14.

2.9. Topology of binary phase diagrams

In ch. 5, § 8.2 the *Gibbs phase rule* was derived.:

$$F = C - P + 2, \tag{14}$$

where C is the number of components, P the number of phases in equilibrium, and F the number of degrees of freedom or variance. That is, F is the number of parameters which can and must be specified in order to completely specify the state of the system. In the present context, the thermodynamic parameters are temperature, total pressure, and the compositions of the phases at equilibrium. Since binary temperature–composition phase diagrams are plotted at constant pressure, usually 1 bar, one degree of freedom is already used up. In a binary system, $C = 2$. Hence, for binary isobaric T–X diagrams the phase rule reduces to:

$$F = 3 - P. \tag{15}$$

Binary T–X diagrams contain single-phase areas and two-phase areas. In the single-phase areas, $F = 3 - 1 = 2$. That is, temperature and composition can be varied independently. These regions are thus called *bivariant*. In two-phase regions, $F = 3 - 2 = 1$. If, say, T is chosen, then the compositions of both phases are fixed by the ends of the tie-lines. Two-phase regions are thus termed *univariant*. Note that the overall composition can be varied within a two-phase region at constant T, but the overall composition is not a variable in the sense of the phase rule. Rather, it is the compositions of the individual phases at equilibrium that are the variables to be considered in counting the number of degrees of freedom.

When three phases are at equilibrium in a binary system at constant pressure, $F = 3 - 3 = 0$. Hence, the compositions of all three phases as well as T are fixed. There are two general types of three-phase *invariants* in binary phase diagrams. These are the *eutectic-type* and *peritectic-type* invariants as illustrated in fig. 15. Let the three phases concerned be called α, β and γ, with β as the central phase as shown in fig. 15. α, β and γ can be solid, liquid or gaseous phases. At the eutectic-type invariant, the following invariant reaction occurs isothermally as the system is cooled:

$$\beta \rightarrow \alpha + \gamma, \tag{16}$$

whereas, at the peritectic-type invariant the invariant reaction upon cooling is:

$$\alpha + \gamma \rightarrow \beta \tag{17}$$

Some examples of eutectic-type invariants are: (i) *eutectics* (fig. 7) in which $\alpha = \text{solid}_1$, $\beta = \text{liquid}$, $\gamma = \text{solid}_2$. The eutectic reaction is $l \rightarrow s_1 + s_2$; (ii) *monotectics* (fig. 9) in which $\alpha = \text{liquid}_1$, $\beta = \text{liquid}_2$, $\gamma = \text{solid}$. The monotectic reaction is $l_2 \rightarrow l_1 + s$; (iii) *eutectoids* (fig. 10) in which $\alpha = \text{solid}_1$, $\beta = \text{solid}_2$, $\gamma = \text{solid}_3$. The eutectoid reaction is $s_2 \rightarrow s_1 + s_3$; (iv) *catatectics* in which $\alpha = \text{liquid}$, $\beta = \text{solid}_1$, $\gamma = \text{solid}_2$. The catatectic reaction is $s_1 \rightarrow l + s_2$.

Some examples of peritectic type invariants are: (i) *peritectics* (fig. 10) in which $\alpha = \text{liquid}$, $\beta = \text{solid}_1$, $\gamma = \text{solid}_2$. The peritectic reaction is $l + s_2 \rightarrow s_1$; (ii) *syntectics* (fig. 8k) in which $\alpha = \text{liquid}_1$, $\beta = \text{solid}$, $\gamma = \text{liquid}_2$. The syntectic reaction is $l_1 + l_2 \rightarrow s$; (iii) *peritectoids* in which $\alpha = \text{solid}_1$, $\beta = \text{solid}_2$, $\gamma = \text{solid}_3$. The peritectoid reaction is $s_1 + s_3 \rightarrow s_2$.

An important rule of construction which applies to invariants in binary phase diagrams is illustrated in fig. 15. This *extension rule* states that at an invariant the extension of a boundary of a two-phase region must pass into the adjacent two-phase region and not into the single-phase region. Examples of both correct and incorrect constructions are given in fig. 15. To understand why the "incorrect extension" shown is not correct, consider that the $(\alpha + \gamma)$ phase boundary line indicates the composition of the γ-phase in equilibrium with the α-phase as determined by the common tangent to the

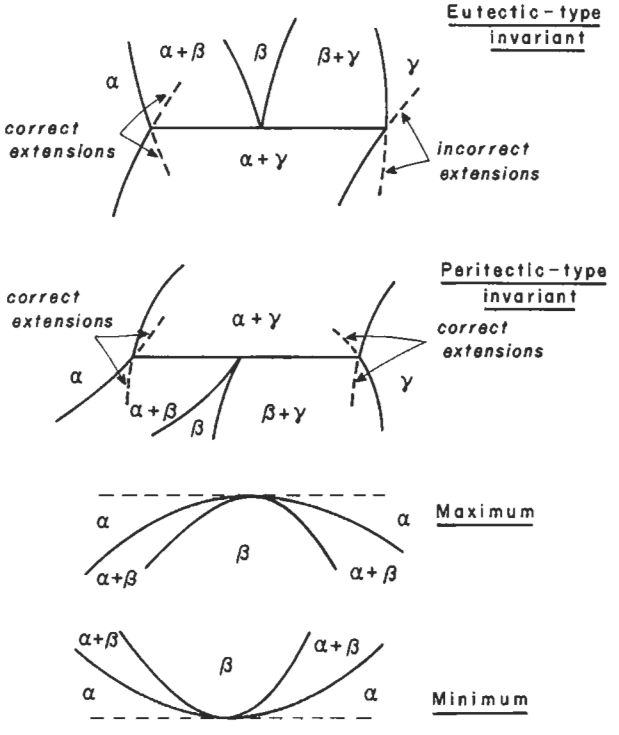

Fig. 15. Some topological units of construction of binary phase diagrams illustrating rules of construction.

References: p. 531.

Gibbs energy curves. Since there is no reason for the Gibbs energy curves or their derivatives to change discontinuously at the invariant temperature, the extension of the $(\alpha + \gamma)$ phase boundary also represents the composition of the γ-phase in equilibrium with the α-phase. Hence, for this line to extend into a region labelled as single-phase γ is incorrect.

Two-phase regions in binary phase diagrams can terminate: (i) on the pure component axes (at $X_A = 1$ or $X_B = 1$) at a transformation point of pure A or B; (ii) at a critical point of a miscibility gap; (iii) at an invariant. Two-phase regions can also exhibit maxima or minima. In this case, both phase boundaries must pass through their maximum or minimum at the same point as shown in fig. 15.

All the *topological units* of construction of binary phase diagrams have now been discussed. The phase diagram of a binary alloy system will usually exhibit several of these units. As an example, the Fe–Mo phase diagram (KUBASCHEWSKI [1982]) is shown in fig. 16. The invariants in this system are: peritectics at 1540, 1488, and 1450°C; eutectoids at 1235 and 1200°C; peritectoids at 1370 and 950°C. The two-phase (liquid $+\gamma$) region passes through a minimum at $X_{Mo} = 0.2$.

Between 910°C and 1390°C is a two-phase $(\alpha + \gamma)$ γ-*loop*. Pure Fe adopts the fcc γ structure between these two temperatures but exists as the bcc α phase at higher and lower temperatures. Mo however, is more soluble in the bcc than in the fcc structure. That is, $g_{Mo}^{0(bcc\text{-}Fe)} < g_{Mo}^{0(fcc\text{-}Fe)}$ as discussed in § 2.6. Therefore, small additions of Mo stabilize the bcc structure.

2.9.1. Order-disorder transformations

In fig. 13 for the Ag–Mg system, a transformation from an α' to an α phase is shown occurring at approximately 390 K at the composition Ag_3Mg. This is an *order–disorder*

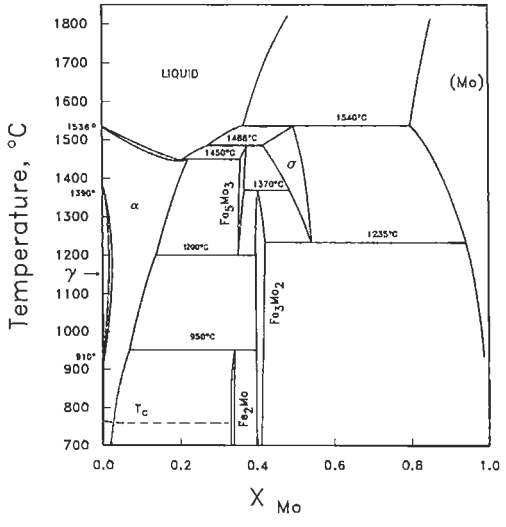

Fig. 16. Fe–Mo phase diagram (KUBASCHEWSKI [1982]).

transformation. Below the transformation temperature, *long-range ordering* (superlattice formation) is observed. An *order parameter* may be defined which decreases to zero at the transformation temperature. This type of phase transformation is not necessarily a first-order transformation like those considered so far in this chapter. Unlike transformations which involve atomic displacements over distances large compared with atomic dimensions, order–disorder transformations, at least at the stoichiometric composition (Ag_3Mg is this example), occur by atomic rearrangement over distances of the order of atomic dimensions. The slope of the curve of Gibbs energy versus T is not necessarily discontinuous at the transformation temperature. For a detailed discussion see ch. 4, § 4.1.1, INDEN [1982], and PITSCH and INDEN [1991].

A type of order–disorder transformation of importance in ferrous metallurgy is the magnetic transformation. Below its *Curie temperature* of 769°C, Fe is ferromagnetic. Above this temperature it is not. The transformation involves a change in ordering of the magnetic domains and is not first-order. Additions of alloying elements will change the temperature of transformation. Magnetic transformations are treated in ch. 29. See also MIODOWNIK [1982], INDEN [1982] and HILLERT and JARL [1978].

2.10. Application of thermodynamics to phase diagram analysis

In recent years, the development of solution models, numerical methods and computer software has permitted a quantitative application of thermodynamics to phase diagram analysis. Computer programs are available which permit phase diagrams to be generated from equations for the Gibbs energies of the phases. Other programs have been written to perform simultaneous critical evaluations of available phase diagram measurements and of available thermodynamic data (calorimetric data, measurements of activities, etc.) with a view to obtaining optimized equations for the Gibbs energies of each phase which best represent all the data. These equations are consistent with thermodynamic principles and with theories of solution behaviour.

The phase diagram can be calculated from these optimized thermodynamic equations, and so one set of self-consistent equations describes all the thermodynamic properties and the phase diagram. This technique of analysis greatly reduces the amount of experimental data needed to characterize a system fully. All data can be tested for internal consistency. The data can be interpolated and extrapolated more accurately, and metastable phase boundaries can be calculated. All the thermodynamic properties and the phase diagram can be represented and stored by means of a small set of coefficients.

Finally and most importantly, it is often possible to estimate the thermodynamic properties and phase diagrams of ternary and higher-order systems from the assessed parameters for their binary sub-systems as will be discussed in § 5. The analysis of binary systems is thus the first and most important step in the development of databases for multicomponent systems.

The computer coupling of thermodynamics and phase diagrams is a growing field of much current research interest. The international Calphad Journal, published by Pergamon Press, and an annual international meeting, the Calphad Conference, are now devoted to this subject.

References: p. 531.

2.10.1. Polynomial representation of excess properties

Empirical equations are required to express the excess thermodynamic properties of the solution phases as functions of composition and temperature. For many simple binary substitutional solutions, a good representation is obtained by expanding the molar excess enthalpy and entropy as polynomials in the mole fractions X_A and X_B of the components:

$$h^E = X_A X_B(h_0 + h_1(X_B - X_A) + h_2(X_B - X_A)^2 + h_3(X_B - X_A)^3 + \ldots) \tag{18}$$

$$s^E = X_A X_B(s_0 + s_1(X_B - X_A) + s_2(X_B - X_A)^2 + s_3(X_B - X_A)^3 + \ldots) \tag{19}$$

where the h_i and s_i are empirical coefficients. As many coefficients are used as are required to represent the data in a given system. For most systems it is a good approximation to assume that the coefficients h_i and s_i are independent of temperature.

If the series are truncated after the first term, then:

$$g^E = h^E - Ts^E = X_A X_B(h_0 - Ts_0) \tag{20}$$

This is the same as eq. (4) for a regular solution. Hence, the polynomial representation can be considered to be an extension of regular solution theory. When the expansions are written in terms of the composition variable $(X_B - X_A)$ as in eqs. (18) and (19) they are said to be in *Redlich–Kister* form. Other equivalent polynomial expansions such as orthogonal Legendre series have been discussed by PELTON and BALE [1986].

Differentiation of eqs. (18) and (19) yields the following expansions for the partial excess properties:

$$h_A^E = X_B^2 \sum_{i=0} h_i \left[(X_B - X_A)^i - 2iX_A(X_B - X_A)^{i-1} \right] \tag{21}$$

$$h_B^E = X_A^2 \sum_{i=0} h_i \left[(X_B - X_A)^i + 2iX_B(X_B - X_A)^{i-1} \right] \tag{22}$$

$$s_A^E = X_B^2 \sum_{i=0} s_i \left[(X_B - X_A)^i - 2iX_A(X_B - X_A)^{i-1} \right] \tag{23}$$

$$s_B^E = X_A^2 \sum_{i=0} s_i \left[(X_B - X_A)^i + 2iX_B(X_B - X_A)^{i-1} \right] \tag{24}$$

2.10.2. Least-squares optimization

Eqs. (18), (19) and (21) to (24) are linear in terms of the coefficients. Through the use of these equations, all integral and partial excess properties (g^E, h^E, s^E, g_i^E, h_i^E, s_i^E) can be expressed by linear equations in terms of the one set of coefficients $\{h_i, s_i\}$. It is thus possible to include all available experimental data for a binary phase in one simultaneous linear least-squares optimization as discussed by BALE and PELTON [1983],

LUKAS *et al.* [1977] and DÖRNER *et al.* [1980], and specialized software for such optimizations is available.

The technique of coupled thermodynamic/phase diagram analysis is best illustrated by an example. The phase diagram of the Cd–Na system with points measured by several authors is shown in fig. 17. From electromotive force measurements on alloy concentration cells, several authors have measured the activity coefficient of Na in liquid alloys. These data are shown in fig. 18 at 400°C. From the temperature dependence of $g^{E}_{Na} = RT \ln \gamma_{Na}$, the partial enthalpy of Na in the liquid was obtained via the Gibbs–Helmholtz equation. The results are shown in fig. 19. Also, h^{E} of the liquid has been measured (KLEINSTUBER [1961]) by direct calorimetry.

Along the Cd-liquidus in fig. 17 the partial Gibbs energy of Cd in the liquid is equal to that of essentially pure solid Cd with which it is in equilibrium:

$$g^{l}_{Cd} = g^{o(s)}_{Cd} \tag{25}$$

Hence,

$$g^{l}_{Cd} - g^{o(l)}_{Cd} = g^{o(s)}_{Cd} - g^{o(l)}_{Cd} \tag{26}$$

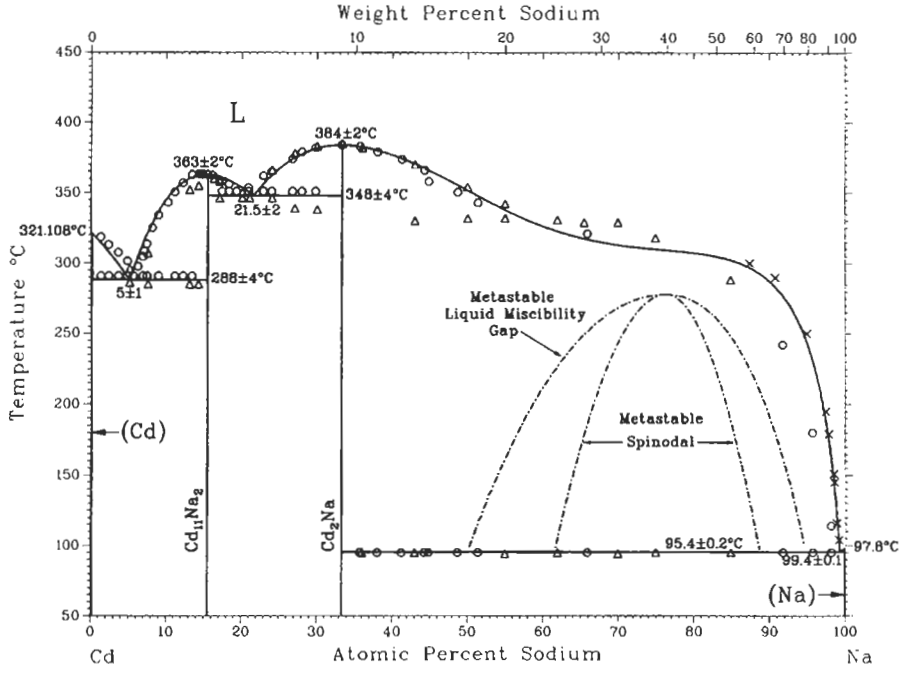

Fig. 17. Cd–Na phase diagram calculated from optimized thermodynamic parameters (Reprinted from PELTON [1988]).

o KURNAKOW and KUSNETZOV [1907]

Δ MATHEWSON [1906]

× WEEKS and DAVIES [1964]

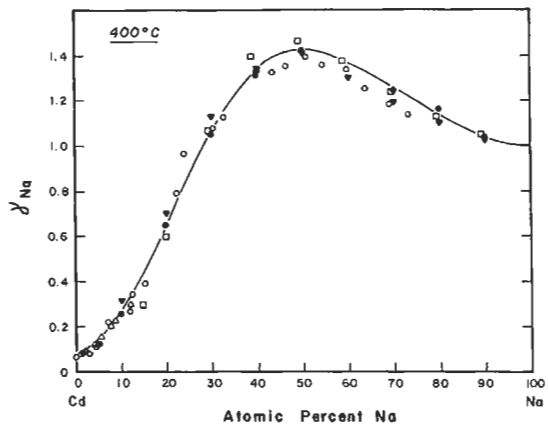

Fig. 18. Sodium activity coefficient in liquid Cd–Na alloys at 400°C. Line is calculated from optimized thermodynamic parameters (Reprinted from PELTON [1988]).
□ HAUFFE [1940]
● LANTRATOV and MIKHAILOVA [1971]
Δ MAIOROVA *et al.* [1976]
∇ ALABYSHEV and MORACHEVSKII [1957]
○ BARTLETT *et al.* [1970]

$$RT \ln X^{1}_{Cd} + g^{E(l)}_{Cd} = -\Delta g^{o}_{f(Cd)} \tag{27}$$

Therefore, from the experimental liquidus composition X^{1}_{Cd}, and from a knowledge of the Gibbs energy of fusion, $g^{E(l)}_{Cd}$ at the measured liquidus points can be calculated from eq. (27).

Similar equations relating the liquidus compositions along the $Cd_{11}Na_2$- and Cd_2Na-liquidus lines to the partial excess Gibbs energies of the liquid and to the Gibbs energies of fusion of $Cd_{11}Na_2$ and Cd_2Na can be written based upon the graphical construction shown in fig. 14.

The thermodynamic data for g^{E}_{Na}, h^{E}_{Na} and h^{E} as well as the measured liquidus points and the Gibbs energies of fusion of the compounds were optimized simultaneously by a least-squares technique to obtain the following optimized expressions (PELTON [1988]):

$$h^{E(l)} = X_{Cd}X_{Na}\left(-12508 + 20316\left(X_{Na} - X_{Cd}\right) - 8714\left(X_{Na} - X_{Cd}\right)^2\right) \text{J/mol} \tag{28}$$

$$s^{E(l)} = X_{Cd}X_{na}\left(-15.452 + 15.186\left(X_{Na} - X_{Cd}\right) - 10.062\left(X_{Na} - X_{Cd}\right)^2 - 1.122\left(X_{Na} - X_{Cd}\right)^3\right) \text{ J/mol K} \tag{29}$$

$$\Delta G^{o}_{f\left(\frac{1}{13}Cd_{11}Na_2\right)} = 6816 - 10.724\ T \quad \text{J/g-atom} \tag{30}$$

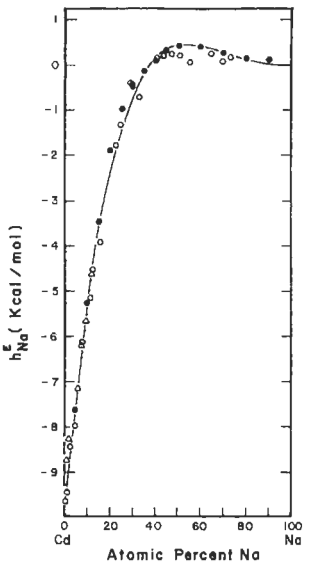

Fig. 19. Partial excess exthalpy of sodium in liquid Cd–Na alloys. Line is calculated from optimized thermodynamic parameters (Reprinted from PELTON [1988]).
● LANTRATOV and MIKHAILOVA [1971]
Δ MAIOROVA *et al.* [1976]
○ BARTLETT *et al.* [1970]

$$\Delta G^o_{f\left(\frac{1}{3}Cd_2Na\right)} = 8368 - 12.737\ T \quad \text{J/g-atom} \tag{31}$$

$$\Delta G^o_{f(Cd)} = 6201 - 10.4344\ T \quad \text{J/g - atom} \tag{32}$$

$$\Delta G^o_{f(Na)} = 2598 - 7.0035\ T \quad \text{J/g-atom} \tag{33}$$

The Gibbs energies of fusion of Cd and Na were taken from CHASE [1983] and were not changed in the optimization. The optimized enthalpies of fusion of 6816 and 8368 J/g-atom for the two compounds in eqs. (30, 31) were modified from the values of 6987 and 7878 J/g-atom measured by ROOS [1916]. These changes are within the experimental error limits. Eq. (28) reproduces the calorimetric data within 200 J/mol^{-1}. Eqs. (22, 24) can be used to calculate h^E_{Na} and γ^E_{Na}. The calculated curves are compared to the measured points in figs. 18 and 19. The phase diagram shown in fig. 17 was calculated from eqs. (28) to (33). Complete details of the analysis of the Cd–Na system are given by PELTON [1988].

It can thus be seen how one simple set of equations can simultaneously and self-consistently describe all the thermodynamic properties and the phase diagram of a binary system. The exact optimization procedure will vary from system to system depending on the type and accuracy of the available data, the number of phases present, the extent of

solid solubility, etc. A large number of optimizations have been published in the Calphad Journal since 1977.

2.10.3. Calculation of metastable phase boundaries

In the Cd–Na system just discussed, the liquid exhibits positive deviations from ideal mixing. That is, $g^{E(l)} > 0$. This fact is reflected in the very flat liquidus in fig. 17 as was discussed in § 2.5.2.

By simply not including any solid phases in the calculation, the metastable liquid miscibility gap as well as the spinodal curve (§ 2.3) can be calculated as shown in fig. 17. These curves are of importance in the formation of metallic glasses by rapid quenching (see ch. 19, § 2.1).

Other metastable phase boundaries, such as the extension of a liquidus curve below a eutectic, can also be calculated thermodynamically simply by excluding one or more phases during the computations.

2.11. Solution models

Polynomial expansions, as in eqs (18, 19), give an adequate representation of the excess mixing properties for simple substitutional solutions in which deviations from regular solution behaviour are not too large. In other cases, more sophisticated models are required.

The Gibbs energy of a regular solution is given by combining eqs. (2) and (4). The ideal mixing term in eq. (2) is a consequence of the assumption that A and B atoms form a random substitutional solution. The parameter Ω in eq (4) can be interpreted as resulting from the fact that the energy of A–B bonds in the solution is different from that of A–A and B–B bonds. Suppose that A–B bonds are energetically favourable. The solution is thereby stabilized, $\Omega < 0$ and $g^E < 0$. However, the distribution will then no longer be random because A and B atoms will tend to favour each other as nearest neighbours, and so the ideal mixing term, $RT(X_A \ln X_A + X_B \ln X_B)$ in eq. (2) is no longer correct. For relatively small deviations from ideality, the random mixing approximation is often acceptable. However, for larger deviations, the non-randomness becomes important. In such cases, a simple polynomial expansion for g^E as in eqs. (18, 19) is insufficient.

The regular solution model can be extended to account for this non-randomness through the *quasichemical model for short-range ordering* developed by GUGGENHEIM [1935] and FOWLER and GUGGENHEIM [1939]. Many liquid alloy solutions exhibit short-range ordering. The ordering is strongest when one component is relatively electropositive (on the left side of the periodic table) and the other is relatively electronegative. Liquid alloys such as Alk–Au (HENSEL [1979]), Alk–Pb (SABOUNGI *et al.* [1985]) and Alk–Bi (PETRIC *et al.* [1988]), where Alk = (Na, K, Rb, Cs) exhibit strong short-range ordering, as do liquid semiconductor solutions such as Ga–As and In–Sb. The quasichemical model has been recently adapted to permit thermodynamic/phase diagram optimizations of such systems (PELTON and BLANDER [1984, 1986, 1988]).

Short-range ordering in liquid alloys has also been modeled by treating such solutions as substitutional solutions of A atoms, B atoms and A_mB_n "complexes". See for example, LÜCK *et al.* [1989]. For most alloy systems, however, such *association models* are not physically realistic.

For an *interstitial solution* the ideal Gibbs energy of mixing is that of a random distribution of the solute atoms over the interstitial sites. For example, in an interstitial solution of C in γ-Fe, X_C moles of C atoms are distributed over X_{Fe} octahedral sites. The molar Gibbs energy of mixing is thus:

$$\begin{aligned}\Delta g &= RT\left(\frac{X_{Fe}}{X_{Fe}+X_C}\right)\left(\frac{X_C}{X_{Fe}}\ln\frac{X_C}{X_{Fe}}+\frac{(X_{Fe}-X_C)}{X_{Fe}}\ln\frac{(X_{Fe}-X_C)}{X_{Fe}}\right)\\ &= RT\left(X_C\ln\frac{X_C}{1-2X_C}+X_{Fe}\ln\left(1-\frac{X_C}{X_{Fe}}\right)\right)+g^E\end{aligned} \tag{34}$$

The ideal activities are thus:

$$a_C^{ideal} = X_C/(1-2X_C) \tag{35}$$

$$a_{Fe}^{ideal} = (1-X_C/X_{Fe}) \tag{36}$$

When modeling an interstitial solution, one should employ these expressions.

A multicomponent interstitial solution such as M_1–M_2–C–N, where M_1 and M_2 are metals, can be considered to consist of two sublattices: a metallic sublattice on which M_1 and M_2 are distributed, and an interstitial sublattice on which C, N (and vacant sites) are distributed. General sublattice models, of which such solutions are a special case, have been discussed by HILLERT *et al.* [1985]. An example of application to the Fe–Cr–V–C system is given in § 5.

Examples of *non-stoichiometric compound phases* were shown in figs 13 and 16. When these exhibit a relatively narrow range of stoichiometry, as is the case for $AgMg_3$ in fig. 14, the phase is conveniently described as a dilute solution of defects in the stoichiometric compound. For example, consider a compound $A_{1-y}B_y$. The lattice sites normally occupied by A atoms we shall call "A sites", and those normally occupied by B atoms are "B sites". The dissolution of excess B in the compound can occur by the formation of *defects*. Example of such defects are (i) B atoms occupying A sites; (ii) vacant A sites; (iii) B atoms occupying interstitial sites; etc. Generally, one type of defect will predominate in any given system when B is in excess, and this is called the majority defect for solutions with excess B. When excess A is added to $A_{1-y}B_y$, then another majority defect predominates. It should, of course, be noted that certain compounds, such as FeO, or Nb_3Al near room temperature, do not even contain the stoichiometric composition within their range of single-phase stoichiometry.

Despite the large number of defect types which can occur, a quite general thermodynamic model can be proposed. Let X_1 be the mole fraction of the majority defects which occur when A is in excess. This is the mole fraction of these defects on the sublattice (or interstitial lattice) which they occupy. Similarly, X_2 is the mole fraction of

the majority defects which occur when B is in excess. Let g_1 and g_2 be the energies required to form one mole of each type of defect in the limit when X_1 and X_2 are very small. Assume that the concentrations X_1 and X_2 are small enough that interactions between defects are negligible (Henry's Law) and that the number of lattice sites does not change appreciably from that in the defect-free compound. Assume further that the defects are randomly distributed. The molar Gibbs energy of the solution relative to the hypothetical defect-free compound is then:

$$g = \frac{RT}{\beta_1}\left(X_1 \ln X_1 + (1 - X_1)\ln(1 - X_1)\right) + \frac{RT}{\beta_2}\left(X_2 \ln X_2 + (1 - X_2)\ln(1 - X_2)\right) + \frac{1}{\beta_1} g_1 X_1 + \frac{1}{\beta_2} g_2 X_2 \tag{37}$$

where $1/\beta_1$ and $1/\beta_2$ are the numbers of moles of lattice sites available to each type of defect. For a given deviation from the stoichiometric composition represented by $A_{1-y-\delta}B_{y+\delta}$:

$$\delta = \frac{X_2}{\beta_2} - \frac{X_1}{\beta_1} \tag{38}$$

and by minimizing g with respect to X_1 and X_2 it can be shown that:

$$\left(\frac{X_1}{1 - X_1}\right)^{\frac{1}{\beta_1}} \left(\frac{X_2}{1 - X_2}\right)^{\frac{1}{\beta 2}} = \exp\left(\frac{-\left(\frac{g_1}{\beta_1} + \frac{g_2}{\beta_2}\right)}{RT}\right) \tag{39}$$

If values of the energy parameters g_1 and g_2 are given, eqs. (38, 39) can be solved for any δ to give X_1 and X_2 which can then be substituted back into eq. (37) to give g. When g_1 and g_2 are very large, g rises very steeply on either side of its minimum, and the range of stoichiometry is very narrow as for the case of the compounds in fig. 14. In the case of the compound $AgMg_3$ in fig. 13, $g_1 > g_2$. That is, it is easier to form defects by adding excess Mg than by adding excess Ag. Hence, the Gibbs energy curve rises more steeply on the Ag side, and as a result, Mg is more soluble in $AgMg_3$ than is Ag.

Defects are discussed in chs. 9, 18 and 20. For an example of an application of the defect model to phase diagram calculations, see PELTON [1991]. For a treatment of defect models as examples of general sublattice models, see HILLERT *et al.* [1985].

2.12. Binary phase diagrams involving a gaseous phase

The effect of total pressure, P, upon the Gibbs energy change for the transformation of one mole of pure component A from the α- to the β-phase is given by:

$$\Delta g_A^{\alpha\to\beta} = \Delta g_A^{0(\alpha\to\beta)} + \int_{P=1}^{P} \left(v_A^{\beta} - v_A^{\alpha}\right) dP, \tag{40}$$

where $\Delta g_A^{0(\alpha-\beta)}$ is the standard (i.e. at $P = 1$ atm) molar Gibbs energy of transformation and where v_A^α and v_B^α are the molar volumes of the phases. For solids and liquids, molar volumes are sufficiently small that the final term in eq. (40) is negligible unless P is very large. If a gaseous phase is involved, however, this is no longer the case. If gaseous A is ideal and monatomic, and since $v_A^g = RT/P >> v_A^l$, the molar Gibbs energy of vaporization is given by:

$$\Delta g_A^v = \Delta g_A^{0(v)} + RT \ln P . \tag{41}$$

where $\Delta g_A^{0(v)}$ is the standard Gibbs energy of vaporization (when P = 1 atm) which is given by:

$$\Delta g_A^{0(v)} = \Delta h_A^{0(v)} - T\Delta s_A^{0(v)} \tag{42}$$

For example, the enthalpy of vaporization of Zn is $\Delta h_{Zn}^{0(v)} = 115300$ J/mol at its normal boiling point of 1180 K (BARIN *et al.* [1977]). Assuming that $\Delta h^{0(v)}$ is independent of T, we calculate that $\Delta s_{Zn}^{0(v)} = 115300/1180 = 97.71$ J/mol K. Hence, Δg_{Zn}^v at any T and P is given by:

$$\Delta g_{Zn}^v = (115300 - 97.71T) + RT \ln P \tag{43}$$

A similar expression can be derived for the other component, Mg.

Curves of g^l and g^v at a constant T and P are shown in the upper panel of fig. 20. The common tangent construction generates the equilibrium vapour and liquid compositions. A temperature–composition phase diagram, at constant pressure, can then be generated as the curve for g^v descends relative to g^l as the temperature is raised. Alternatively, the isothermal pressure–composition diagram shown in the lower panel of fig. 20 is generated as the curve for g^v descends relative to g^l as the pressure is lowered. The diagram at 1250 K in fig. 20 was calculated under the assumption of ideal liquid and vapour mixing ($g^{E(l)} = g^{E(v)} = 0$).

3. *Ternary phase diagrams*

In this section, an introduction to ternary phase diagrams will be given. A complete discussion of the subject is beyond the scope of this chapter. For more detailed treatments see PRINCE [1966], WEST [1965] or BERGERON and RISBUD [1984].

3.1. The ternary composition triangle

In a ternary system with components A–B–C the sum of the mole fractions is unity. $(X_A + X_B + X_C) = 1$. Hence, there are two independent composition variables. A representation of composition, symmetrical with respect to all three components may be obtained with the equilateral "composition triangle" as shown in fig. 21. Compositions at the corners of the triangle correspond to the pure components. Along the edges of the triangle are found compositions corresponding to the three binary subsystems A–B, B–C and C–A. Lines of constant mole fraction X_A are parallel to the B–C edge, while lines of

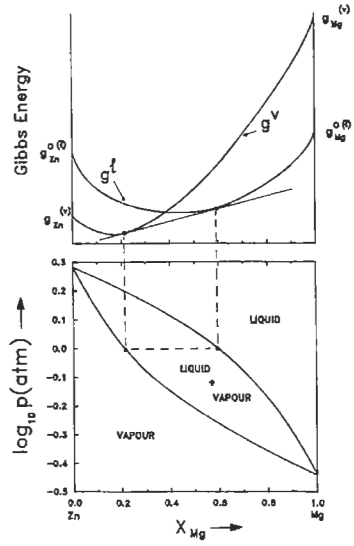

Fig. 20. Pressure-composition phase diagram of the Zn–Mg system at 1250 K calculated for ideal vapour and liquid solutions. Upper panel illustrates common tangent construction at a constant pressure and temperature.

constant X_B and X_C are parallel to the C–A and A–B edges respectively. For example at point **a** in fig. 21, $X_A = 0$, $X_B = 0.7$ and $X_C = 0.3$. At point **b**, $X_A = 0.3$, $X_B = 0.2$ and $X_C = 0.5$.

Similar equilateral composition triangles can also be drawn with coordinates in terms of weight% of the three components.

3.2. Ternary space model

A ternary temperature–composition "phase diagram" at constant total pressure may be plotted as a three-dimensional "space model" within a right triangular prism with the equilateral composition triangle as base and temperature as vertical axis. Such a space model for a simple eutectic ternary system A–B–C is illustrated in fig. 22. On the three vertical faces of the prism we find the phase diagrams of the three binary subsystems, A–B, B–C and C–A which, in this example, are all simple eutectic binary systems. The binary eutectic points are at $\mathbf{e}_1$, $\mathbf{e}_2$ and $\mathbf{e}_3$. Within the prism we see three *liquidus surfaces* descending from the melting points of pure A, B and C. Compositions on these surfaces correspond to compositions of liquid in equilibrium with A-, B- and C-rich solid phases.

In a ternary system at constant pressure, the Gibbs phase rule, eq. (14), becomes:

$$F = 4 - P. \tag{44}$$

When the liquid and one solid phase are in equilibrium, $P = 2$. Hence, $F = 2$, and the system is bivariant. A ternary liquidus is thus a two-dimensional surface. We may choose two variables, say T and one composition coordinate of the liquid, but then the other liquid composition coordinate and the composition of the solid are fixed.

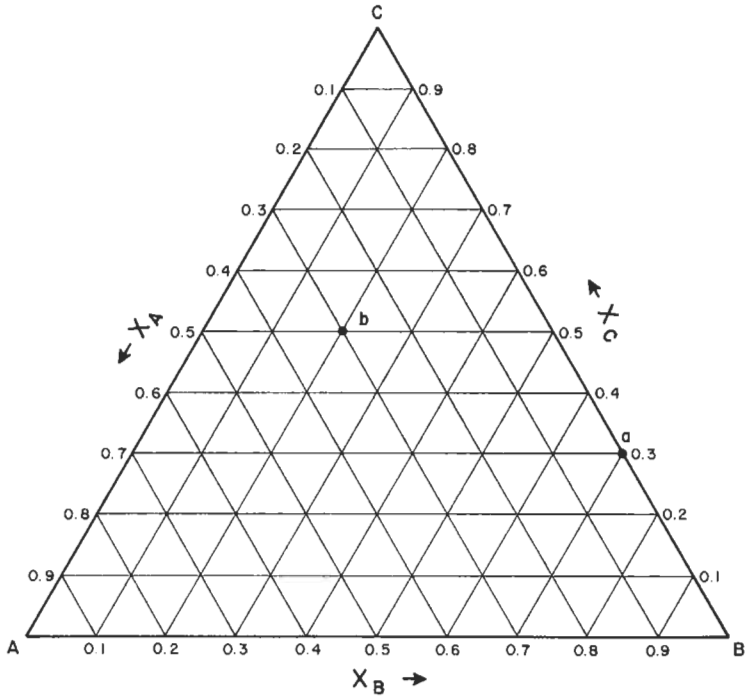

Fig. 21. The equilateral ternary composition triangle.

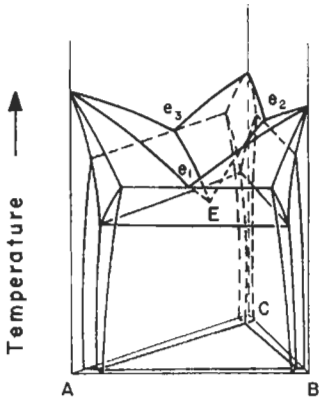

Fig. 22. Perspective view of ternary space model of a simple eutectic ternary system. $\mathbf{e}_1$, $\mathbf{e}_2$, $\mathbf{e}_3$ are the binary eutectics and **E** is the ternary eutectic. The base of the prism is the equilateral composition triangle.

References: p. 531.

The A- and B-liquidus surfaces in fig. 22 intersect along the line $\mathbf{e}_1$E. Liquids with 0compositions along this line are therefore in equilibrium with A-rich and B-rich solid phases simultaneously. That is, $P=3$ and so $F=1$. Such "valleys" are thus called *univariant lines*. The three univariant lines meet at the *ternary eutectic point* E at which $P=4$ and $F=0$. This is an invariant point since the temperature and the compositions of all four phases in equilibrium are fixed.

3.3. Polythermal projections of liquidus surfaces

A two-dimensional representation of the ternary liquidus surface may be obtained as an orthogonal projection upon the base composition triangle. Such a *polythermal projection* of the liquidus of the Bi–Sn–Cd system (BRAY *et al.* [1961–62]) is shown in fig. 23. This is a simple eutectic ternary system with a space model like that shown in fig. 22. The constant temperature lines on fig. 23 are called *liquidus isotherms*. The univariant valleys are shown as the heavier lines. By convention, the large arrows indicate the directions of decreasing temperature along these lines.

Let us consider the sequence of events which occur during the equilibrium cooling from the liquid of an alloy of overall composition **a** in fig. 23 ($X_{Bi}=0.05$, $X_{Sn}=0.45$, $X_{Cd}=0.50$). Point **a** lies within the *field of primary crystallization* of Cd. That is, it lies within the composition region in fig. 23 in which Cd-rich solid will be the first solid to precipitate upon cooling. As the liquid alloy is cooled, the Cd-liquidus surface is reached at $T \approx 465$ K (slightly below the 473 K isotherm). A solid Cd-rich phase begins to precipitate at this temperature. Now, in this particular system, Bi and Sn are nearly insoluble in solid Cd, so that the solid phase is virtually pure Cd (note that this fact cannot be deduced from fig. 23 alone). Therefore, as solidification proceeds, the liquid becomes depleted in Cd, but the ratio X_{Sn}/X_{Bi} in the liquid remains constant. Hence, the composition path followed by the liquid (its *crystallization path*) is a straight line passing through point **a** and projecting to the Cd-corner of the triangle. This crystallization path is shown on fig. 23 as the line **ab**.

In the general case in which a solid solution rather than a pure component or stoichiometric compound is precipitating, the crystallization path will not be a straight line. However, for equilibrium cooling, a straight line joining a point on the crystallization path at any T to the overall composition point **a** will extend through the composition, on the solidus surface, of the solid phase in equilibrium with the liquid at that temperature.

When the composition of the liquid has reached point **b** in fig. 23 at $T \approx 435$ K, the relative proportions of the solid Cd and liquid phases at equilibrium are given by the *lever rule* applied to the *tie-line* **dab**: (moles of liquid)/(moles of Cd) = **da**/**ab**, where **da** and **ab** are the lengths of the line segments. Upon further cooling the liquid composition follows the univariant valley from **b** to E while Cd and Sn-rich solids co-precipitate as a binary eutectic mixture. When the liquidus composition attains the ternary eutectic composition E at $T \approx 380$ K the invariant *ternary eutectic reaction* occurs:

$$\text{liquid} \rightarrow s_1 + s_2 + s_3, \tag{45}$$

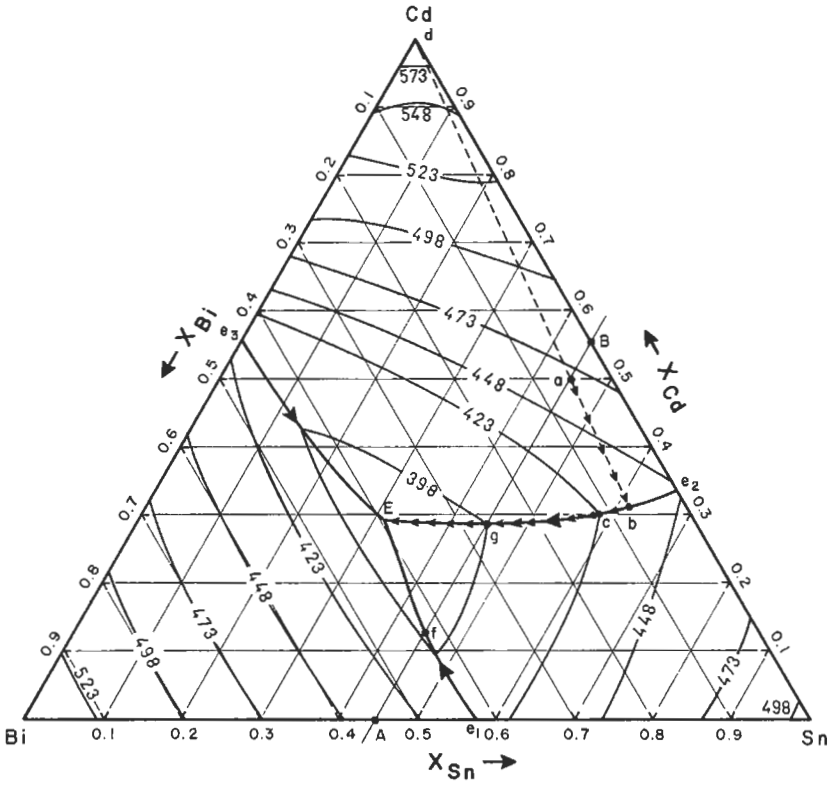

Fig. 23. Projection of the liquidus surface of the Bi–Sn–Cd system (after BRAY *et al.* [1961–62]). Small arrows show crystallization path of an alloy of overall composition at point **a**.

where s_1, s_2 and s_3 are the three solid phases and where the compositions of all four phases as well as T remain fixed until all liquid is solidified.

In order to illustrate several of the features of polythermal projections of liquidus surfaces, a projection of the liquidus of a hypothetical system A–B–C is shown in fig. 24. For the sake of simplicity, isotherms are not shown, but only the univariant lines with arrows to show the directions of decreasing temperature. The binary subsystems A–B and C–A are simple eutectic systems, while the binary subsystem B–C contains one congruent binary phase, ε and one incongruent binary phase, δ, as shown in the insert in fig. 24. The letters **e** and **p** indicate binary eutectic and peritectic points. The ε and δ phases are called *binary compounds* since they have compositions within a binary subsystem. Two *ternary compounds*, η and ζ, with compositions within the ternary triangle as indicated in fig. 24, are also found in this system. All compounds as well as pure solid A, B and C (the "α, β and γ" phases) are assumed to be stoichiometric (i.e. there is no solid solubility). The fields of primary crystallization of all the solids are indicated in parentheses in fig. 24. The composition of the ε phase lies within its field,

References: p. 531.

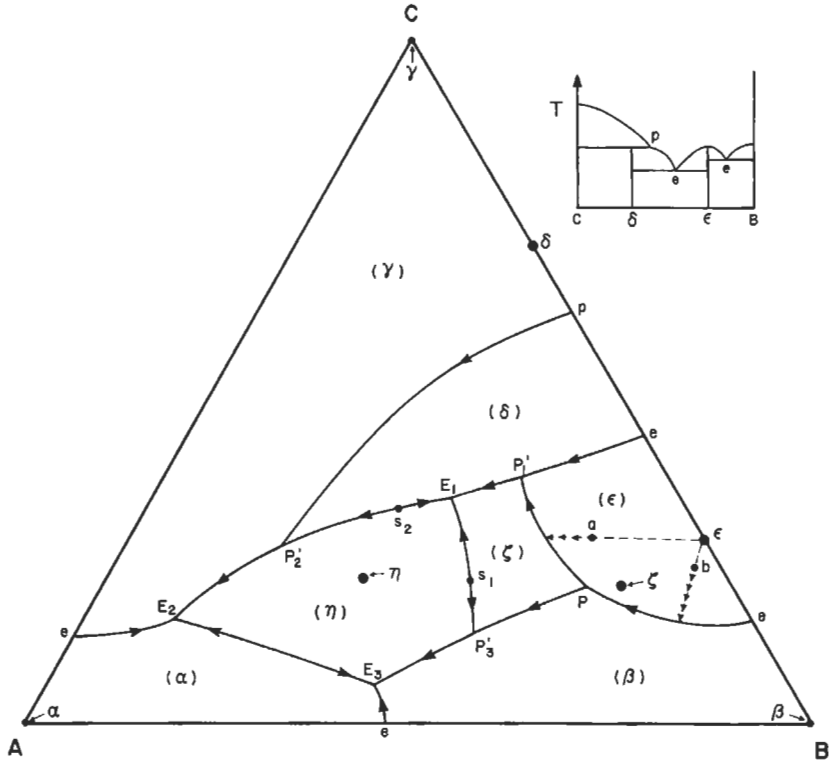

Fig. 24. Projection of the liquidus surface of a system A–B–C. The binary subsystems A–B and C–A are simple eutectic systems. The binary phase diagram B–C is shown in the insert. All solid phases are assumed pure stoichiometric components or compounds. Small arrows show crystallization paths of alloys of compositions at points **a** and **b**.

since ε is a congruent compound, while the composition of the δ phase lies outside of its field since δ is incongruent. Similarly for the ternary compounds, η is a congruently melting compound while ζ is incongruent. For the congruent compound η, the highest temperature on the η-liquidus occurs at the composition of η.

The univariant lines meet at a number of *ternary eutectics* E_i (three arrows converging), a *ternary peritectic* P (one arrow entering, two arrows leaving the point), and several *ternary quasi-peritectics* P'_i (two arrows entering, one arrow leaving). Two *saddle points* **s** are also shown. These are points of maximum T along the univariant line but of minimum T on the liquidus surface along a section joining the compositions of the two solids. For example, $\mathbf{s}_1$ is at a maximum along the univariant $E_1P'_3$, but is a minimum point on the liquidus along the straight line $\zeta\mathbf{s}_1\eta$.

Let us consider the events occurring during the cooling from the liquid of an alloy of overall composition **a** in fig. 24. The primary crystallization product will be the ε phase. Since this is a pure stoichiometric solid the crystallization path of the liquid will be along

a straight line passing through **a** and extending to the composition of ε as shown on the figure.

Solidification of ε continues until the liquid attains a composition on the univariant valley. Then the liquid composition follows the valley towards the point P_1' in co-existence with ε and ζ. At point P_1' the invariant *ternary quasi-peritectic reaction* occurs isothermally:

$$\text{liquid} + \varepsilon \rightarrow \delta + \zeta. \tag{46}$$

Since there are two reactants in a quasi-peritectic reaction, there are two possible outcomes: (i) The liquid is completely consumed before the ε-phase; in this case, solidification will be complete at the point P_1'. (ii) ε is completely consumed before the liquid; in this case, solidification will continue with decreasing T along the univariant line $P_1'E_1$ with co-precipitation of δ and ζ until, at E, the liquid will solidify eutectically (liquid $\rightarrow \delta + \zeta + \eta$). To determine whether condition (i) or (ii) occurs, we use the mass balance criterion that, for three-phase equilibrium, the overall composition must always lie within the *tie-triangle* formed by the compositions of the three phases. Now, the triangle joining the compositions of δ, ε, and ζ does not contain the point **a**, but the triangle joining the compositions of δ, ζ, and liquid at P_1' does contain the point **a**. Hence, case (ii) occurs.

An alloy of overall composition **b** in fig. 24 solidifies with ε as primary crystallization product until the liquid composition contacts the univariant line. Thereafter, co-precipitation of ε and β occurs with the liquid composition following the univariant valley until the liquid reaches the peritectic composition P. The invariant *ternary peritectic reaction* then occurs isothermally:

$$\text{liquid} + \varepsilon + \beta \rightarrow \zeta. \tag{47}$$

Since there are three reactants, there are three possible outcomes: (i) Liquid is consumed before either ε or β and solidification terminates at P. (ii) ε is consumed first; solidification then continues along the path PP_3'. (iii) β is consumed first and solidification continues along the path PP_1'. Which outcome occurs depends on whether the overall composition **b** lies within the tie-triangle (i) $\varepsilon\beta\zeta$, (ii) $\beta\zeta$P or (iii) $\varepsilon\zeta$P. In the example shown, case (i) will occur.

3.4. Ternary isothermal sections

Isothermal projections of the liquidus surface do not give information on the compositions of the solid phases at equilibrium. However, this information can be presented at any one temperature on an *isothermal section* such as that shown for the Bi–Sn–Cd system at 423 K in fig. 25. This phase diagram is a constant temperature slice through the space model of fig. 22.

The liquidus lines bordering the one-phase liquid region of fig. 25 are identical to the 423 K isotherms of the projection in fig. 23. Point **c** in fig. 25 is point **c** on the univariant line in fig. 23. An alloy with overall composition in the one-phase liquid region of fig. 25 at 423 K will consist of a single liquid phase. If the overall composition lies within one of the two-phase regions, then the compositions of the two phases are given

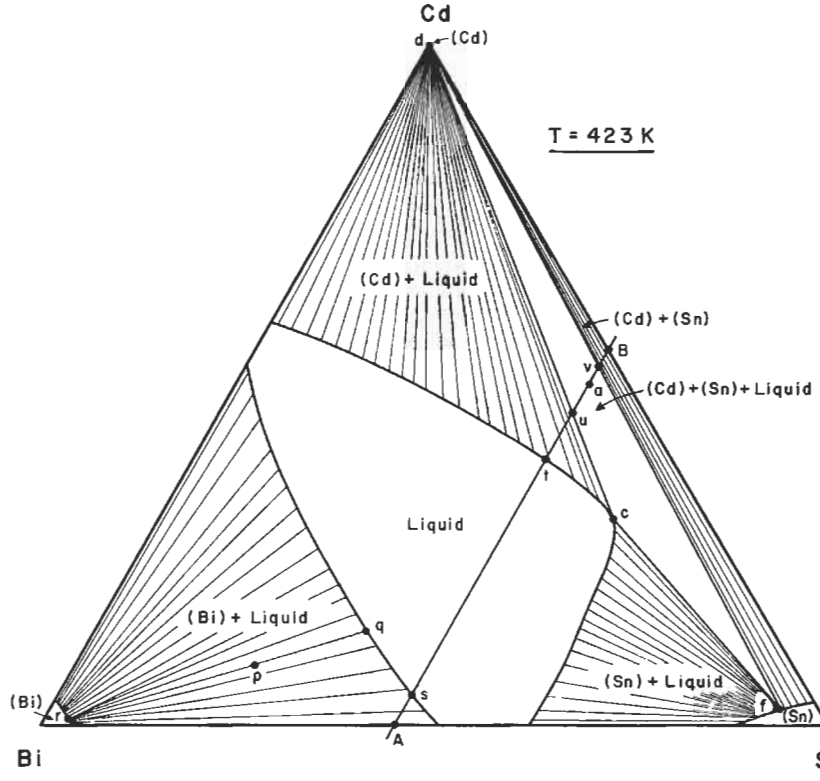

Fig. 25. Isothermal section of Bi–Sn–Cd system at 423 K (after BRAY *et al.* [1961–62]). Extents of solid solubility in Bi and Sn have been exaggerated for clarity of presentation.

by the ends of the *tie-line* containing the overall composition. For example, a sample with overall composition **p** in fig. 25 will consist of a liquid of composition **q** on the liquidus and a solid Bi-rich alloy of composition **r** on the solidus. The relative proportions of the two phases are given by the lever rule: (moles of liquid)/(moles of solid) = **pr**/**pq**, where **pr** and **pq** are the lengths of the line segments.

In the case of solid Cd, the solid phase is nearly pure Cd, so all tie-lines of the (Cd + liquid) region converge nearly to the corner of the triangle. In the case of Bi- and Sn-rich solids, some solid solubility is observed. (The actual extent of this solubility is somewhat exaggerated in fig. 25 for the sake of clarity of presentation.) Alloys with overall compositions rich enough in Bi or Sn to lie within the single-phase (Sn) or (Bi) regions of fig. 25 will consist, at 423 K, of single-phase solid solutions. Alloys with overall compositions at 423 K in the two-phase (Cd + Sn) region will consist of two solid phases.

Alloys with overall compositions within the three-phase triangle **dcf** will, at 423 K, consist of three phases: Cd- and Sn-rich solids with compositions at **d** and **f**, and liquid

of composition **c**. To understand this better, consider an alloy of composition **a** in fig. 25, which is the same composition as the point **a** in fig. 23. In § 3.3 we saw that when a alloy of this composition is cooled, the liquid follows the path **ab** on fig. 23 with primary precipitation of Cd and then follows the univariant line with co-precipitation of Cd and Sn so that at 423 K the liquid will be at the composition point **c**, and two solid phases are in equilibrium with the liquid.

3.4.1. Topology of ternary isothermal sections

At constant temperature the Gibbs energy of each phase in a ternary system is represented as a function of composition by a surface plotted in a right triangular prism with Gibbs energy as vertical axis and the composition triangle as base. Just as the compositions of phases at equilibrium in binary systems are determined by the points of contact of a common tangent line to their isothermal Gibbs energy curves, so the compositions of phases at equilibrium in a ternary system are given by the points of contact of a common tangent plane to their isothermal Gibbs energy surfaces. A common tangent plane can contact two Gibbs energy surfaces at an infinite number of pairs of points. thereby generating an infinite number of tie-lines within a two-phase area on an isothermal section. A common tangent plane to three Gibbs energy surfaces contacts each surface at a unique point, thereby generating a three-phase tie-triangle.

Hence, the principal topological units of construction of an isothermal ternary phase diagram are three-phase ($\alpha + \beta + \gamma$) tie-triangles as in fig. 26 with their accompanying two-phase and single-phase areas. Each corner of the tie-triangle contacts a single-phase region, and from each edge of the triangle there extends a two-phase region. The edge of the triangle is a limiting tie-line of the two-phase region.

For overall compositions within the tie-triangle, the compositions of the three phases at equilibrium are fixed at the corners of the triangle. The relative proportions of the three phases are given by the *lever rule* of tie-triangles which can be derived from mass balance considerations. At an overall composition **q** in fig. 26, for example, the relative proportion of the γ-phase is given by projecting a straight line from the γ-corner of the triangle (point **c**) through the overall composition **q** to the opposite side of the triangle, point **p**. Then: (moles of γ)/(total moles) = **qp/cp** if compositions are expressed in mole fractions, or (weight of γ)/(total weight) = **qp/cp** if compositions are in weight percent.

Isothermal ternary phase diagrams are generally composed of a number of these topological units. An example for the Al–Zn–Mg system at 25°C is shown in fig. 27 (KÖSTER and DULLENKOPF [1936]). The β, γ, δ, θ, η and ζ phases are binary intermetallic compounds with small (~1%) ranges of stoichiometry which can dissolve a limited amount (~1–6%) of the third component. The τ phase is a ternary phase with a single-phase region existing over a fairly extensive oval-shaped central composition range. Examination of fig. 27 shows that it consists of the topological units of fig. 26.

An extension rule, a case of *Schreinemakers's rule* (SCHREINEMAKERS [1915]) for ternary tie-triangles is illustrated in fig. 26. At each corner, the extension of the boundaries of the single-phase regions, indicated by the dashed lines, must either both project into the triangle as at point **a**, or must both project outside the triangle as at point **b**, and furthermore the angle between these extensions must be less than 180°. For a proof, see LIPSON and WILSON [1940].

References: p. 531.

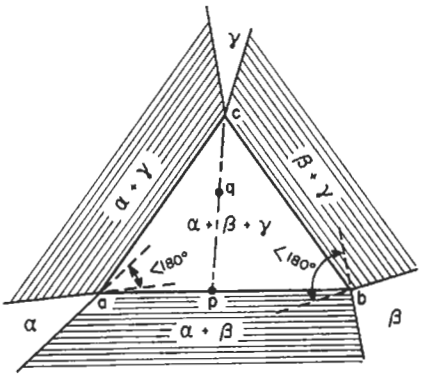

Fig. 26. A tie-triangle in a ternary isothermal section illustrating the lever rule and the extension rule.

Many published phase diagrams violate this rule. For example, it is violated in fig. 27 at the δ-corner of the $(\varepsilon + \delta + \tau)$ tie-triangle.

Another important rule of construction, whose derivation is evident, is that within any two-phase region tie-lines must never cross each other.

3.5. Ternary isopleths (constant composition sections)

A vertical *isopleth*, or constant composition section through the space model of the Bi–Sn–Cd system is shown in fig. 28. The section follows the line **AB** in fig. 23.

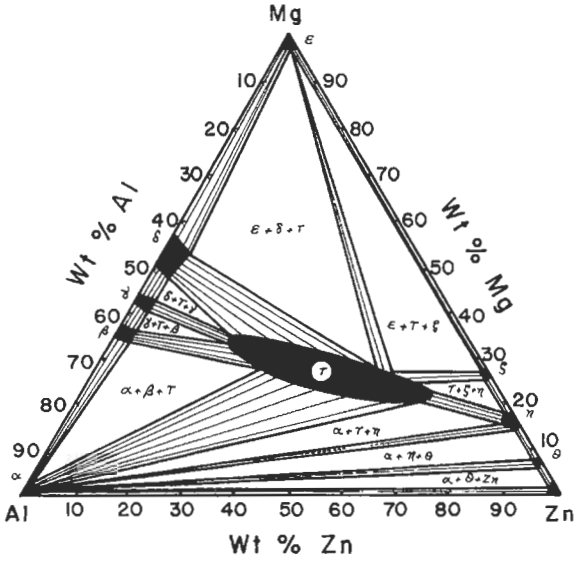

Fig. 27. Ternary isothermal section of the Al–Zn–Mg system at 25°C (after KÖSTER and DULLENKOPF [1936]).

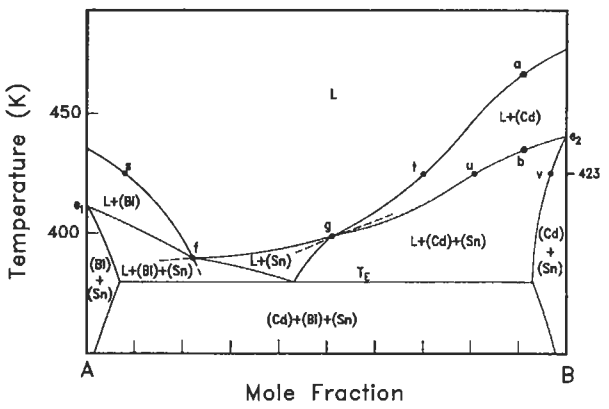

Fig. 28. Isopleth (constant composition section) of the Bi–Sn–Cd system following the line **AB** of fig. 23.

The phase fields on fig. 28 indicate which phases are present when an alloy with an overall composition on the line **AB** is equilibrated at any temperature. For example, consider the cooling from the liquid state, of an alloy of composition **a** which is on the line **AB** (see fig. 23). At T ≈ 465 K, precipitation of the solid (Cd) phase begins at point **a** in fig. 28. At T ≈ 435 K (point **b** in figs. 23 and 28) the solid (Sn) phase begins to appear. Finally, at the eutectic temperature T_E, the ternary eutectic reaction occurs, leaving solid (Cd) + (Bi) + (Sn) at lower temperatures. The intersection of the isopleth with the univariant lines on fig. 23 occurs at points **f** and **g** which are also indicated in fig. 28. The intersection of this isopleth with the isothermal section at 423 K is shown in fig. 25. The points **s**, **t**, **u** and **v** of fig. 25 are also shown on fig. 28.

It is important to note that on an isopleth, the tie-lines do not, in general, lie in the plane of the diagram. Therefore, the diagram gives information only on which phases are present, not on their compositions. The boundary lines on an isopleth do not in general indicate the phase compositions, but only the temperature at which a phase appears or disappears for a given overall composition. The lever rule cannot be applied on an isopleth.

Certain topological rules apply to isopleths. As a phase boundary line is crossed, one and only one phase either appears or disappears. This *Law of Adjoining Phase Regions* (PALATNIK and LANDAU [1964]) is illustrated by fig. 28. The only apparent exception occurs for the horizontal invariant line at T_E. However, if we consider this line to be a degenerate infinitely narrow four-phase region (L + (Cd) + (Bi) + (Sn)), then the law is also obeyed here.

Three or four boundary lines meet at intersection points. At an intersection point, *Schreinemakers' rule* applies (SCHREINEMAKERS [1915]). This rule states that the boundaries of the phase field with the smallest number of phases, when extrapolated, must either both fall within the phase field with the greatest number of phases (as at point **f** in fig. 28) or else both fall outside this region (as at point **g** in fig. 28).

Apparent exceptions to these rules (such as, for example, five boundaries meeting at an intersection point) can occur if the section passes exactly through a node (such as a ternary eutectic point) of the space model. However, these apparent exceptions are really only limiting cases. See PRINCE [1963] or PRINCE [1966].

References: p. 531.

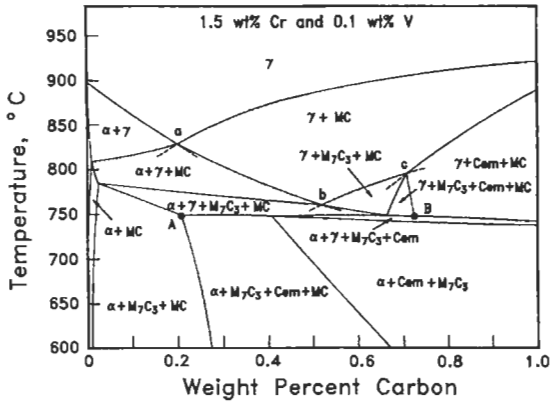

Fig. 29. Section of the Fe–Cr–V–C system at 1.5 wt.% Cr and 0.1 wt.% V (LEE and LEE [1992]).

4. *Multicomponent phase diagrams*

Only a brief outline of multicomponent phase diagrams can be presented here. For more detailed treatments see PALATNIK and LANDAU [1964], PRINCE [1963], PRINCE [1966] and HILLERT [1985].

For alloy systems of four or more components, two-dimensional sections are usually plotted with one or more compositional variables held constant. Hence, these sections are similar to the ternary isopleths discussed in § 3.5. In certain cases, sections at constant chemical potential of one or more components (for example, at constant oxygen partial pressure) can be useful. These are discussed in § 6.

Two sections of the Fe–Cr–V–C system (LEE and LEE [1992]) are shown in figs. 29, 30. The diagram in fig. 29 is a T-composition section at constant Cr and V content, while fig. 30 is a section at constant T = 850°C and constant C content of 0.3 wt.%. The

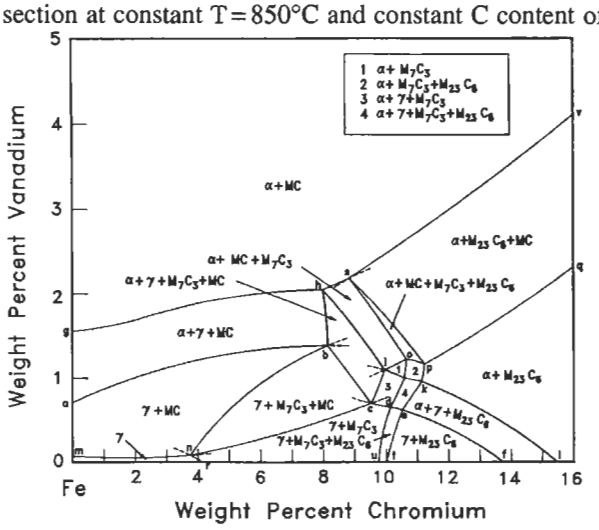

Fig. 30. Section of the Fe–Cr–V–C system at 850°C and 0.3 wt.% C (LEE and LEE [1992]).

interpretation and topological rules of construction of these sections are the same as those for ternary isopleths as discussed in § 3.5. In fact, the same rules apply to a two-dimensional constant–composition section for a system of any number of components. The phase fields on the diagram indicate the phases present at equilibrium for an overall composition lying on the section. Tie-lines do not, in general, lie in the plane of the diagram so the diagram does not give information on the compositions or amounts of the phases present. As a phase boundary is crossed, one and only one phase appears or disappears (Law of Adjoining Phase Regions). If temperature is an axis, as in fig. 29, then horizontal invariants like the line AB in fig. 29 can appear. These can be considered as degenerate infinitely narrow phase fields of (C + 1) phases, where C is the number of components (for isobaric diagrams). For example in fig. 29, on the line AB, five phases are present. Three or four phase boundaries meet at intersection points at which *Schreinemakers' rule* applies. This rule was given in § 3.5. It is illustrated by the extrapolations in fig. 29 at points **a**, **b** and **c** and in fig. 30 at points **b**, **c**, **n**, **i** and **s**. The applicability of Schreinemakers' rule to systems of any number of components was noted by HILLERT [1985], although no formal proof has been presented.

4.1. Zero phase fraction lines

An interesting and useful method of constructing multicomponent phase diagrams through the use of *zero phase fraction (ZPF)* lines has recently been proposed (GUPTA *et al.* [1986]). A ZPF line divides a two-dimensional phase diagram into two regions. On one side of the line a phase occurs, while on the other side it does not. For example, in fig. 30 the ZPF line for the α phase is the line **abcdef**. The ZPF line for the γ phase is **ghijkl**. For the MC phase the ZPF line is **mnciopq**. The ZPF line for M_7C_3 is **rnbhspket**, and for $M_{23}C_6$ it is **udjosv**. These five ZPF lines yield the entire two-dimensional phase diagram. The usefulness of this methodology for estimating phase diagrams for multicomponent systems from experimental data was discussed by GUPTA *et al.* [1986]. The method also holds promise for the thermodynamic calculation of phase diagrams (§ 5).

4.2. Nomenclature for invariant reactions

As discussed in § 2.9, in a binary isobaric temperature–composition phase diagram there are two possible types of invariant reactions: "eutectic type" invariant reactions ($\beta \rightarrow \alpha + \gamma$), and "peritectic type" invariant reactions ($\alpha + \gamma \rightarrow \beta$). In a ternary system, there are "eutectic type" ($\alpha \rightarrow \beta + \gamma + \delta$), "peritectic type" ($\alpha + \beta + \gamma \rightarrow \delta$) and "quasi-peritectic type" ($\alpha + \beta \rightarrow \gamma + \delta$) invariants (§ 3.3). In a system of C components, the number of types of invariant reaction is equal to C. A reaction with one reactant, such as $\alpha \rightarrow \beta + \gamma + \delta + \varepsilon$ is clearly a "eutectic type" invariant reaction but in general there is no standard terminology. These reactions are conveniently described according to the numbers of reactants and products (in the direction which occurs upon cooling). Hence, the reaction $\alpha + \beta \rightarrow \gamma + \delta + \varepsilon$ is a $2 \rightarrow 3$ reaction; the reaction $\alpha \rightarrow \beta + \gamma + \delta$ is a $1 \rightarrow 3$ reaction; and so on. The ternary peritectic type $3 \rightarrow 1$ reaction ($\alpha + \beta + \gamma \rightarrow \delta$) is an invariant reaction in a ternary system, a univariant reaction in a quaternary system, a bivariant reaction in a quinary system, etc.

References: p. 531.

5. *Thermodynamic calculation of ternary and multicomponent phase diagrams*

Among 70 metallic elements are formed $70!/3!67! = 54740$ ternary systems and 916895 quaternary systems. In view of the amount of work involved in measuring even one isothermal section of a relatively simple ternary phase diagram, it is very important to have means of estimating ternary and higher-order phase diagrams. The most fruitful approach to such predictions is via thermodynamic methods. In recent years, large advances have been made in this area by the international Calphad group. Many key papers have been published in the Calphad Journal.

As a first step in the thermodynamic approach to calculating a ternary phase diagram one critically analyzes the experimental phase diagrams and thermodynamic data for the three binary subsystems of the ternary system in order to obtain a set of mathematical expressions for the Gibbs energies of the binary phases as was discussed in § 2.10 and § 2.11. Next, equations based on solution models are used to estimate the Gibbs energies of the ternary phases from the Gibbs energies of the binary phases. The ternary phase diagram is then calculated from these estimated ternary Gibbs energies by means of common tangent plane or total Gibbs energy minimization algorithms.

For a phase for which the excess Gibbs energies in the binary systems have been expressed by polynomial expansions (§ 2.10.1) a satisfactory estimation of the Gibbs energy of the ternary phase can often be obtained with the following equation proposed by KOHLER [1960]:

$$g^{E} = (1 - X_A)^2 g^{E}_{B/C} + (1 - X_B)^2 g^{E}_{C/A} + (1 - X_C)^2 g^{E}_{A/B} \tag{48}$$

In this equation, g^E is the excess molar Gibbs energy at a composition point in the ternary phase and $g^E_{B/C}$, $g^E_{C/A}$ and $g^E_{A/B}$ are the excess Gibbs energies in the three binary subsystems at the same molar ratios X_B/X_C, X_C/X_A and X_A/X_B as at the ternary point. If the ternary solution as well as the three binary solutions are all regular then eq. (48) is exact. In the general case, a physical interpretation of eq. (48) is that the contribution to g^E from, say, pair interactions between A and B particles is constant at a constant ratio X_A/X_B apart from the dilutive effect of the C particles which is accounted for by the term $(1 - X_C)^2$ taken from regular solution theory. Other very similar equations, all based upon extension of regular solution theory, are also regularly used. These all give quite similar results. For a discussion see SPENCER and BARIN [1979] or HILLERT [1980].

For more complex solutions involving structural ordering or more than one sublattice, appropriate solution models for representing the binary properties have been discussed in § 2.11. In such cases, eq. (48) or similar equations should not be used for estimating the ternary excess Gibbs energies. Rather, equations consistent with the appropriate solution model should be used. For the quasichemical model, these have been discussed by PELTON and BLANDER [1986]. For the sublattice model, see HILLERT *et al.* [1985].

As an example of the calculation of a ternary phase diagram, the experimental isothermal section at 923 K of the Cr–Ni–Fe phase diagram is compared in fig. 31 with the diagram calculated solely from optimized binary thermodynamic properties (CHART

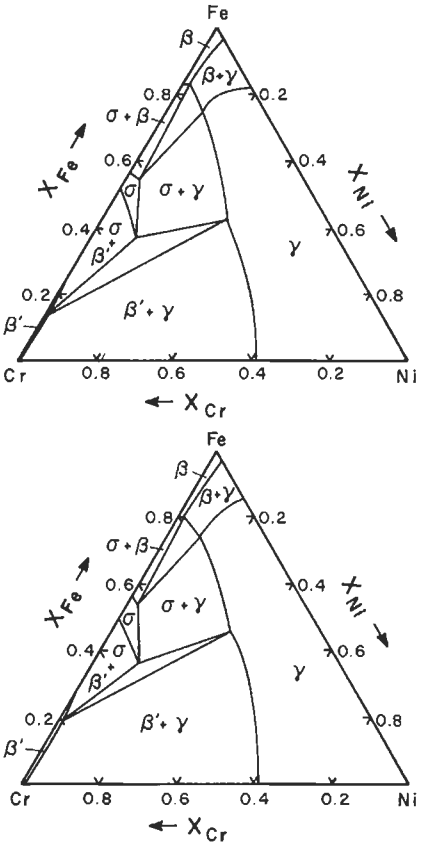

Fig. 31. Isothermal section at 923 K of the Cr–Ni–Fe phase diagram from CHART *et al.* [1979]. Lower diagram is experimental; upper diagram is calculated from binary data.

et al. [1979]). Such estimated phase diagrams are often quite acceptable for many purposes. However, the agreement between the experimental and calculated diagrams can usually be greatly improved by the inclusion of one or more "ternary terms" with adjustable coefficients in the equations for g^E. For example, the ternary term $aX_AX_BX_C$, which is zero in all three binary subsystem could be added to eq. (48) and the value of the parameter a which gives the best optimized fit to measured ternary phase diagram points could be determined. This, of course, requires that ternary measurements be made, but only a very few experimental points will usually suffice rather than the large number of measurements required for a fully experimental determination. In this way, the coupling of the thermodynamic approach with a few well chosen experimental measurements can greatly reduce the experimental effort involved in determining multicomponent phase diagrams.

An example of a coupled thermodynamic/phase diagram evaluation and calculation for a multicomponent system is the work of LEE and LEE [1992] on the Fe–Cr–V–C

system. The diagrams in figs 29, 30 were calculated thermodynamically by these authors. For the solid alloy and carbide phases, interstitial sublattice models were used. For the liquid phase, a substitutional model was employed. All available phase diagram and thermodynamic data for the binary and ternary subsystems, as well as for the quaternary system, were simultaneously optimized in order to obtain the best sets of binary and ternary parameters of the model equations for g^E for each phase as well as optimized equations for the standard Gibbs energies of the compounds. In this way, all the diverse data sets were smoothed and made consistent with each other and with thermodynamic principles. Any desired type of two-dimensional phase diagram section for the quaternary system can be calculated from the database of model parameters.

6. *Phase diagrams with potentials as axes*

So far we have considered mainly isobaric temperature–composition phase diagrams. However, there are many other kinds of phase diagrams of metallurgical interest with pressure, chemical potentials, volume, etc. as axes. These can be classified into geometrical types according to their topological rules of construction.

For instance, binary isothermal P–X diagrams as in fig. 20 are members of the same type as binary isobaric T–X diagrams since they are both formed from the same topological units of construction. Other useful phase diagrams of this same geometrical type are isothermal chemical potential–composition diagrams for ternary systems. An example is shown in the lowest panel of fig. 32 (PELTON and THOMPSON [1975]) for the Co–Ni–O system at T = 1600 K (and at a constant total hydrostatic pressure of 1 atm). Here the logarithm of the equilibrium partial pressure of O_2 is plotted versus the metal ratio $\xi = n_{Ni}/(n_{CO} + n_{Ni})$, where n_i = number of moles of i. There are two phases in this system under these conditions, a solid alloy solution stable at lower p_{O_2}, and a solid solution of CoO and NiO stable at higher p_{O_2}. For instance, point **a** gives p_{O_2} for the equilibrium between pure Co and pure CoO at 1600 K. Between the two single-phase regions is a two-phase (alloy + oxide) region. At any overall composition on the tie-line **cd** between points **c** and **d**, two phases will be observed, an alloy of composition **d** and an oxide of composition **c**. The lever rule applies just as for binary T–X diagrams.

The usual isothermal section of the ternary Co–Ni–O system at 1600 K is shown in the top panel of fig. 32. There are two single-phase regions with a two-phase region between them. The single-phase areas are very narrow since oxygen is only very slightly soluble in the solid alloy and since CoO and NiO are very stoichiometric oxides. In the central panel of fig. 32 this same diagram is shown but with the composition triangle "opened out" by putting the oxygen corner at infinity. This can be done if the vertical axis becomes $\eta = n_O/(n_{Co} + n_{Ni})$ with the horizontal axis as $\xi = n_{Ni}/(n_{Co} + n_{Ni})$. These are known as *Jänecke coordinates*. It can be seen in fig. 32 that each tie-line, **ef**, of the isothermal section corresponds to a tie-line, **cd** of the log diagram. This underscores the fact that every tie-line of a ternary isothermal section corresponds to a constant chemical potential of each of the components.

Another example of a log diagram is shown for the Fe–Cr–O system at 1573

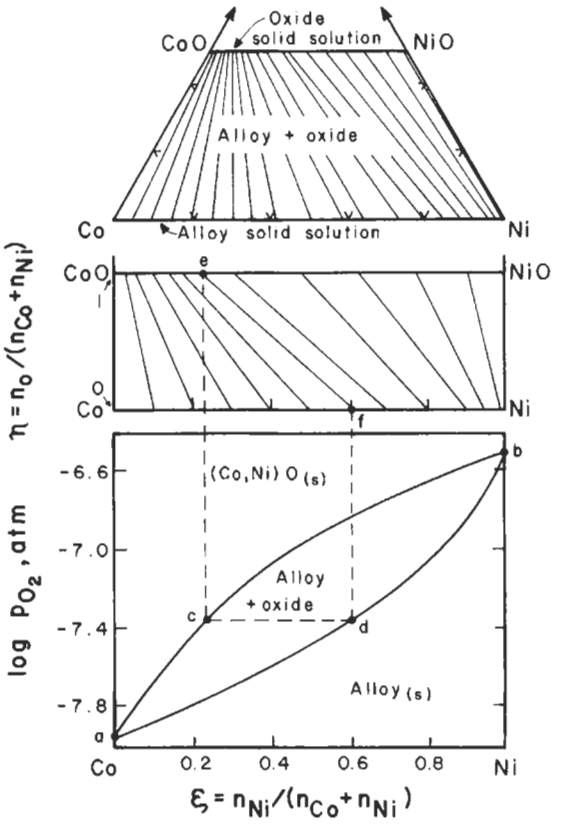

Fig. 32. Corresponding type-2 and type-3 phase diagrams for the Co–Ni–O system at 1600 K (from PELTON and THOMPSON [1975]).

K in the lower panel of fig. 33 (PELTON and SCHMALZRIED [1973]). The corresponding ternary isothermal section in Jänecke coordinates is shown in the upper panel. Each of the invariant three-phase tie-triangles in the isothermal section corresponds to an invariant line in the log p_{O_2}-ξ diagram. For example, the (spinel + (Fe, Cr)O + alloy) triangle with corners at points **a**, **b** and **c** corresponds to the "eutectic-like" invariant with the same phase compositions **a**, **b** and **c** at log $p_{O_2} \approx -10.7$. We can see that within a three-phase tie-triangle, p_{O_2} is constant.

An example of yet another kind of phase diagram of this same geometrical type is shown in fig. 34. For the quaternary Fe–Cr–O–SO_2 system at T = 1273 K and at constant $p_{SO_2} = 10^{-7}$ atm, fig. 34 is a plot of log p_{O_2} versus the molar metal ratio ξ (PELTON [1991]). Since log p_{O_2} varies as $-1/2$ log p_{S_2} when p_{SO_2} and T are constant, fig. 34 is also a plot of log p_{S_2} versus ξ.

It can be seen that the diagrams discussed above are of the same geometrical type as binary T–X diagrams since they are all composed of the same topological units of

References: p. 531.

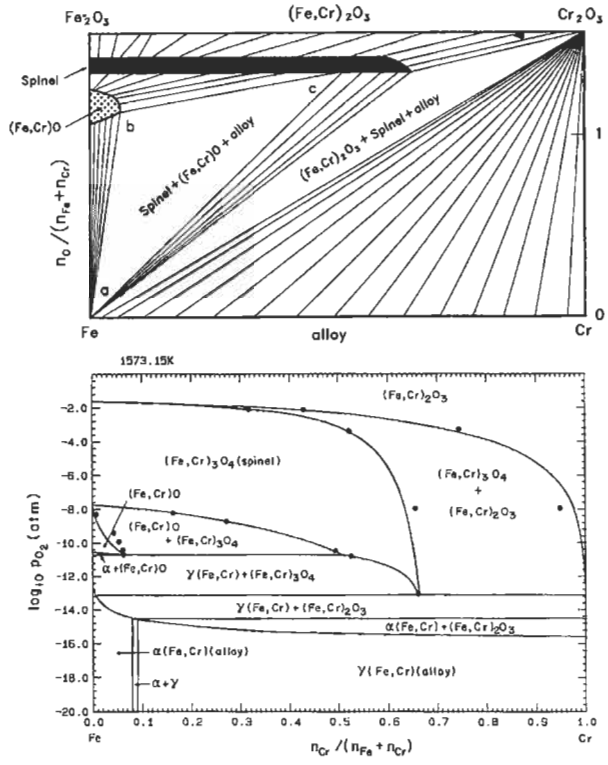

Fig. 33. Corresponding type-2 and type-3 phase diagrams for the Fe–Cr–O system at 1573 K (PELTON and SCHMALZRIED [1973]). Experimental points from KATSURA and MUAN [1964].

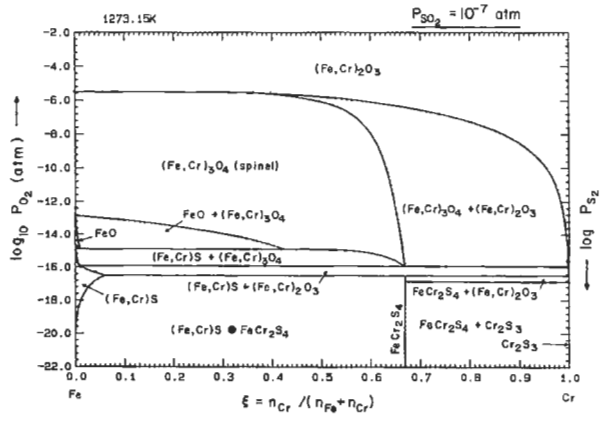

Fig. 34. Calculated type-2 phase diagram of log p_{O_2} versus molar metal ratio at T = 1273 K and $p_{SO_2} = 10^{-7}$ atm for the Fe–Cr–O–SO_2 system (PELTON [1991]).

construction as in fig. 15. Their interpretation is thus immediately clear to anyone familiar with binary T–X diagrams. Chemical potential–composition diagrams (figs. 32–34) are useful in the study of high temperature oxidation of alloys, metallurgical roasting processes, etc.

The log p_{O_2}-ξ diagrams in figs. 33, 34 were calculated by the same algorithm which produced the binary phase diagram of fig. 17. This algorithm operates by computing common tangent lines to the Gibbs energy–composition curves of the phases. The diagrams in figs. 33, 34 were calculated from optimized mathematical expressions for the Gibbs energy curves of all the phases. With these same optimized equations, $\log p_{O_2}$-ξ diagrams at other temperatures can be calculated, as can T–ξ diagrams at constant p_{O_2} which are also of the same geometrical type. For details see PELTON *et al.* [1979].

Another important geometrical type of phase diagram is exemplified by P–T phase diagrams for one-component systems as shown for H_2O in fig. 35. In such diagrams, which are discussed in ch. 5, § 3, bivariant single-phase regions are indicated by areas, univariant two-phase regions by lines, and invariant three-phase regions by *triple points.* An important rule of construction is the *extension rule* which is illustrated by the dashed lines in fig. 35. At a triple point, the extension of any two-phase line must pass into the single-phase region of the third phase.

Another kind of phase diagram of the same geometrical type is shown in fig. 36. For the Fe–S–O system at T = 800 K, the axes of the diagram are the equilibrium partial pressures of S_2 and O_2. Single-phase areas indicate which pure compounds of Fe are stable under the given conditions. Two-phase regions are lines. Three phases can co-exist only at triple points. The extension rule given above applies at all triple points. Such *stability diagrams* or *predominance diagrams* are useful in the study of oxidation, corrosion, roasting, etc. They have been treated in ch. 5, § 6.2 and have been discussed by KELLOGG and BASU [1960], INGRAHAM and KELLOGG [1963], PELTON and THOMPSON [1975], BALE *et al.* [1986] and BALE [1990]. They lend themselves to rapid computer calculation by Gibbs energy minimization from thermodynamic data stored in computerized data banks (BALE *et al.* [1986], BALE [1990]). Their usefulness is by no means restricted to metal–sulphur–oxygen systems or to systems of three components.

As another example of this same geometrical type of diagram, a plot of $RT \ln p_{O_2}$

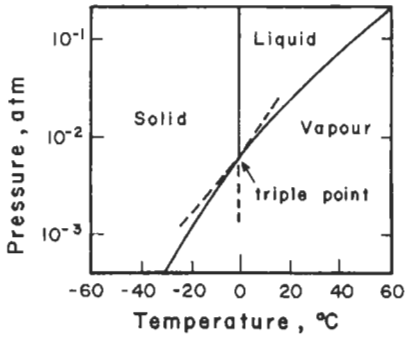

Fig. 35. Type-1 *P–T* phase diagram of H_2O.

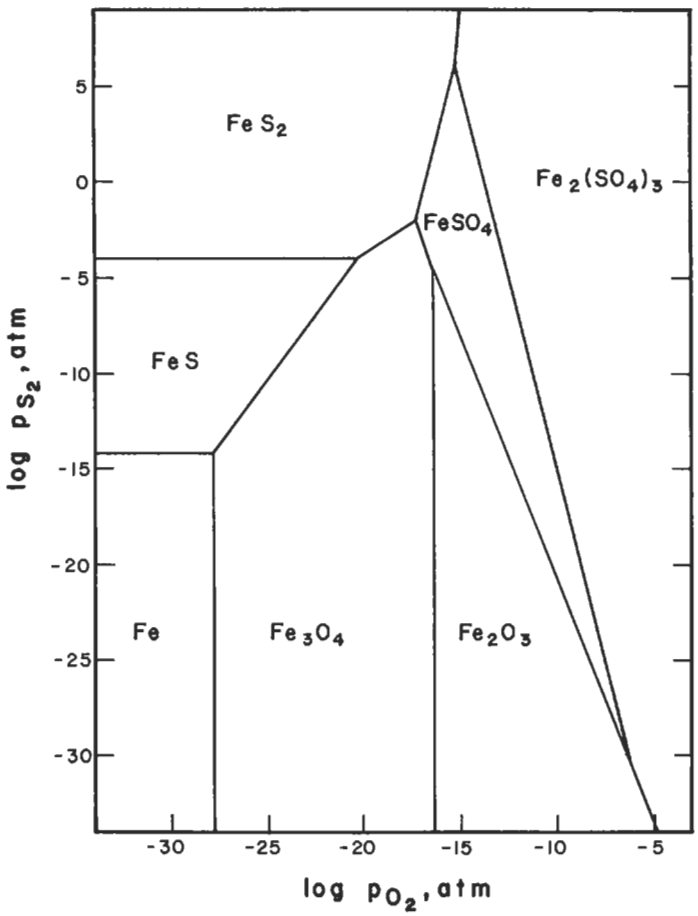

Fig. 36. Type-1 predominance diagram for Fe–S–O at 800 K.

versus T for the Fe–O system is shown in fig. 37b. Again, one-, two-, and three-phase regions are indicated by areas, lines and triple points respectively. In fig. 37a is the binary T-composition phase diagram for the Fe–O system. The correspondence between figs 37a and 37b is evident. Each two-phase line of fig. 37b "opens up" to a two-phase region of fig. 37a. Each tie-line of a two-phase region in fig. 37a can thus be seen to correspond to a constant p_{O_2}. Triple points in fig. 37b become horizontal invariant lines in fig. 37a.

Yet another type of phase diagram is shown in fig. 38. This is an isothermal section at constant molar metal ratio $n_{Cr}/(n_{Fe}+n_{Cr})=0.21$ for the Fe–Cr–S–O system. This diagram was calculated thermodynamically from model parameters (LAPLANTE [1993]). The axes are the equilibrium sulfur and oxygen partial pressures. Three or four boundary lines can meet at an intersection point. Some of the boundary lines on fig. 38 separate a two-phase region ($\alpha+\beta$)

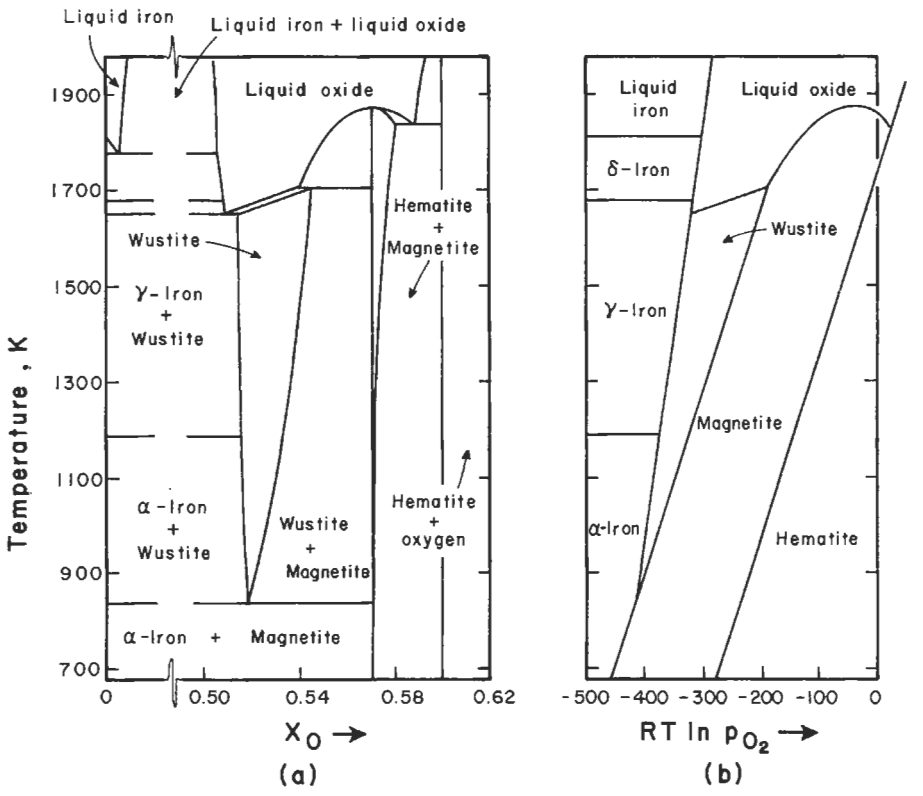

Fig. 37. Corresponding type-1 and type-2 phase diagrams for the Fe–O system (after MUAN and OSBORN [1965]).

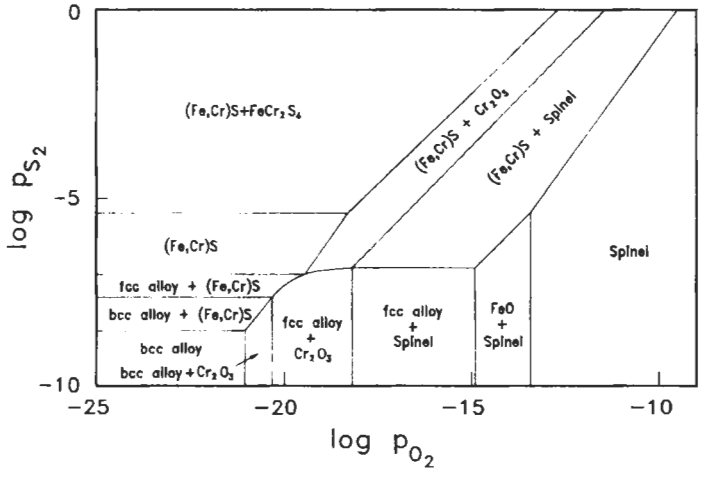

Fig. 38. Phase diagram of log p_{S_2} versus log p_{O_2} at 1273 K and constant molar metal ratio $n_{Cr}/(n_{Fe}+n_{Cr})=0.21$ in the Fe–Cr–S–O system (LAPLANTE [1993]).

References: p. 531.

from another two-phase region ($\alpha + \gamma$). These lines thus represent the conditions for three-phase ($\alpha + \beta + \gamma$) equilibrium. The Law of Adjoining Phase Regions (§ 3.5) applies to fig. 38 if these 3-phase lines are considered as degenerate infinitely narrow phase fields.

6.1. Classification of phase diagrams

In a system of C components we can define (C+2) *thermodynamic potentials*, ϕ_i. These are T, P, μ_1, μ_2, ..., μ_c (where μ_j is the chemical potential of component j). For each potential ϕ_i we can define a "*corresponding*" *extensive variable* q_i. For the potentials T, P and μ_j the corresponding extensive variables are S, V and n_j (entropy, volume and moles of component j). When two phases, α and β, are in equilibrium, $\phi_i^\alpha = \phi_i^\beta$ for all i.

If we choose any three potentials, designated ϕ_1, ϕ_2 and ϕ_3, and if we hold ϕ_4, ϕ_5, ..., ϕ_{c+2} constant, then a plot of ϕ_1 versus ϕ_2 will have the geometry of figs. 35, 36. Such diagrams were termed *type-1 phase diagrams* by PELTON and SCHMALZRIED [1973]. A general type-1 diagram is shown in fig. 39b. On a type-1 diagram the lines give the conditions for two-phase equilibrium, and the triple points are three-phase points.

If we now replace the ϕ_2 axis of the type-1 diagram by the ratio q_2/q_3 (or equivalently, by $q_2/(q_2+q_3)$), then we obtain a "*corresponding*" *type-2 phase diagram* as illustrated in fig. 39a. A corresponding type-2 diagram is also obtained by replacing ϕ_1 by q_1/q_3 as in fig. 39d. Two-phase lines in the type-1 diagram become two-phase regions with tie-lines in the corresponding type-2 diagrams. Triple points become invariant lines.

Consider the binary Fe–O system in fig. 37. Let $\phi_1 = T$, $\phi_2 = \mu_O$, $\phi_3 = \mu_{Fe}$, $\phi_4 = P$. Fig.

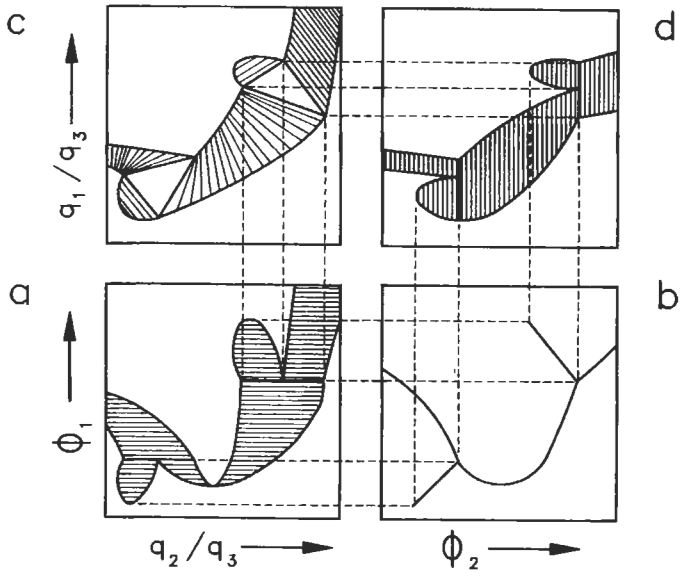

Fig. 39. Schematic representation of the three types of phase diagrams illustrating the general topology of (a) ϕ_1 *vs.* q_2/q_3, (b) ϕ_1 *vs.* ϕ_2, (c) q_1/q_3 *vs.* q_2/q_3, and (d) ϕ_2 *vs.* q_1/q_3, plots. (ϕ_4, ϕ_5, ... are kept constant).

37b is a type-1 diagram of ϕ_1 versus ϕ_2 with ϕ_4 constant. Fig. 37a is the corresponding type-2 diagram obtained by replacing ϕ_2 by the ratio $q_2/(q_2+q_3)=n_O/(n_O+n_{Fe})$.

Figs 20, 32 (lower panel), 33 (lower panel) and 34 are also type-2 diagrams. Type-2 diagrams are exemplified by binary isobaric T-composition diagrams. Consider the Fe–Cr–O system in fig. 33. Let $\phi_1=\mu_O$, $\phi_2=\mu_{Cr}$, $\phi_3=\mu_{Fe}$, $\phi_4=T$, $\phi_5=P$. the lower panel in fig. 33 is a type-2 diagram of ϕ_1 versus $q_2/(q_2+q_3)$ at constant ϕ_4 and ϕ_5. In the Fe–Cr–O–SO_2 system in fig. 34 there is one more component and therefore, one more potential, $\phi_6=\phi_{SO_2}$. By also holding this potential constant, we obtain the type-2 diagram of fig. 34.

If, as well as replacing ϕ_2 in a type-1 diagram by q_2/q_3, we also replace ϕ_1 by q_1/q_3, then a *corresponding type-3 phase diagram* results as shown in fig. 39c. In this diagram, triple points have become tie-triangles. Type-3 diagrams are exemplified by isothermal isobaric sections of ternary systems as in figs. 25, 27 and 31. The upper panel of fig. 33 shows the type-3 diagram corresponding to the type-2 diagram in the lower panel. The potential $\phi_1=\mu_O$ has been replaced by $q_1/(q_2+q_3)=n_O/(n_{Fe}+n_{Cr})$. This gives the type-3 diagram in Jänecke coordinates. This is usually transformed to the more usual Gibbs triangle representation as illustrated in fig. 32.

For a more detailed discussion of this classification scheme, see PELTON and SCHMALZRIED [1973] and PELTON and THOMPSON [1975].

Type-1, -2, and -3 phase diagrams are all sections at constant potentials (ϕ_4, ϕ_5, ... ϕ_{c+2}). Hence, all tie-lines lie in the plane of the diagram. When sections are taken at constant composition, then different geometries result. Fig. 38 is an example of a constant composition section in which both axes are potentials. Figs 28 and 29 are constant composition sections in which one axis is a potential, T, while the other axis is a composition variable. In fig. 30, both axes are composition variables. The geometrical rules of construction of these diagrams have already been discussed (§ 3.5, § 4). The difference among them is that fig. 30 contains no degenerate phase fields, while in fig. 38 lines can be degenerate phase fields, and in figs. 28 and 29 only horizontal lines can be degenerate phase fields.

For more detailed discussions of the classification of phase diagrams, including projections and diagrams with more than two dimensions, see PALATNIK and LANDAU [1964], PRINCE [1963] and HILLERT [1985].

As a final note on the topology of phase diagrams, the construction of multicomponent constant–composition sections by means of zero phase fraction (ZPF) lines was discussed in § 4.1 and illustrated by fig. 30. It should be noted that this method applies to any two-dimensional phase diagram section and can be used to construct any phase diagram in the present article (with the exception of the projections in figs. 23, 24 and 27). When one or both axes are potentials, then parts of the ZPF lines for two phases may be coincident.

7. *Experimental techniques of measuring phase diagrams*

It is beyond the scope of the present article to give a complete discussion of experimental techniques. Only a brief survey of the major techniques will be presented

with a view to providing the reader with some insight into the difficulties involved. More detailed discussions are given by RAYNOR [1970], MACCHESNEY and ROSENBERG [1970], BUCKLEY [1970], and HUME–ROTHERY *et al.* [1952].

As has been discussed in § 5, modern techniques of computer coupling of thermodynamics and phase diagrams can significantly reduce the amount of experimental effort required to characterize a phase diagram completely, particularly in the case of multicomponent systems.

7.1. Thermal analysis

Liquidus temperatures are commonly determined by the measurement of *cooling curves*. Consider the binary alloy A–B of composition 1 in fig. 40. A sample of liquid alloy, of the order of 50 g, is held in a crucible in a furnace. The furnace temperature is then decreased slowly at a uniform rate, usually not exceeding 1°C per minute, while the temperature of the alloy is measured by a calibrated recording thermocouple. A graph of sample temperature versus time (the *cooling curve*) is shown in fig. 41a. At the liquidus temperature (point **a** in fig. 40), solidification commences with the evolution of heat. This causes a decrease in the cooling rate of the specimen with, ideally, a resultant abrupt change of slope of the curve as shown in fig. 41a. When solidification is complete at the solidus composition (point **b** in fig. 40), heat evolution ceases and, ideally, another change of slope of the cooling curve is observed. From the "idealized" cooling curve of fig. 41a, one can then read the liquidus and solidus temperatures. For an alloy of composition 2, the idealized cooling curve is shown in fig. 41b. There is a change of

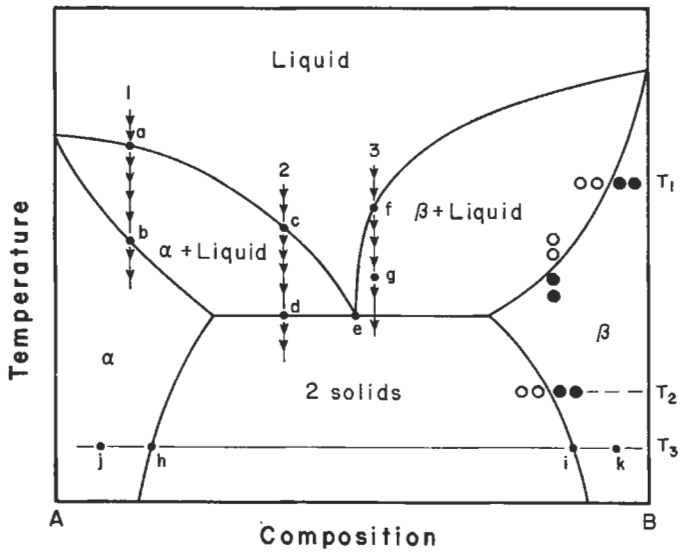

Fig. 40. Binary phase diagram to illustrate some experimental techniques; solid circles: single-phase alloy, open circles: two-phase alloy.

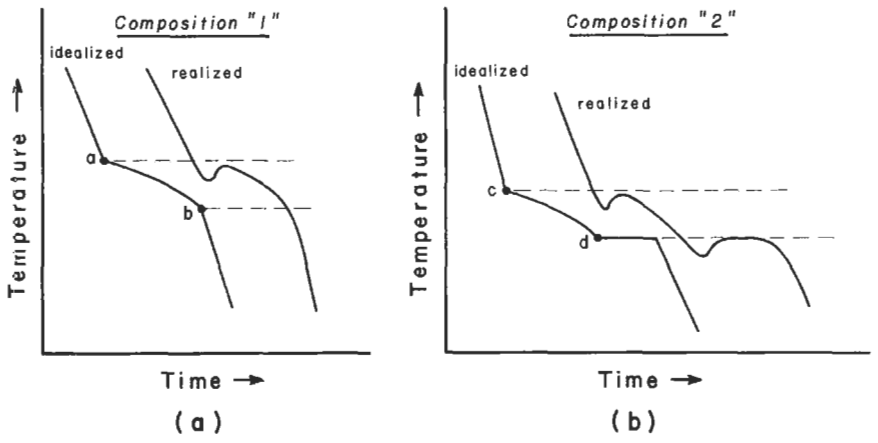

Fig. 42. Cooling curves for alloys of compositions 1 and 2 of fig. 40.

slope at the liquidus, and a plateau at the eutectic temperature since, ideally, the sample temperature remains constant until the invariant eutectic solidification reaction is complete.

In a real experiment, however, cooling curves of the type labelled "realized" in fig. 41 are usually obtained. Some degree of undercooling (or *supercooling*) is almost always observed. The sample must be cooled below the transformation temperature before nucleation of the new phase occurs. The temperature then rises again. However, at a liquidus the temperature will never rise all the way back up to the liquidus, so that some extrapolation technique must be used to estimate the liquidus temperature. At a eutectic, the equilibrium eutectic temperature may be regained by the sample after supercooling provided that the quantity of material solidifying eutectically is large enough to yield a sufficient evolution of heat. Supercooling may be minimized by stirring or by constantly jolting the sample to induce nucleation.

It is important that temperature gradients within the sample be eliminated by stirring and by the use of a furnace with a good constant temperature zone. Otherwise, part of the sample will start to solidify before the rest and the cooling curve will show a rounded rather than an abrupt change of slope.

At compositions where the liquidus is steep, such as the composition 3 in fig. 40, the rate of heat evolution is small. That is, on descending from the liquidus at point **f** to a point **g** an appreciable distance below the liquidus, only a small amount of heat is evolved since, as can be seen from the lever rule, only a small amount of solid is precipitated. Hence, it is more difficult to determine the exact temperature of the change in slope of the cooling curve, and the technique of thermal analysis is less precise. For very steep liquidus lines, a method of segregation and sampling or quenching may be preferable, as will be discussed below.

For liquidus temperatures below about 1000°C, absolute accuracies of the order of ± 1°C can be obtained by cooling curve methods under optimal conditions. For temperat-

ures of the order of 100°C or lower, accuracies of ±0.25°C may be obtained.

In principle, solidus temperatures can be determined by the method of cooling curves as shown for the idealized curve in fig. 41a. In certain very favourable cases, with very slow cooling rates, this may be possible. However, in most cases a curve such as the "realized" curve of fig. 41a will be observed, in which determination of the solidus temperature is extremely imprecise. The reasons for this are, firstly, that the solid phase will contain concentration gradients so that solidification will not be complete at the equilibrium solidus temperature; secondly, that the precipitated solid phase will insulate the thermocouple from the sample thereby reducing sensitivity; and thirdly, that by the time the solidus temperature is approached the sample temperature will have lagged well behind the furnace temperature so that the cooling rate will start to accelerate rapidly. For these reasons, solidus temperatures are better measured by *heating curves* which are, in most respects, analogous to cooling curves. An important precaution here is to ensure, by means of a long anneal, that the solid sample is homogeneous before commencing the experiment. In general, it is more difficult to measure solidus temperatures with accuracy than it is to measure liquidus temperatures.

In principle, a peritectic invariant can also be evidenced by a plateau on a cooling curve. However, as discussed in § 2.5.3, peritectic reactions are frequently greatly retarded kinetically so that only a weak short thermal arrest may actually be observed.

In general, the precision of thermal analysis experiments may be increased by the use of Differential Thermal Analysis (DTA) in which two thermocouples, connected in opposition, are placed, respectively, in the sample and in a standard specimen which undergoes no phase transformation in the temperature range of study. The danger in DTA experiments is that, because of the large surface to volume ratio of the small samples used, specimen temperatures often do not increase sufficiently after supercooling.

7.2. Sampling techniques and quenching techniques

As discussed above, thermal analysis may be inaccurate for determining the position of a steep liquidus. In such a case, a segregation and sampling technique may prove best. Suppose an alloy of overall composition and temperature in the (liquid + solid) region at point **g** in fig. 40 is held at temperature until equilibrium is established. A specimen of the liquid phase is then obtained, perhaps by suction in a ceramic tube. Chemical analysis will then give the composition of the liquidus at this temperature. A similar technique might be used to measure the compositions of the boundaries of a liquid–liquid miscibility gap. Clearly these methods depend for accuracy on a clean separation of the phases and on the prevention of oxidation and of volatilization losses while the sampling device is inserted into the container.

The principle of *quenching techniques* for solidus determinations is illustrated at temperature T_1 in fig. 40. Samples at each of the four overall compositions shown at T_1 are held at temperature long enough for equilibrium to be attained. They are then quenched rapidly. When examined microscopically, samples from the two-phase zone will exhibit regions of rapidly quenched liquid which can be distinguished from the solid grains. In this way the solidus composition can be bracketed. Alternatively, one could

quench samples of the same composition annealed at different temperatures, thereby bracketing the solidus temperature as is also illustrated in fig. 40.

Because of the slowness of solid state reactions, thermal analysis is rarely a useful technique for locating phase boundaries involving two solid phases. However, in such cases annealing and quenching followed by microscopic observation to determine whether one or two phases are present can often be used to bracket the phase boundary as illustrated for the solvus line in fig. 40 at T_2.

Another method of determining phase boundaries in the solid state involves the annealing of a sample in a two-phase (solid_1 + solid_2) region followed by quenching and subsequent quantitative analysis by any of several techniques to determine the compositions of the two phases present. The relevant techniques of quantitative metallography are discussed in ch. 10, § 7, where several examples are quoted of the use of such techniques to determine solid solubility limits.

In all techniques involving quenching, it is essential that the quench be as rapid as possible so as to avoid any diffusion, segregation or reaction during cooling.

7.3. Other techniques

Suppose that one wishes to determine the compositions (points **h** and **i**) of the phase boundaries at T_3 in fig. 40. Samples at a number of compositions at T_3 between points **j** and **k** are annealed and quenched. The lattice spacings of the α and β phases are then measured by X-ray techniques. The lattice spacings, when plotted versus composition, vary continuously in the single-phase regions, but remain constant in the two-phase region. Extrapolation of the single-phase and two-phase portions of the lattice spacing versus composition curve to their point of intersection then gives the composition of the phase boundary. If too much decomposition occurs upon quenching, then high-temperature X-ray techniques may be required to perform the measurements at temperature.

A technique which is similar in principle consists in measuring the electrical conductivity of specimens at various compositions at T_3 along the line between points **j** and **k**. Again, sharp breaks in the plot of conductivity versus composition are noted at the phase boundaries. This technique is often quite rapid, and can be carried out at elevated temperatures without the necessity of quenching.

In the interdiffusion technique, polished pellets of compositions **j** and **k** are clamped together and annealed at T_3. Following quenching, a composition versus distance scan is performed across the specimen by, say, microprobe analysis. A sharp discontinuity in the curve is observed at the interface, the compositions at either side being the phase boundary compositions **h** and **i**. This technique can also often be used to indicate the presence and compositions of one or more intermediate phases in one single experiment (see for example, SCHMALZRIED [1974]).

A great many other techniques of phase diagram measurement exist, such as dilatometric (HUME–ROTHERY *et al.* [1952], SINHA *et al.* [1967]), hardness (BARREAU and CIZERON [1979]), and magnetic measurements (ch. 29, § 6, also SUCKSMITH [1939]). The complete determination of an alloy phase diagram usually requires a combination of several techniques (e.g., a combination of dilatometry and magnetic measurements (SERVANT *et al.* [1973])).

References: p. 531.

8. *Bibliography*

8.1. Compilations of phase diagrams

The classic compilation in the field of binary alloy phase diagrams is that of HANSEN [1958]. This work was continued by ELLIOTT [1965] and SHUNK [1969]. These compilations contain critical commentaries. A non-critical compilation of binary alloy phase diagrams was prepared by MOFFAT [1978-1992]. HULTGREN *et al.* [1973] have critically evaluated the phase diagrams and thermodynamic properties of several binary alloy systems. An extensive non-critical compilation of binary and ternary phase diagrams of metallic systems has been edited by AGEEV [1959–1978]. An index to all compilations of binary alloy phase diagrams up to 1979 was prepared by MOFFAT [1979]. A critical compilation of binary phase diagrams involving Fe has been published by ORTRUD KUBASCHEWSKI [1982].

Ternary alloy phase diagrams were compiled by AGEEV [1959–1978] and by GUERTLER *et al.* [1969]. A bibliography of ternary and multicomponent metallic phase diagrams for the period 1955–1973 was published by PRINCE [1978]. VCH publishers (NY) are producing a series of volumes of compilations of ternary alloy phase diagrams known as "Ternary Alloys". Eight volumes, in alphabetical order, have already appeared.

Since 1979, the American Society for Metals in collaboration with the National Institute of Science and Technology and with national organizations in several countries, has undertaken a project whose goal is a complete critical evaluation of all binary and ternary alloy phase diagrams. All available literature on phase equilibria, crystal structures, and often on thermodynamic properties is cited and critically evaluated in great detail by "category editors" who are each responsible for a group of systems. Evaluations of important systems usually run to several pages. The evaluations are peer reviewed and the majority are published in the *Journal of Phase Equilibria*, (formerly the *Bulletin of Alloy Phase Diagrams*) (ASM International, Materials Park, Ohio). More than 2500 binary evaluations have been completed. Condensed versions of approximately 2800 evaluations have been published in three volumes (MASSALSKI *et al.* [1990]). When a "category" of evaluations (e.g. all binary phase diagrams with Cu) is completed, a monograph is published as part of the ASM Monograph Series.

An extensive bibliography of binary and multicomponent phase diagrams of all types of systems (metallic, ceramic, aqueous, organic, etc.) has been compiled by WISNIAK [1981]. A bibliographical database known as THERMDOC on thermodynamic properties and phase diagrams of systems of interest to materials scientists, with monthly updates, is available through Thermodata (Domaine Universitaire, Saint-Martin d'Hères, France).

8.2. Texts and review articles

A large number of texts and review articles covering all aspects of the theory, measurement and applications of phase diagrams are available. Only a selected few are listed here. A classical discussion of phase diagrams in metallurgy was given by RHINES [1956]. A definitive text on the theory of phase diagrams is that of PALATNIK and LAUDAU [1964]. Treatments of the geometry of multicomponent phase diagrams are

given by PRINCE [1963], PRINCE [1966] and HULTGREN [1985]. Good discussions of the interpretation of binary and ternary diagrams are given by WEST [1965] and BERGERON and RISBUD [1984]. A series of five volumes edited by ALPER [1970–1978] discusses many aspects of the theory, interpretation, measurement and applications of phase diagrams in materials science.

9. *Acknowledgements*

Thanks are due to Mr. Jacques Desrochers for the task of preparing the drawings and to Mrs. Johanne Gaulin for her help with the manuscript.

References

AGEEV, N. V., ed., 1959–1978, Phase Diagrams of Metallic Systems, vol. 1–22 (Academy of Sciences of USSR, Moscow).

ALABYSHEV, A. F. and A. G. MORACHEVSKII, 1957, Z. Neorg. Khim. **2**, 669.

ALPER, A. M., ed., 1970–1978, Phase Diagrams – Materials Science and Technology, vol. 1–5 (Academic, New York).

ASHTAKALA, S., C. W. BALE and A. D. PELTON, 1981, Bull. Alloy Phase Diagrams **2**, 83.

BALE, C. W., 1990, Canad. Metall. Quart. **29**, 263.

BALE, C. W., and A. D. PELTON, 1983, Metallurg. Trans., **14B**, 77.

BALE, C. W., A. D. PELTON and W. T. THOMPSON, 1986, Canad. Metall. Quart. **25**, 107.

BARIN, I., O. KNACKE and O. KUBASCHEWSKI, 1977, Thermochemical Properties of Inorganic Substances (Springer–Verlag, Berlin).

BARREAU, O., and G. CIZERON, 1979, Mém. Sci. Rev. Mét. **76**, 729.

BARTLETT, H. E., A. J. NEETHLING and P. CROWTHER, 1970, J. Chem. Thermo. **2**, 523.

BERGERON, C. J. and S. H. RISBUD, 1984, Introduction to Phase Equilibria in Ceramics (Amer. Ceramic Soc., Columbus, Ohio).

BRAY, H. J., F. D. BELL and S. J. HARRIS, 1961–62, J. Inst. Metals **90**, 24.

BUCKLEY, R. A., 1970, in: Techniques of Metals Research, ed. R. A. Rapp (Interscience, New York) vol. IV, part I.

CHART, T., F. PUTLAND and A. DINSDALE, 1979, in: Proc. Calphad VIII Conference, Stockholm, 1979, eds. B. Uhrenius and M. Hillert (Royal Institute of Technology, Stockholm) p. 183.

CHASE, M. W., 1983, Bull. Alloy Phase Diag. **4**, 124.

DINSDALE, A. T., 1991, Calphad J. **15**, 317.

DÖRNER, P., E.-Th. HENIG, H. KRIEG, H. L. LUCAS and G. PETZOW, 1980, Calphad J. **4**, 241.

ELLIOTT, R. P., 1965, Constitution of Binary Alloys, First Supplement (McGraw–Hill, New York).

FOWLER, R. H. and E. A. GUGGENHEIM, 1939, Statistical Thermodynamics, pp 350–366 (Cambridge Univ. Press, Cambridge, U.K.).

GUERTLER, W., M. GUERTLER and E. ANASTASIADIAS, 1969, A Compendium of Constitutional Ternary Diagrams of Metallic Systems, WADC Technical Report 58–615 (Parts I, II, III) U.S. Dept. of Commerce, Springfield, VA).

GUGGENHEIM, E. A., 1935, Proc. Roy. Soc. **A148**, 304.

GUPTA, H., J. E. MORRAL and H. NOWOTNY, 1986, Scripta Metall. **20**, 889.

HANSEN, M., 1958, Constitution of Binary Alloys, 2nd Ed. (McGraw–Hill, New York; 1st Ed.: Springer, Berlin, 1936).

HAUFFE, K., 1940, Z. Elektrochem. **46**, 348.

HENSEL, F., 1979, Adv. Phys. **28**, 555.

HILLERT, M., 1980, Calphad J. **4**, 1.
HILLERT, M., 1985, Int. Metall. Rev. **30**, 45.
HILLERT, M., and M. JARL, 1978, Calphad J. **2**, 227.
HILLERT, M., B. JANSSON, B. SUNDMAN and J. AGREN, 1985, Metall. Trans. **16A**, 261.
HULTGREN, R., R.L. ORR, P.D. ANDERSON and K.K. KELLY, 1963, Selected Values of Thermodynamic Properties of Metals and Alloys (Wiley, New York).
HULTGREN, R., P.D. DESAI, D.T. HAWKINS, M. GLEISER, K.K. KELLY and D.D. WAGMAN, 1973, Selected Values of the Thermodynamic Properties of the Elements and Binary Alloys, vol. 1, 2 (ASM, Metals Park, OH).
HUME–ROTHERY, W., J.W. CHRISTIAN and W.B. PEARSON, 1952, Metallurgical Equilibrium Diagrams (Inst. of Physics, London).
INDEN, G, 1982, Bull. Alloy Phase Diagrams **2**, 412.
INGRAHAM, T.R. and H.H. KELLOGG, 1963, TMS-AIME **227**, 1419.
KATSURA, T. and A. MUAN, 1964, TMS-AIME **230**, 77.
KAUFMAN, L., and H. BERNSTEIN, 1970, Computer Calculation of Phase Diagrams (Academic, New York).
KELLOGG, H.H. and S.K. BASU, 1960, TMS–AIME **218**, 70.
KLEINSTUBER, T., 1961, Ph.D. Thesis, Univ. Munich, Germany.
KOHLER, F., 1960, Monatsh. Chemie **91**, 738.
KÖSTER, W., and W. DULLENKOPF, 1936, Z. Metallk. **28**, 309.
KUBASCHEWSKI, O., 1982, Iron Binary Phase Diagrams (Springer–Verlag, NY).
KURNAKOV, N.S. and A.N. KUSNETZOW, 1907, Z. Anorg. Chem. **52**, 173.
LANTRATOV, M.F. and A.G. MIKHAILOVA, 1971, Zh. Prikl. Khimii **44**, 1778.
LAPLANTE, S., 1993, Final year project, Ecole Polytechnique, Montreal.
LEE, B.J. and D.N. LEE, 1992, J. Phase Equilib. **13**, 349.
LEVIN, E.M., C.R. ROBBINS, H.F. MCMURDIE, R.S. ROTH, T. NEGAS, L.P. COOK, J.R. DENNIS, M.A. CLEVINGER and D. MCKENNA, 1964–1992, Phase Diagrams for Ceramists (and Supplements) (Am. Ceramic Soc., Columbus, Ohio).
LIPSON, H. and A.J.C. WILSON, 1940, J. Iron Steel Inst. **142**, 122.
LÜCK, R., U. GERLING and B. PREDEL, 1989, Z. Metallkunde **80**, 270.
LUKAS, H.L., E.-Th. HENIG and B. ZIMMERMANN, 1977, Calphad J. **1**, 225.
MACCHESNEY, J.B., and P.E. ROSENBERG, 1970, in: Phase Diagrams – Materials Science and Technology, ed. A.M. Alper (Academic, New York) vol. 1, ch. 3.
MAIOROVA, E.A., A.G. MORACHEVSKII and S.G. KOVALENKO, 1976, Elektrochimiya **12**, 313.
MASSALSKI, T.B., P.R. SUBRAMANIAN, H. OKAMOTO and L. KACPRZAK, 1990, Binary Alloy Phase Diagrams, 2nd ed., vol. 1, 2 and 3 (ASM International, Materials Park, Ohio).
MATHEWSON, C.H., 1906, Z. Anorg. Chem. **50**, 180.
MIODOWNIK, A.P., 1982, Bull. Alloy Phase Diagrams **2**, 406.
MOFFATT, W.G., 1979, The Index to Binary Phase Collections (General Electric, Schenectady, NY).
MOFFATT, W.G., 1978–1992, Handbook of Binary Phase Diagrams (and Supplements) (Genium Publishing Corp., Schenectady, NY).
MUAN, A., and F. OSBORN, 1965, Phase Equilibria Among Oxides in Steelmaking (AddisonWesley, Reading, MA).
PALATNIK, L.S. and A.I. LANDAU, 1964, Phase Equilibria in Multicomponent Systems (Holt, Rinehart and Winston, NY).
PELTON, A.D., 1988, Bull. Alloy Phase Diag. **9**, 41.
PELTON, A.D., 1991, Thermodynamics and Phase Diagrams of Materials, in: Materials Science and Technology, Vol. 5, Eds. R.W. Cahn, P. Haasen and E.J. Kramer (VCH, NY).
PELTON, A.D. and C.W. BALE, 1986, Metall. Trans. **17A**, 1057.
PELTON, A.D. and M. BLANDER, 1984, Proc. AIME Symp. on Molten Salts and Slags, 281 (The Metall. Soc., AIME, Warrendale, PA).
PELTON, A.D. and M. BLANDER, 1986, Metall. Trans. **17B**, 805.
PELTON, A.D. and M BLANDER, 1988, Calphad J. **12**, 97.
PELTON, A.D. and H. SCHMALZRIED, 1973, Metallurg. Trans. **4**, 1395.

PELTON, A. D., and W. T. THOMPSON, 1975, Prog. Solid State Chem. **10**, Part 3, 119.
PELTON, A. D., H. SCHMALZRIED and J. STICHER, 1979, J. Phys. Chem. Solids **40**, 1103.
PETRIC, A., A. D. PELTON and M.-L. SABOUNGI, 1988, J. Electrochem. Soc. **135**, 2754.
PITSCH, W. and G. INDEN, 1991, Atomic Ordering, in: Materials Science and Technology, Vol. 5, Eds. R. W. Cahn, P. Haasen and E. J. Kramer (VCH, NY).
PRINCE, A., 1963, Metall. Rev. **8**, 213.
PRINCE, A., 1966, Alloy Phase Equilibria (Elsevier, Amsterdam).
PRINCE, A., 1978, Multicomponent Alloy Constitution Bibliography 1955–73 (The Metals Society, London).
RAYNOR, G. V., 1970, Phase Diagrams and Their Determination, in: Physical Metallurgy, 2nd Ed., Ed. R. W. Cahn (North–Holland, Amsterdam) ch. 7.
RHINES, F. N., 1956, Phase Diagrams in Metallurgy (McGraw–Hill, New York).
ROOS, G. D., 1916, Z. Anorg. Chem. **94**, 329.
SABOUNGI, M.-L., S. J. HERRON and R. KUMAR, 1985, Ber. Bunsenges, Phys. Chem. **89**, 375.
SCHMALZRIED, H., 1974, Solid State Reactions (Academic, New York), ch. 7.
SCHREINEMAKERS, F. A. H., 1915, Proc. K. Akad. Wetenschappen, Amsterdam (Section of Sciences) **18**, 116.
SERVANT, C., O. CIZERON and P. LACOMBE, 1973, J. Iron Steel Inst. **211**, 75.
SHUNK, F. A., 1969, Constitution of Binary Alloys, Second Supplement (McGraw–Hill, New York).
SINHA, A. K., R. A. BUCKLEY and W. HUME–ROTHERY, 1967, J. Iron Steel Inst. (London) **205**, 191.
SPENCER, P. J., and I. BARIN, 1979, Mater. Eng. Appl., Sci and Tech. Press, Reigate, U.K. **1**, 167.
SUCKSMITH, W., 1939, Proc. Roy. Soc. [A] **170**, 551
VAN LAAR, J. J., 1908, Z. Phys. Chem. **63**, 216; **64**, 257.
WEEKS, J. R. and H. A. DAVIES, 1964, AEC Report, Conf. 660712–1, BNL–10372.
WEST, D. R. F., 1965, Ternary Equilibrium Diagrams (McMillan, New York).
WISNIAK, J., 1981, Phase Diagrams: A Literature Source Book, vol. 1 and 2 (Elsevier, NY).

CHAPTER 7

DIFFUSION IN METALS AND ALLOYS

J. L BOCQUET, G. BREBEC, Y. LIMOGE

Centre d'Etudes de Saclay
Département d'Etudes du Comportement des Matériaux
Section de Recherches de Métallurgie Physique
91191 Gif sur Yvette, Cedex, France

R. W. Cahn and P. Haasen†, eds.
Physical Metallurgy; fourth, revised and enhanced edition

1. Macroscopic and microscopic theories of diffusion

In this section we will present the macroscopic and microscopic theories of diffusion. The former provides a description of the observed phenomena (which are fluxes), starting from the formalism associated with the thermodynamics of irreversible processes; one then obtains a formal expression of these fluxes as a function of thermodynamic forces and of parameters which are called the *phenomenological coefficients*. In the latter approach the fluxes are calculated by starting from atomic mechanisms. The parameters used in this case are the jump frequencies; they have a clear physical meaning, as opposed to the phenomenological coefficients which are only coefficients of proportionality. This step encompasses two parts: on the one hand the random walk modelling which starts with atomic jump frequencies and builds the macroscopic diffusion coefficient, and on the other hand the jump theory which defines the jump frequencies themselves from the very properties of the system and its defects. For both formalisms, however, a knowledge of the underlying atomic mechanisms is required in order to describe the diffusion phenomena properly. Thus we begin with a short review of the possible mechanisms. Finally we present briefly the modern simulation tools, the use of which is steadily increasing in diffusion studies.

1.1. The mechanisms of diffusion

In crystalline solids, the atoms occupy well defined equilibrium positions (regardless of thermal vibrations); they move by jumping successively from an equilibrium site to another. The different possible mechanisms for dense structures are schematized in fig. 1.

1.1.1. Exchange mechanisms

In the *direct exchange mechanism* (fig. 1–1) two neighbouring atoms exchange their positions. This mechanism is unlikely for dense structures, for it would involve large distortions and would then entail too large activation energies.

In the *cyclic exchange mechanism* as proposed by ZENER [1951], N atoms exchange themselves simultaneously (in fig. 1–2, $N = 4$); the energy involved is much lower than in the direct exchange, but this mechanism remains unlikely, because of the constraint imposed by a collective motion.

At the present time there are no experimental supports for any such mechanisms in crystallized metals and alloys. In metallic liquids cooperative motions are more likely operating.

1.1.2. Mechanisms involving point defects

In thermal equilibrium a crystal always contains point defects. The best known are vacancies, divacancies and interstitials. The presence of these defects in the crystals will allow the atoms to move without too large lattice distortions. The properties of these point defects are described in ch. 18.

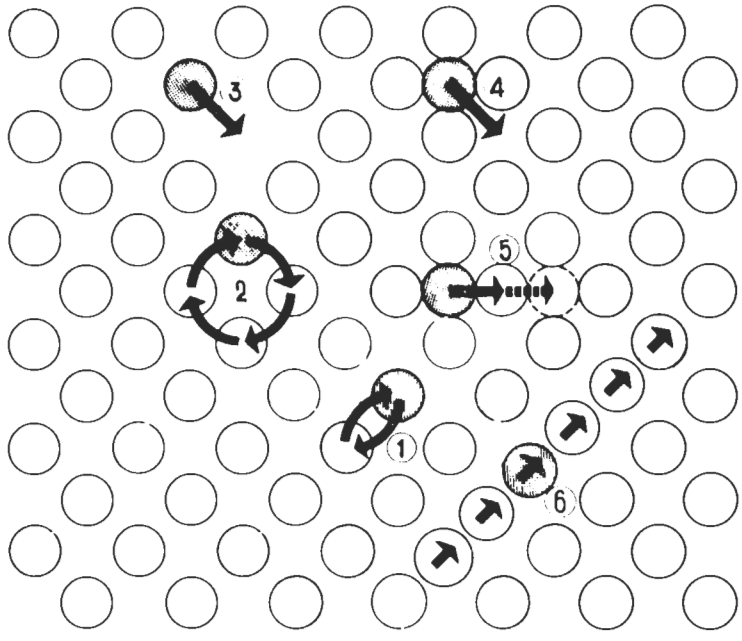

Fig. 1. Mechanisms of diffusion in crystals, after ADDA and PHILIBERT [1966]: (1) direct exchange, (2) cyclic exchange, (3) vacancy, (4) interstitial, (5) interstitialcy, (6) crowdion.

1.1.2.1. Interstitial mechanisms. In the *interstitial mechanism* (fig. 1–4) the atoms move from interstitial site to interstitial site. Usually small interstitial atoms, like hydrogen or carbon in metals, diffuse through the lattice by this mechanism.

The *interstitialcy* is somewhat more complex; as sketched in fig. 1–5, the atoms move from interstitial to substitutional site and vice versa. At higher temperatures, this mechanism contributes to silver diffusion in the silver halides. In metals and alloys with a dense structure the interstitial formation energy is so large that the concentration of these defects is completely negligible at thermal equilibrium. The situation is quite different when the material is out of equilibrium (for instance when it is plastically deformed or irradiated); under these conditions one can create *Frenkel pairs*, namely an equal number of vacancies and interstitials, which will both contribute to the diffusion. In metals and alloys the self-interstitial atom is not centered on the interstitial site: it has a dumbbell split configuration around a stable position. It is generally recognized that the self-interstitial is split along a <100> direction in fcc and along a <110> in bcc materials (SCHILLING [1978]; ch. 18, § 3.3.2.2). The case of the mixed dumbbell (one solute + one solvent) is not so simple (see for example LAM *et al.* [1983]). The elementary jumps for these split interstitials are shown in fig. 2. At low temperatures, under irradiation, the interstitial would have a *crowdion* configuration (SEEGER [1976]; fig. 1–6); at a higher temperature this crowdion would convert into a split interstitial.

References: p. 651.

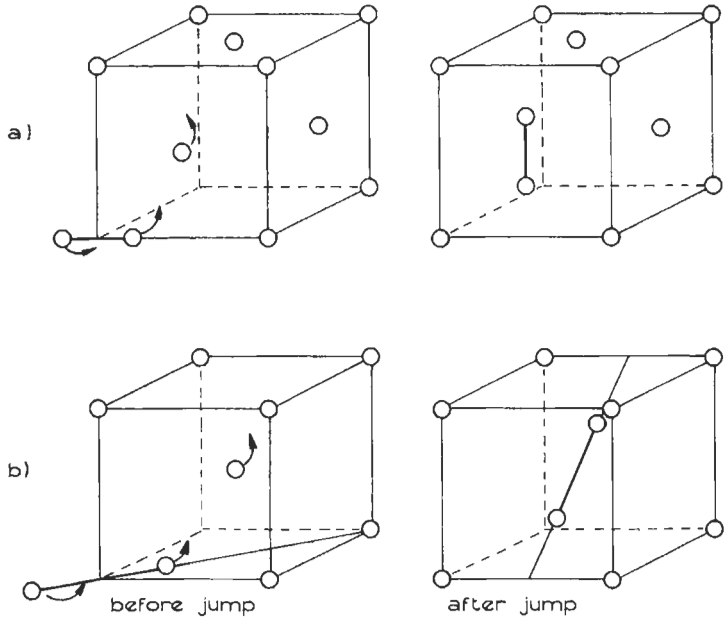

Fig. 2. Elementary jumps of the split interstitials (a) in fcc metals and (b) in bcc metals.

1.1.2.2. Vacancy mechanisms. In metals and alloys, near the melting point, the vacancy concentration is about 10^{-3} to 10^{-4} site fraction. These vacancies allow the atoms to move rather easily, and this mechanism is operating in most cases, with jumps to nearest neighbour sites (NN), or also to next nearest neighbour ones (NNN) in bcc crystals.

Besides monovacancies there are *vacancy aggregates*: divancancies, trivacancies, etc., which can contribute to the diffusion (ch. 18, § 2.2.2.1). The ratio divacancies/ monovacancies generally increases with temperature, so that the divacancy contribution to the diffusion also increases. We will see that numerous anomalies observed at high temperature (leading to curvature of the Arrhenius plot) are attributed to the divancancies. In dilute alloys there is often a binding energy between solutes and vacancies, and the resulting solute–vacancy pairs (complexes) also contribute to the diffusion. The *relaxation mechanism* which is a variant of the vacancy mechanism was proposed by NACHTRIEB and HANDLER [1954]. The underlying idea is that a large relaxation around a vacancy distorts its surroundings to such an extent that a liquid-like diffusion mechanism can take place; this idea has now been abandoned.

Molecular dynamics calculations by DA FANO and JACUCCI [1977] have shown that at high temperatures, when the atom jump frequency becomes large, a dynamical correlation between successive jumps can occur so that a vacancy can move more than one jump distance; these *vacancy double jumps* are an alternative explanation for the observed curvature of the Arrhenius plot.

1.1.2.3. Mixed mechanisms. For some systems it has been necessary to devise more complex mechanisms in order to account for abnormally fast diffusion. The dissociative

model by FRANK and TURNBULL [1956] was the first attempt at explanation. It assumed that the fast diffusing solute dissolves both substitutionally and interstitially; the mass transport is then due to a mixed vacancy and interstitial mechanism. MILLER [1969] has improved this mechanism by introducing the idea of vacancy-interstitial pairs. For more details see § 4.3.2.

1.1.2.4. Short-lived Frenkel pairs. Numerical simulations have revealed that, at least in non compact phases at high temperatures, short-lived Frenkel pairs can form *homogeneously* and give rise to closed rings of replacement of various sizes (4 atoms and above). At the end of the sequence the pair recombines (DOAN and ADDA [1987]).

1.1.3. Mechanisms involving extended defects

Linear defects (dislocations) and planar defects (surfaces, interfaces, grain boundaries, etc.) are disordered regions in which the atomic migration is easier than in the bulk. These preferential paths of diffusion are called *short-circuits*. The diffusion mechanisms are not yet well known but it is a topic where one is expecting rapid theoretical advances owing to the increasing power of computers. For more details see § 7.

1.2. The macroscopic theory of diffusion

1.2.1. Generalities

Diffusion is an irreversible phenomenon; its description requires the use of the proper formalism, namely *thermodynamics of irreversible processes* (TIP).

We refer the reader, for a detailed discussion of the subject, to specialized books and articles (PRIGOGINE [1947], HOWARD and LIDIARD [1964], MÜNSTER [1966], DE GROOT and MAZUR [1969]).

For measuring a flux, it is necessary to define a frame of reference; for the crystallized solid there are two preferred reference frames: the *laboratory reference frame* is bound to the ends of the sample which are assumed to be not affected by diffusion (we will neglect the sample size variation) whereas the *lattice reference frame* is rigidly bound to the atomic planes. It is possible to mark this lattice reference frame with inert markers such as very thin refractory wires, oxide particles, scratches on the surface etc.. These inert markers neither contribute nor alter the diffusion but "follow" the motion of the neighbouring atomic planes. Hereafter we will denote fluxes measured with respect to the laboratory frame by J^0 and fluxes measured with respect to the lattice frame by J.

The vacancy mechanism most commonly operates in metals and alloys; we will present the TIP formalism with this assumption. We assume further that the medium is isotropic; no chemical reactions take place; no viscous phenomena and no size variations occur; and, last, that mechanical equilibrium is achieved. We will restrict the discussion to the case of a binary alloy since only these alloys have been widely studied theoretically and experimentally.

1.2.2. Binary alloys and the vacancy mechanism

In a binary alloy there are three species: A, B and vacancies V; there will then be three fluxes, J_A, J_B and J_V in the lattice reference frame or J_A^0, J_B^0 and J_V^0 in the

laboratory frame. For a sample subjected to concentration gradients, ∇n_i, a temperature gradient, ∇T, and an electric field, E, it has been shown (BREBEC [1978]) that:

$$J_A = -D_A \nabla n_A + \left(L_{AA} Z_A^* + L_{AB} Z_B^*\right) eE - \left(L_{AA} Q_A^* + L_{AB} Q_B^*\right) \frac{\nabla T}{T} \tag{1}$$

$$J_B = -D_B \nabla n_B + \left(L_{BA} Z_A^* + L_{BB} Z_B^*\right) eE - \left(L_{BA} Q_A^* + L_{BB} Q_B^*\right) \frac{\nabla T}{T} \tag{2}$$

$$J_V = -\left(J_A + J_B\right) \tag{3}$$

$$v = \frac{J_V}{n} = -\frac{J_A + J_B}{n} \tag{4}$$

$$J_A^O = J_A + n_A v \text{ and } J_B^O = J_B + n_B v \tag{5}$$

We have omitted the vector notation for simplicity but we must keep in mind that J_i, ∇n_i, ∇T, E and v are vectors. Symbols are defined in what follows.

D_A and D_B are the *intrinsic diffusion coefficients*; they are given by:

$$D_A = kT\varphi\left(\frac{L_{AA}}{n_A} - \frac{L_{AB}}{n_B}\right), \qquad D_B = kT\varphi\left(\frac{L_{BB}}{n_B} - \frac{L_{BA}}{n_A}\right) \tag{6}$$

where k is the Boltzmann constant and L_{AA}, L_{AB}, L_{BA} and L_{BB} are the *phenomenological coefficients* which depend on the intensive quantities such as temperature, concentration, etc.; further they verify the *Onsager reciprocity relation* $L_{ij} = L_{ji}$, (here $L_{AB} = L_{BA}$); φ is the *thermodynamic factor* of the A-B solution; it is given by:

$$\varphi = 1 + \frac{\partial \log \gamma_A}{\partial \log C_A} = 1 + \frac{\partial \log \gamma_B}{\partial \log C_B} \tag{7}$$

where γ_A and γ_B are the thermodynamic activity coefficients. n_A, n_B and n_V are the numbers of A and B atoms and vacancies per unit volume, respectively.

The number of sites per unit volume is equal to:

$$n = n_A + n_B + n_V$$

We now define the *atomic fractions*, taking into account the three species:

$$N_A = \frac{n_A}{n}, \; N_B = \frac{n_B}{n} \text{ and } N_V = \frac{n_V}{n}$$

or, taking into account only the A and B atoms:

$$C_A = \frac{n_A}{n_A + n_B} \text{ and } C_B = \frac{n_B}{n_A + n_B}$$

Since n_V is always small ($n_V \ll n_A + n_B$), the two definitions are practically equivalent.

Z_A^* and Z_B^* are the *effective valences* for A and B and e the absolute value of the charge of an electron. If the material is an insulator or an ionic conductor, these effective valences are equal to the ionic valences z_A and z_B. In a metallic alloy for which the electrical conductivity is due to the electronic carriers there is a momentum transfer from these carriers (electrons or holes) to the A and B atoms. This is equivalent to a force which has to be added to the electrostatic force; as a consequence an effective valence can be defined (see § 6).

Q_A^* and Q_B^* are energies per mole and are related to the *heats of transport* q_A^* and q_B^*. Physically these heats of transport define the *heat flux*, J_q associated with the matter fluxes J_A and J_B when there is no thermal gradient. Actually it can be shown that:

$$J_q = q_A^* J_A + q_B^* J_B + \alpha \frac{\nabla T}{T} \tag{8}$$

which implies:

$$J_q = q_A^* J_A + q_B^* J_B \text{ when } \nabla T = 0$$

In metals and alloys the assumption is often made that the vacancies are in thermal equilibrium everywhere in the sample; this implies that the vacancy sources and sinks (dislocations, grains boundaries, etc.) are effective enough to fulfil this assumption. When this equilibrium condition is well obeyed we have:

$$Q_A^* = q_A^* - \Delta H_{FV} \text{ and } Q_B^* = q_B^* - \Delta H_{FV}$$

ΔH_{FV} is the *vacancy formation enthalpy* in the alloy.

When the requirement of local equilibrium is not met, no simple relation holds between Q_i^*'s and q_i^*'s.

Finally, v is the lattice velocity measured with respect to the laboratory frame. The physical reason for the lattice displacements is related to the fact that vacancies are not conservative species (they can be created or destroyed at certain lattice sites). In fig. 3 we have sketched the process responsible for the inert marker displacement; we see, in this simple example, that the lattice moves to the right because the vacancies created on the left are eliminated on the right.

We notice from equations (1)–(5) that the fluxes measured in the laboratory frame equal to:

$$J_A^O = C_B J_A - C_A J_B, \qquad J_B^O = -\left(C_B J_A - C_A J_B\right)$$

so that $J_A^O + J_B^O = 0$

1.2.3. Some special cases

1.2.3.1. Chemical diffusion. In the absence of electric fields and thermal gradients, eqs. (1)–(5) become:

$$J_A = -D_A \nabla n_A, \qquad J_B = -D_B \nabla n_B, \qquad v = \left(D_A - D_B\right)\nabla N_A \tag{9}$$

References: p. 651.

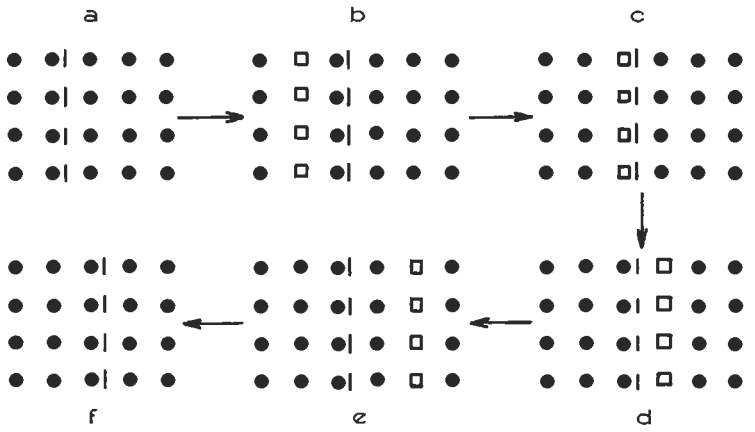

Fig. 3. Schematic representation of the displacement of inert markers (solid circles: atoms; squares: vacancies; dashes: inert markers: (a) initial state; (b) creation of a plane of vacancies; (c, d, e) displacement of the vacancy plane towards the right; (f) elimination of the vacancies. Comparison between (a) and (f) shows that the inert markers are displaced to the right.

In the laboratory frame we have:

$$J_A^O = -J_B^O = \tilde{D}\nabla n_A \tag{10}$$

where:

$$\tilde{D} = N_B D_A + N_A D_B \tag{11}$$

$\tilde{D}$ is the *chemical diffusion coefficient.*

We see that, for binary alloys, the fluxes have the form of *Fick's first law*:

$$J_i = -D_i \nabla n_i$$

In the lattice frame there are two independent fluxes and thus two intrinsic coefficients, whereas in the laboratory frame there is only one flux and one chemical diffusion coefficient.

1.2.3.2. Dilute systems. For dilute alloys n_B (or C_B) $\rightarrow 0$ and $\varphi \rightarrow 1$; on the other hand it can be shown (§ 4.1.2.1) that L_{BB}/n_B tends to a finite value, whereas L_{BA}/n_A, which is of the order of n_B, tends towards zero. So:

$$D_{B,n_B \rightarrow 0} = kT \frac{L_{BB}}{n_B} = D_{B^*} \tag{12}$$

This coefficient is the *solute diffusion coefficient at infinite dilution.* It will be denoted by D_{B^*} to distinguish it from D_B and to recall that diffusion is generally studied with radioactive isotopes which are used at great dilution; then we will also replace n_B by n_{B^*}. D_A does not become as simple as D_B because the cross-term L_{AB}/n_B does not tend to zero with n_B (§ 4.1.2.1).

For these dilute systems the flux of solute is equal to:

$$J_{B^*} = -D_{B^*}\nabla n_{B^*} + \frac{n_{B^*}D_{B^*}}{kT} Z_B^{**} eE - \frac{n_{B^*}D_{B^*}}{kT^2} Q_B^{**}\nabla T \tag{13}$$

where:

$$Z_B^{**} = Z_B^* + \frac{L_{AB}}{L_{BB}} Z_A^* \text{ (the apparent effective valence)}$$

$$Q_B^{**} = Q_B^* + \frac{L_{AB}}{L_{BB}} Q_A^* \text{ (the apparent heat of transport)}$$

Because $Z_{B^*}^* = Z_B^*$ and $q_{B^*}^* = q_B^*$(same chemical species) we have dropped the asterisk on B in Z_B^*, Z_B^{**}, Q_B^* and Q_B^{**}.

Equation (13) has the generalized form of Fick's first Law:

$$J_i = -D_i\nabla n_i + < v >_i n_i$$

When B atoms are isotopes A* of the element A, eq. (13) becomes:

$$J_{A^*} = -D_{A^*}\nabla n_{A^*} + \frac{n_{A^*}D_{A^*}}{kT} Z_A^{**} eE - \frac{n_{A^*}D_{A^*}}{kT^2} Q_A^{**} \tag{14}$$

It can be shown, (HOWARD and LIDIARD [1964]), that:

$$\frac{1}{f_0} = 1 + \frac{L_{A^*A}}{L_{A^*A^*}} \tag{15}$$

The apparent valency and heat of transport are therefore given by:

$$Z_A^{**} = \frac{Z_A^*}{f_0} \text{ and } Q_A^{**} = \frac{Q_A^*}{f_0}$$

where f_0 is the *correlation factor for self-diffusion*; its presence stems from the non-ramdom character of the tracer atom displacements by a vacancy mechanism. D_{A^*} is the *self-diffusion coefficient*, given by:

$$D_{A^*} = kT\frac{L_{A^*A^*}}{n_{A^*}} \tag{16}$$

1.2.4. The various diffusion coefficients

Diffusion coefficients have the dimension Length^2 Time^{-1}. In the international system of units they are expressed in m^2s^{-1}. The CGS system (cm^2s^{-1}) is still widely used. We will show now which experimental situations correspond to these various coefficients.

The *chemical diffusion coefficient* $\tilde{D}$ describe the interdiffusion of A and B (fig. 4a); it can be measured from the curve C_A (or C_B) versus x; in general it depends on the concentration.

The *intrinsic coefficients* D_A and D_B correspond to a similar experiment; but to obtain them it is necessary to determine $\tilde{D}$ and v [see eqs. (9) and (11)]. v is obtained from the displacement of inert markers (see *Kirkendall effect*, § 5.3.1.1). These coefficients depend also on the concentration.

The *solute diffusion coefficient at infinite dilution* D_{B^*} corresponds to the experimental situation shown in fig. 4b. A thin layer of B* atoms has been deposited on the A surface so that $C_{B^*} \sim 0$ and B* diffuses in pure A.

The *self-diffusion coefficient* D_{A^*} corresponds to a similar situation when B* is replaced by A*.

Two other diffusion coefficients are defined as shown in fig. 4c; they are the *self-diffusion coefficients in an homogeneous alloy* AB which are denoted by $D^{AB}_{B^*}$. The B* (or A*) concentration is always negligible so that the alloy composition is not modified by the diffusing species. These coefficients depend on the concentration. An alternative notation often used for dilute alloys is:

$$D_{A^*}(C_B) \equiv D^{AB}_{A^*},\ D_{B^*}(C_B) \equiv D^{AB}_{B^*}$$

where C_B is the concentration of B.

The macroscopic description presented above cannot account for the A* and B* diffusion into AB alloys; it would be necessary to derive the flux equations for four species A, A*, B, B* (plus vacancies); this is beyond the scope of this review and we refer the reader to HOWARD and LIDIARD [1964] for more details. Thus it is possible to show that the self-diffusion coefficients in the alloy and the intrinsic diffusion coefficients are related by:

$$D_A = D^{AB}_{A^*}\varphi r_A \quad D_B = D^{Ab}_{B^*}\varphi r_B \tag{17}$$

where φ is the thermodynamic factor and r_A and r_B are terms which will be made explicit in § 5.1.2. These relations, (17), were first established by DARKEN [1948] in a

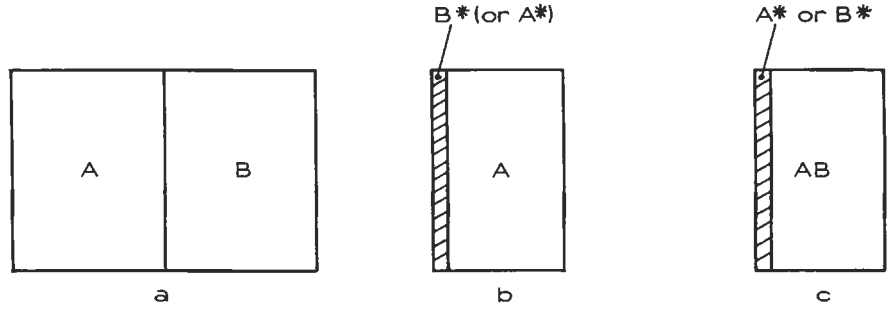

Fig. 4. Different types of diffusion experiments: (a) chemical diffusion → $\tilde{D}$; (b) self or solute diffusion in pure metals → D_{A^*} or D_{B^*}; (c) self-diffusion in homogeneous alloys → $D^{AB}_{A^*}$ or $D^{AB}_{B^*}$